Nanoparticle-based intracellular diagnostics

by

Barbara Korzeniowska

A thesis presented to Dublin City University
for the Degree of Doctor of Philosophy

Research supervisor:
Prof. Colette McDonagh
School of Physical Sciences
Dublin City University

July 2012

Declaration

I hereby certify that this material, which I now submit for assessment on the programme of study leading to the award of Doctor of Philosophy is entirely my own work, that I have exercised reasonable care to ensure that the work is original, and does not to the best of my knowledge breach any law of copyright, and has not been taken from the work of others save and to the extent that such work has been cited and acknowledged within the text of my work.

Signed: . . . . (Candidate) ID No.: .58102825. . . .

Date: . . . .09/07/2012 . . . .

Dedication

To my best Flatmate, Friend, Companion,

- *My Husband*

Acknowledgments

I would like to thank my research supervisor Colette McDonagh for her excellent supervision, all her support, encouragement and especially for her friendship, which were invaluable during the four years of my PhD pathway.

A very special word of thanks goes to my colleague, Dorota Wencel, for all her friendship, scientific and non-scientific support and for her very pleasant company in the office, and overall for giving me a great example of the researcher, which contributed a lot to my personal development. Thanks to her I understood that there is nothing impossible, it is only a matter of good will.

Thanks to Rob Woolley, for opening to me a new world of microscopy, as well as for his guidance and participation into the project. He also showed me the complexity of the biological matter, which enabled me to widen my horizons greatly.

I also want to take the opportunity to thank all the OSL members, and other DCU colleagues who created a very friendly and relaxed work environment. From them I really learnt the meaning of trust and reliability.

To Joey Decourcey, who was a great teacher in the cell culturing techniques, for his assistance, availability and friendship.

To Prof. Kees Jalink and Dr Marcel Raspe from Netherlands Cancer Institute, for the research collaboration and enthusiasm, which they showed during our project time together.

To my parents, who were always encouraging me to study. Without them, I would not have got to where I am now.

To my Italian family, who always was close to me, giving smiles, support and a lot of love. Thanks to them, I learnt how to face the world, and how to be happy even in the difficult moments.

And finally, to my husband, Alessio, who made this possible through his constant support, encouragement, and love which I can never repay. I hope that he will consider my achievement his as well. It is to him that I dedicate this thesis.

“There’s Plenty of Room at the Bottom”

R. Feynman, 1959

Table of contents

5. Intracellular sensing ………………………………………………………... 112

Abstract

An in-depth understanding of biochemical processes occurring within the cell is a key factor for early diagnosis of disease and identification of appropriate treatment. Intracellular sensing using fluorescent nanoparticles (NPs) is a potentially useful tool for real-time, in vivo monitoring of important cellular analytes.

This work is focused on synthesis of organically modified-silicate (ORMOSIL) optical nanosensors for the quantitative analysis of oxygen concentration and pH sensing inside the cell. The structure of the sensor consists of a biofriendly silica matrix with encapsulated oxygen/pH-sensitive dyes. The optical probes used in this work are the oxygen-sensitive ($[Ru(dpp)_3]^{2+}$) complex and pH-sensitive fluorescein isothiocyanate (FITC) co-encapsulated with the ATTO488 and Texas Red as the reference dyes, respectively. In order to obtain silica-based NPs, the Stöber method was used. The NPs were characterised using techniques such as Transmission Electron Microscopy (TEM), Dynamic Light Scattering (DLS), fluorescence and other spectroscopic techniques.

The second part of this work focuses on the introduction of the NPs into the cell and intracellular sensing. In this work the oxygen and pH nanosensors are introduced in a number of established human and mouse cell lines. Internalization of NPs within the cell is investigated using fluorescence confocal microscopy techniques. The detection of the optical signal is based on both ratiometric and fluorescence lifetime – based measurements carried out on the wide-field and confocal microscopes with fluorescence lifetime imaging platforms. After the NP calibration, the response of the cell to the different extracellular oxygen concentration is investigated.

Oxygen and pH sensing is the starting point for this intracellular diagnostics research. The silica-based NPs, thanks to the flexible processing conditions, allow for tailoring of pore size and hydrophilic-hydrophobic balance. The possibility to control these two parameters makes the NPs a very promising tool for a better understanding of many processes in living cells.

Abbreviations and Symbols

λ	wavelength
λ_{exc}	excitation wavelength
μm	micrometer
μs	microsecond
Φ	phase angle
Φ_0	phase angle in 0% O_2
Φ_{100}	phase angle in 100% O_2
τ	excited state lifetime of the luminophore
τ_0	excited state lifetime in absence of quencher (oxygen)
°	degree
3D	three-dimensional
6PG	6-phosphogluconate
$[O_2]$	oxygen molar concentration
$[Ru(bpy)_3]^{2+}$	[Ru(II)-tris(2,2'-bipyridine)]
$[Ru(dpp)_3]^{2+}$	[Ru(II)-tris(4,7-diphenyl-1,10-phenanthroline)]
$[Ru(phen)_3]^{2+}$	[Ru(II)-tris(1,10-phenanthroline)]
A	absorption
a	activity
a_{H+}	hydrogen ions activity
A^-	basic (deprotonated) form of the pH indicator
APTES	Aminopropyltriethoxysilane
ATP	adenosine triphosphate
BET	Brunauer, Emmett, Teller
BP	Band-pass
c	molar concentration
CCD	charge coupled device
COPD	Chronic Obstructive Pulmonary Disease
CNS	Central Nervous System
CO_2	carbon dioxide
D	diffusion coefficient
DI water	deionised water
DLS	Dynamic Light Scattering
DMEM	Dulbecco's Modified Eagles Medium
DMSO	dimethyl sulfoxide
DNA	deoxyribonucleic acid
EtOH	Ethanol
f_{H+}	activity coefficient value
F	fluorescence intensity

f_i	fractional contribution to the total emission from site i
FACS	Fluorescence-activated cell sorting
FAD	Flavine Adenine Dinucleotide
FADH	Flavine Adenine Dinucleotide, semiquinone form
FCS	Fetal Calf Serum
FITC	fluorescein 5(6)-isothiocyanate
FLIM	fluorescence lifetime imaging microscopy
FRET	fluorescence resonance energy transfer
fs	femtosecond
FTIR	Fourier Transform Infrared Spectroscopy
G6P	glucose-6-phosphate
g/L	gram/liter
h	hour
HA	acidic (protonated) form of the pH indicator
HCl	hydrochloric acid
HEK293	Human Embryo Kidney 293 cells
HIF-1	Hypoxia-Inducible Factor-1
H_3O^+	hydronium ions
HCO_3^-	bicarbonate ions
HPTS	1-hydroxypyrene-3,6,8-trisulfonic acid
Hz	Hertz
I_{O2}	luminescence intensity in the presence of quencher (oxygen)
I_{N2}	luminescence intensity in the absence of quencher (oxygen)
IC	internal conversion
$Ir(Cs)_2(acac)$	Iridium (III)((benzithiazol-2-yl)-7-(diethylamino)-cumarin))2(acetylacetonat)
IS	ionic strength
ISC	intersystem crossing
Ka	acid dissociation constant
K_i	equilibrium constant
k_q	bi-molecular quenching constant
k_r	rate of radiative decay
k_{nr}	rate of non-radiative decay
k_{ISC}	rate of singlet to triplet intersystem crossing
Ksv	Stern-Volmer constant
K_{Svi}	discrete Stern-Volmer constant associated with site i
K_2HPO_4.	Potassium salts of hydrogen phosphate
KH_2PO_4.	Potassium salts of dihydrogen phosphate
kHz	kilohertz
LED	Light Emitting Diode
LP	Long-pass
LSCM	laser scanning confocal microscopy
MCP	micro-channel plate
MLCs	transition-metal-ligand complexes
mM	millimolar
mms^{-1}	millimeter/second
mol/L	mole/liter

MTEOS	Methyltriethoxysilane
MTMS	Methyltrimethoxysilane
mV	millivolt
mW	milliwatt
m_ω	modulation factor
N	Avogadro's number
N_2	nitrogen
NADP	nicotinamide adenine dinucleotide phosphate
NADPH	nicotinamide adenine dinucleotide phosphate-oxidase
NHS	N-hydroxy-succinimidyl
NH_4OH	ammonium hydroxide solution
nm	nanometer
NO_2	nitrogen dioxide
ns	nanosecond
O_2	oxygen
ORMOSIL	ORganically MOdified SILicate
P	phosphorescence intensity
PALM	photo-activated localization microscopy
PAHs	polycyclic aromatic hydrocarbons
PBS	Phosphate Buffer Saline
Pd	Palladium
PD	photodiode
PDI	Poly Dispersity Index
Pdots	polymer dots
PDMA	Polydecylmethacrylate
PEBBLE	Photonic Explorer for Bioanalysis with Biologically Localized Embedding
PhTEOS	Phenyltriethoxysilane
pKa	negative logarithm of an acid dissociation constant
PMTs	photomultiplier tubes
PNS	Peripheral Nervous System
pO_2	partial pressure oxygen
Pt	Platinum
ps	picosecond
PTMS	Phenyltrimethoxysilane
Q	quencher
QD	semiconductor quantum dots
R-COOH	carboxylic acid
$R\text{-}COO^-$	carboxylate anion
r^2	the square of the correlation coefficient, regression
rcf	relative centrifugal force
RNA	ribonucleic acid
ROS	reactive oxygen species
S_0	ground state
S_1	first singlet excited state
S_2	second singlet excited state
SERS	Surface-enhanced Raman Scattering

SNAFL	Carboxyseminaphthofluorescein
SNARF	Seminaphtharhodafluor
SNR	signal to noise ratio
STEM	stimulated emission depletion microscopy
STORM	stochastic optical reconstruction microscopy
T_1	first triplet excited state
TCSPC	Time-correlated single-photon counting
TEM	Transmission Electron Microscopy
TEOS	Tetraethoxysilane
TLR4	Toll-like receptor 4
TTTR	Time-Tagged Time-Resolved
U_2OS	Human Osteosarcoma Epithelial (cells)
UV-Vis	ultraviolet-visible
V_R	vibrational relaxation
XPS	X-ray Photoelectron Spectroscopy

Chapter 1

Introduction

1.1. Cellular diagnostics

“The constant conditions which are maintained in the body might be termed equilibria. That word, however, has come to have a fairly exact meaning as applied to relatively simple physico-chemical states, in closed systems, where known forces are balanced. The coordinated physiological processes which maintain most of the steady states in the organism are so complex and so peculiar to living beings — involving, as they may, the brain and nerves, the heart, lungs, kidneys and spleen, all working cooperatively — that I have suggested a special designation for these states, homeostasis. The word does not imply something set and immobile, a stagnation. It means a condition — a condition which may vary, but which is relatively constant.” [1]

This sentence, published by American biologist Walter Cannon in the 1930s, is a starting point in understanding the importance of cellular sensing which enables the detection of changes in the analyte concentration at a ppm (parts per million) level. The homeostasis mechanism plays a key role in the adaptation by the body to constantly changing conditions. If there is any breakdown in homeostatic mechanisms, the body is not able to maintain a balance and, as a consequence, disorder and disease occur. Unfortunately, in many cases, the disease “macro-symptoms” are only recognisable when irreversible changes have already taken place. It would be highly desirable in early stage diagnosis to detect the disease “micro-symptoms”, which would be manifested as very small changes of the analytes happening at the cellular level. This insight into the inter- and intracellular environment could enable the monitoring of the homeostasis of the body, thus enabling an early response and treatment in order to prevent serious pathological conditions.

1.2 Oxygen and its role

Elixir of Life – and Death – this ambiguous title can be found in the book written by Nick Lane, describing "oxygen - the molecule that made the world" [2]. The therapeutic abilities of "active", meaning ozone and hydrogen peroxide-based oxygen treatments against bacterial infections and tumours coexist together with the toxic and apoptosis-inducible character of the same "active" components. Life depends on oxygen, from the moment when the first organisms, which appeared 2.5 billion years ago, were able to convert solar energy into chemical energy of carbon bonds. The evolution machinery gave them the unique photosynthesis skill, which enabled them to convert carbon dioxide and water into glucose and oxygen. One billion years later, the next generation of organism, eukaryotes, came into being and closed the energy cycle by transforming glucose into carbon dioxide and water in the process called cellular respiration. This process consists of two steps: glycolysis and oxidation of pyruvic acid. The energy produced during the glycolysis process is then trapped in molecules of ATP, what is illustrated in Figure 1.1.

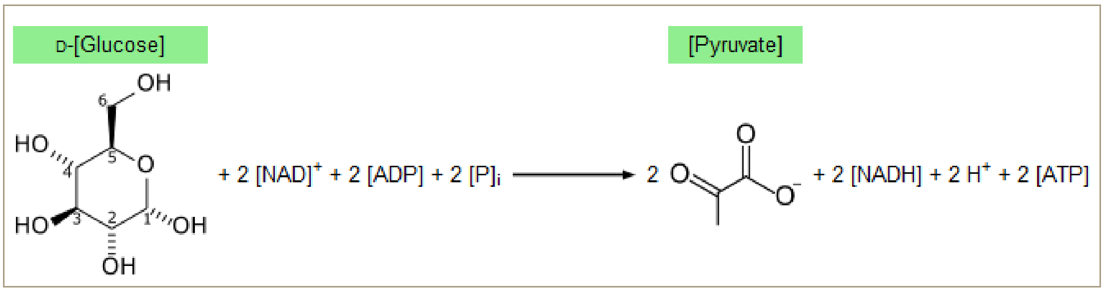

Figure 1.1: The glycolysis process [3].

The reaction efficiency, 2 molecules of adenosine triphosphate (ATP) per 1 molecule of glucose, is not as high as would be required for developing and maintaining more advanced organisms. To satisfy the need of metazoans, the next cell-type in the evolution chain, oxidative phosphorylation evolved around 0.5 billion years ago. This new metabolic pathway, in comparison to glycolysis, produced 18 times as much ATP per 1 mole of glucose, which is enough to perform the functions of these complex multicellular organisms. A schematic of this process is shown in Figure 1.2.

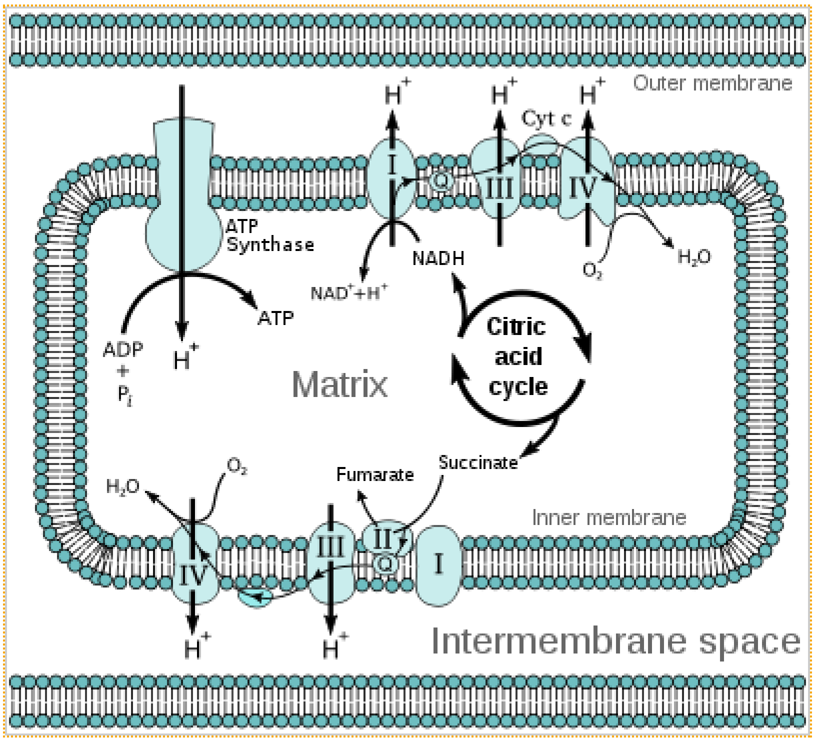

Figure 1.2: The oxidative phosphorylation process [4].

The same metabolic route, called aerobic respiration, is used by the human body. This highly efficient process, which utilizes oxygen as an energy source, has however dual nature: it can maintain or terminate life. In the creation of ATP molecules, a fraction of electrons, escapes from the respiratory chain and combine with the oxygen molecule O_2, generating the so-called “active” oxygen mentioned at the beginning of this chapter. This type of oxygen is now referred to as free radicals [5]. Apart from in the mitochondria, where they are naturally produced by the oxidative phosphorylation process, free radicals are also formed at inflammation sites and as a by-product of some normal cellular enzymatic reactions as well as exogenously generated by exposure to pesticides, radiation, pharmacological agents, industrial pollutants, food additives, cigarette smoke and many others agents [6]. Any deviation in their production can result in oxidative stress and lead to a pathological state for the human body. Some human diseases associated with generation of free radicals have been gathered in the Table 1.1:

Table 1.1: Oxidative stress-related human diseases [6].

ORGAN SYSTEM	**DISEASE**
Brain, Central Nervous System(CNS), Peripheral Nervous System (PNS)	Alzheimer`s, Parkinson`s, Huntington`s, Multiple Sclerosis, Trauma, Stroke, Ischemia, Other Neurodegenerative disorders
Circulatory	Atherosclerosis, Hyperlipidemia, Cardio-vascular diseases, Vascular disorders, Hypertension
Endocrine	Diabetes, Metabolic Syndrome
Musculoskeletal	Arthritis, Physical injury, Joint disorders
Immune	Allergic disorders, Autoimmune disorders, Inflammatory disorders
Respiratory	Asthma, Emphysema, Chronic Obstructive Pulmonary Disease (COPD), Bronchitis
Digestive	Inflammatory bowel disease, Crohn`s disease

Oxygen therefore is a crucial component for the human body, and should be monitored in order to maintain a balance between the generation of energy and production of potentially toxic oxidants. It is proposed that the non-invasive oxygen nanosensor, which is the subject of this PhD thesis, could act as an effective early diagnostic device, thus fulfilling this oxidative stress screening function.

1.3. Intracellular pH

The term pH was introduced at the beginning of 20th century by the Danish chemist Sørensen who applied the electromotive force technique in order to determine the hydrogen ion concentration. In his publication from 1909, he defined pH as the negative logarithm of the hydrogen ion concentration [7]:

$$pH = -\log[H^{+}] \tag{1.1}$$

The level of acidity and alkalinity is represented on a scale from 1 to 14, where an increase in the amount of protons results in a decrease in the pH value. The chemicals which have a strong influence on the pH are acids which are proton donors and bases which are proton acceptors. The mechanism of introducing a proton to an aqueous solution is based on the molecule dissociation process, an example of which is shown below:

$$R - COOH \rightleftharpoons R - COO^{-} + H^{+} \tag{1.2}$$

Where R-COOH is a general formula for a carboxylic acid and R-COO^{-} is a carboxylate anion. The tendency to ionize varies between different acids, which can be expressed by the difference in the dissociation constant, Ka:

$$K_a = \frac{[R - COO^{-}][H^{+}]}{[R - COOH]} \tag{1.3}$$

Where [R-COO^{-}], [H^{+}] and [R-COOH] are the molar concentrations of carboxylate anions, hydrogen ions and carboxylic acid respectively. Using equation 1.2 the dissociation constant Ka can be then translated into pKa value:

$$pK_a = -\log K_a \tag{1.4}$$

Only strong acids and strong bases will be completely dissociated under respectively low and high pH. In the case of weak acids and weak basics, which are capable of dissociating very easily, the protonic equilibrium will be prone to change giving small changes in pH, which is expressed in the Henderson – Hasselbalch equation:

$$pH = pK_a + \log\frac{[R - COO^{-}]}{[R - COOH]} \tag{1.5}$$

In the intracellular environment, many macromolecules, which are responsible for the proper functioning of the cell, possess functional groups which are weak acids or bases [8]. As a consequence, even small changes in pH may have a huge impact on the cell. Some common factors which influence cell pH are illustrated in Table 1.2.

Table 1.2: Influence of intracellular pH on the cellular functions.

Factor	Influence of pH
Activity of metabolic enzymes	Increase of the activity of the enzyme with increasing pH (i.e. phosphofructokinase [9])
Protein synthesis	Increase in rate of protein synthesis from pH 6.9 and its optimum at pH 7.4 [10]
Synthesis of DNA and RNA	Increase in DNA and RNA synthesis with higher pH within physiological range [11]
Actin and myosin contractility	Low pH reduces the contractility (i.e. ischemia in the heart muscle [12])
Ion channels conductivity	Decrease in pH inhibits the conductivity of potassium channels, which stimulate voltage-gated calcium channels [13]
Proliferation and apoptosis	Increase in pH induces the cell proliferation and cell division [14]
Multidrug resistance	Alkaline shift of cytosolic pH inhibits the intracellular drug accumulation[15]
Endocytosis	Cytoplasmic acidification (below pH 6.5) inhibits endocytosis [16]

Maintaining a stable physiological pH at 7.0-7.4 for neutral and slightly alkaline cytoplasm and lower acidic pH of 4.0 - 6.0 for endosome and lysosome compartments will be therefore crucial for intracellular homeostasis. [2,17] On the other hand, monitoring intracellular pH can be a very powerful tool in the fight against such diseases as cancer and Alzheimer's where indicative abnormal pH values have been detected [18].

1.4. Optical Chemical Nanosensors

Man has always been curious about and has striven to understand his surrounding environment. This exploration has been carried out largely by measurement techniques. Building up knowledge with time, man has succeeded in achieving a very sophisticated level of measurement of different physical, biological and chemical environments [19]. Using sensors, devices which respond in selective and reversible way to different compounds and ions, it is possible to measure very small quantities of analytes [20]. Generally, a sensing platform contains three main elements:

- the active surface
- the transducer
- the electronics/software.

These elements are illustrated in Figure 1.3.

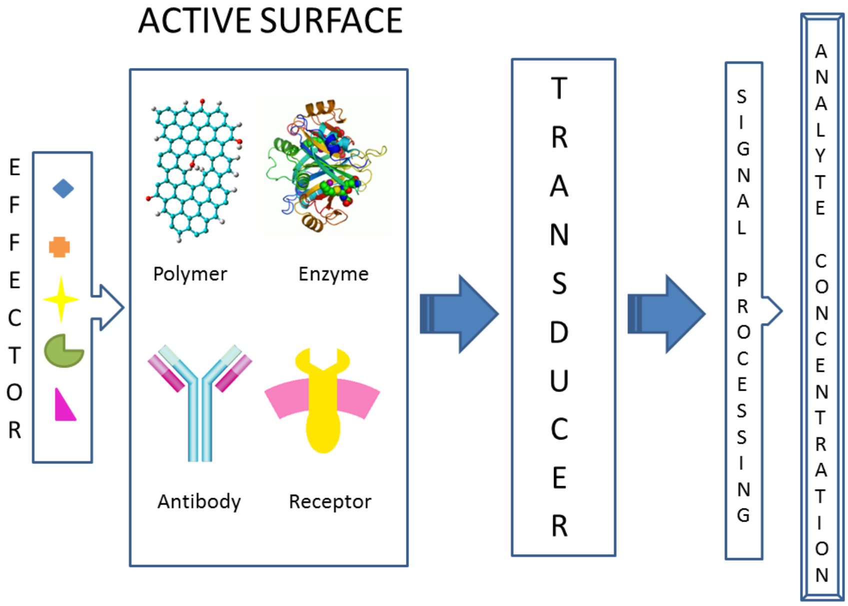

Figure 1.3: The basic components of a sensor.

The nature of the active surface determines the type of sensor. If the active surface contains some non-biological material, for example a polymeric membrane which reacts with the substrate, the sensor is defined as a chemical sensor. This is defined by R.W. Catterall [21] as “a device which responds to a particular analyte in a selective way through a chemical reaction and can be used for the qualitative and quantitative determination of the analyte". An optical chemical sensor is based on an optical transduction method, which can be optical absorption, luminescence (which is the most sensitive) or other optical parameters such as refractive index or reflectivity [22]. Biosensors utilize biomolecules such as enzymes, antibodies and receptors or a cell to react with the analyte. Due to these biological recognition elements they have advantages like high specificity and/or exceptionally high natural selectivity, and drawbacks such as restricted stability and lifetime [20]. In this work, the developed sensors can be described as Optical Chemical Nanosensors as, while the sensing principle of the oxygen or pH is via chemical sensing, the sensor's dimension is in nanometer range. The general sensing pathway can be described as follows:

1) Chemical or biological reaction between analyte and the active surface
2) Change in the transducer due to the reaction, which can be expressed as change of impedance, voltage, light intensity, reflectance, etc. Usually the magnitude of the electronic signal is proportional to the analyte concentration
3) Detection, amplification and processing the signal by electronics/software module

Key sensor properties and behaviour in an ideal situation are described in Table 1.3.

Table 1.3: The ideal sensor characteristics [23].

PROPERTY	CHARACTERISTIC BEHAVIOUR OF IDEAL SENSOR
Sensitivity	Constant during the sensor lifetime and sufficiently high to allow convenient measurement of the signal
Calibration	Ease of calibration and preferably single point calibration
Linearity	In the full region of the substrate concentration (can be also nonlinear but more complicated signal analysis)
Limit Of Detection	The lowest concentration of substrate determined by the resolution of the electronic instrumentation
Background Signal	Constant with the sensor signal changes
Hysteresis	No influence from previous measurements = zero hysteresis

Drift And Long-Term Stability	Constant sensitivity for the sensor entire lifetime or at least during the time of measurement
Selectivity	Response only to the target analyte changes and no interference from other analytes
Dynamic Response	Fast response to a change in analyte concentration
Temperature Dependence	Isothermal experimental conditions
Signal To Noise Ratio	Digital filtering techniques
Lifetime	Sensitive under normal operational conditions
Biocompatibility	Minimum impact on the human body

In recent decades, nanotechnology has had a major impact on sensing, particularly for biomedical applications. The capability to observe interactions unique to the nanoscale between matter and its environment and new behaviours not present at the macroscale, is a powerful driver for the new discipline of Nanomedicine. Nanosensors which could scan for the presence of infectious agents or any signs of homeostatic imbalances, as well as eliminate infectious agents and fix the “broken” parts in cells are under investigation. There is much work worldwide on the development, clinical implementation and evaluation of hazards related to these new nanodevices which should be a source of hope for the many people suffering from diseases such as multiple sclerosis and other as yet, incurable conditions [24].

1.5. Thesis structure

This work was focused on the sensing of oxygen and pH inside cells. In order to achieve quantitative information on inter- and intracellular level of the analytes, nanoparticles (NPs) in which were entrapped an oxygen-sensitive long lifetime ruthenium complex or a pH-sensitive fluorescein isothiocyanate fluorophores, were fabricated using the Stöber method. The sensor response of the nanosensors was first measured outside the cell environment. The NPs were then introduced to a range of different cell types including phagocytic and non-phagocytic cell lines, using a number of different particle loading techniques. The intracellular sensor response was monitored using both luminescence intensity imaging and lifetime based imaging techniques such as confocal microscopy and fluorescence lifetime imaging microscopy (FLIM).

The PhD thesis consists of six chapters. After an abstract, Chapter 1 gives a brief overview of the different elements of the work and details the work objectives. In the context of the interdisciplinary character of the project, the physics, chemistry and biology background is described in Chapter 2. Chapters 3 and 4 describe the experimental results for oxygen and pH respectively including NP synthesis, characterisation and extra-cellular sensor response while Chapter 5 deals with the intracellular sensing aspect of the project. The thesis concludes with a brief Summary and Perspectives chapter.

1.6. Research objectives

The main objectives of this project were:

1. To synthesise novel oxygen and pH sensitive nanoparticles for application in intracellular sensing.
2. To introduce the developed nanosensors inside the cells and determine their intracellular localisation.
3. To measure the intracellular concentration of analytes in a number of established human and mouse cell lines using different microscopy imaging approaches.

References

[1] Cannon, W. B. *The Wisdom of the body.* W. W. Norton&Company, Inc., USA, 1932.

[2] Lane, N. *Oxygen: The Molecule that Made the World.* Oxford University Press Inc., New York, 2002.

[3] "Glycolysis process". http://en.wikipedia.org/wiki/Glycolysis.

[4] "Oxidative phosphorylation". en.wikipedia.org/wiki/Oxidative_phosphorylation.

[5] Semenza, G. L. Life with oxygen. *Science,* **2007**, *318*, 62-64.

[6] Shanti, R. M.; Tuan, R. S.; Kumar C. S. S. R. *Tissue, cell, and organ engineering.* Nanotechnologies for the life sciences; Wiley-VCH, Weinheim, 2006.

[7] Sorensen, S. P. L. *World of Chemistry*. Thomson Gale, a part of the Thomson Corporation, 2005-2006.

[8] Martin, D. W.; Mayes, P. A.; Rodwell, V. W. *Harper's Review of Biochemistry.* LANGE Medical Publications, USA, 1981.

[9] Fidelman, M. L.; Seeholzer, S. H.; Walsh, K. B.; Moore, R. D. Intracellular pH mediates action of insulin on glycolysis in frog skeletal muscle. *Am. J. Physiol.***1982**, *242,* 87-93.

[10] Winkler, M. M. *Intracellular pH: Its Measurements, Regulation and Utilization in Cellular Functions.* Alan R. Liss, New York, 1982, 325-340.

[11] Hayward, N. K.; Lavin, M. F. Inhibition of DNA, RNA and protein synthesis and chromatin alteration by N-hydroxyphenacetin. *Xenobiotica*, **1987**, *17*, 115-24.

[12] Jacobus, W. E.; Pores, I. H.; Lucas, S. K.; Kallman, C. H.; Weisfeldt, M. L.; Flaherty, J. H. *Intracellular pH: Its Measurement, Regulation and Utilization in Cellular Functions* Alan R Liss New York , 1982, 537-565.

[13] Moody W. J. Jr. Effects of intracellular H^+ on the electrical properties of excitable

cells. *Annual Review Neuroscience,* **1984**, *7*, 257-278.

[14] Han, J.; Burgess, K. Fluorescent Indicators for Intracellular pH. *Chem. Rev.,* **2010**, *110*, 2709-2728.

[15] Gottlieb R. A.; Nordberg J.; Skowronski E.; Babior B. M. Apoptosis induced in Jurkat cells by several agents is proceded by intracellular acidification *Proc. Natl. Acad. Sci. USA,* **1996**, *93*, 654-658.

[16] Izumi, H; Torigoe, T; Ishiguchi, H; Uramoto, H; Yoshida, Y; Tanabe, M; Ise, T; Murakami, T; Yoshida, T; Nomoto, M; Kohno, K. Cellular pH regulators: potentially promising molecular targets for cancer chemotherapy. *Cancer Treat Rev.,* **2003**, *29*, 541-549.

[17] Madshus, I. H. Regulation of intracellular pH in eukaryotes cells. *Biochem. J.*, **1988**, *250*, 1-8.

[18] Davies, T. A.; Fine, R. E.; Johnson, R. J.; Levesque, C. A.; Rathbun, W. H.; Seetoo, K. F.; Smith, S. J.; Strohmeier, G.; Volicer, L.; Delva, L. Non-age related differences in thrombin responses by platelets from male patients with advanced Alzheimer's disease. *Biochem Biophys Res Commun.,* **1993**, *194*, 537-43.

[19] Taylor, R. F.; Schultz, J. S. *Handbook of chemical and biological sensors.* Institute of Physics Pub., Bristol, Philadelphia, 1996.

[20] Spichiger-Keller, U. E. *Chemical sensors and biosensors for medical and biological applications.* Wiley-VCH, Weinheim, 1998.

[21] Cattrall, R. W. *Chemical sensor.* Oxford chemistry primers, Oxford University Press, Oxford, New York, 1997.

[22] McDonagh, C.; Burke, C. S.; MacCraith, B. D. Optical chemical sensors. *Chem. Rev.,* **2008***, 108*, 400-422.

[23] Buerk, D. G. *Biosensors: theory and applications.* Technomic Pub. Co, Lancaster Penn., 1993.

[24] Hornyak, G. L. *Introduction to nanoscience and nanotechnology.* Taylor & Francis, Boca Raton, 2009.

Chapter 2

Background

2.1 Introduction

This chapter gives a comprehensive overview of all theoretical aspects related to the thesis. Due to the interdisciplinary nature of this work, the background from the different disciplines of physics, chemistry and biology is presented below. Optical chemical sensors, with special emphasis on luminescence–based sensors, are discussed at the beginning. The concept of nanosensor and its application for intracellular studies is then introduced. This is followed by a discussion on the optical detection and imaging techniques used. The last section gives an introduction to the biological aspects, such as how O_2 and pH sensing occur inside the cell as well as what are the possible intracellular pathways of nanoparticle uptake.

2.2 Overview of luminescence

2.2.1 Luminescence phenomenon

The process of absorption of photons by a material occurs on a very fast timescale, of the order of 10^{-15}s. In this process, the electrons are excited from the ground state energy level to a higher, more energetic state. The ground and excited states have a number of discrete vibrational and rotational energy states. As a consequence the molecule can be excited with different absorption energies, which broadens the absorption and emission spectra. The factors which determine whether a photon is absorbed/emitted by a molecule are the photon energy and the energy level differences and, more fundamentally, the quantum mechanical transition probabilities [1]. Electrons can be transferred between two energy levels only if the photon energy is exactly equal to the energy level difference. The process of electron de-excitation is called luminescence and it is well illustrated on the Jablonski diagram shown in Figure 2.1.

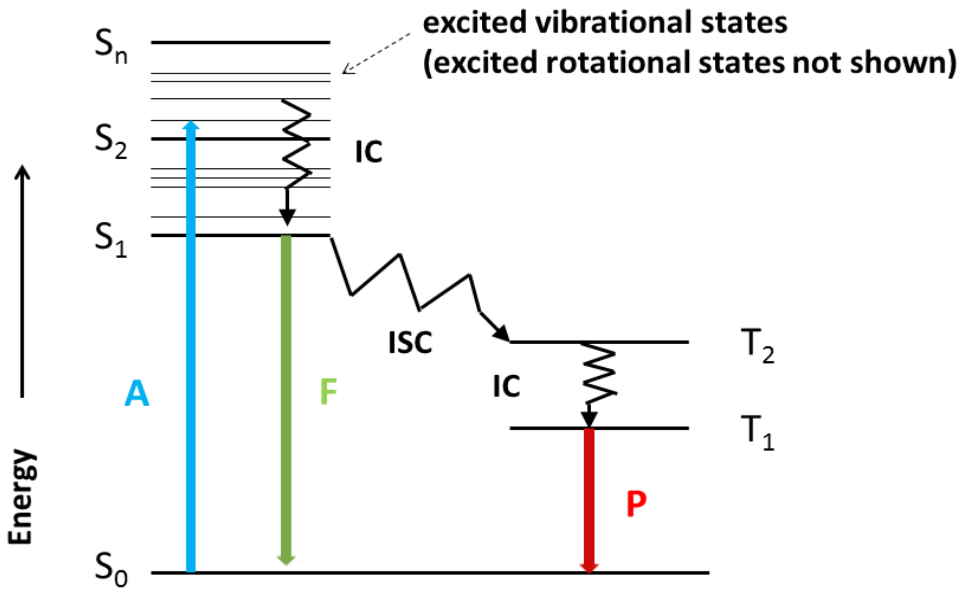

Figure 2.1: The Jablonski diagram. A-photon absorption, F-fluorescence, P-phosphorescence, S-singlet state, T-triplet state, IC-internal conversion, ISC-intersystem crossing.

Before luminescence occurs, electrons may lose energy thermally in a process called internal conversion. In these 10^{-11} seconds the electrons move to the lowest excited singlet state, S_1, where they stay for a period of the order of nanoseconds. The luminescence energy released by the molecule while relaxing to the ground state, S_0, will be the energy level difference between the vibrational energy state $v_1=0$ and whichever ground state energy level the electron occupies [2]. Depending on the nature of the excited state the resulting luminescence or emission process can be divided into two categories: fluorescence and phosphorescence. Fluorescence occurs when electrons excited to a singlet state rapidly decay with an emission rate of typically 10^{-8}s. Electrons can also de-excite from the lowest excited singlet state to a triplet state by intersystem crossing. The process of returning from the triplet state to the ground state and the associated emission of light is called phosphorescence and it lasts much longer (10^{-3}-10^{0} s) than fluorescence. Molecules which contain a metal and one or more organic ligands called transition-metal-ligand complexes (MLCs) have a particular way of de-excitation, due to the presence of mixed singlet-triplet states; as a consequence, electrons can take from 400ns to several microseconds to come back to the ground state. It is noted that the ruthenium complex used in this work belongs to the group of MLCs [1] and displays phosphorescent emission while the transitions of the pH dyes, fluorescein and 1-hydroxypyrene-3,6,8-trisulfonic acid (HPTS), display fluorescence (short ~ns) lifetime decays. In order to simplify the terminology, luminescence is used in this thesis to denote all photon emission processes.

2.2.2 Stokes' shift

The difference in the position of the maxima for absorption and emission spectra of the luminescent molecule is defined as the Stokes' shift and is shown in Figure 2.2.

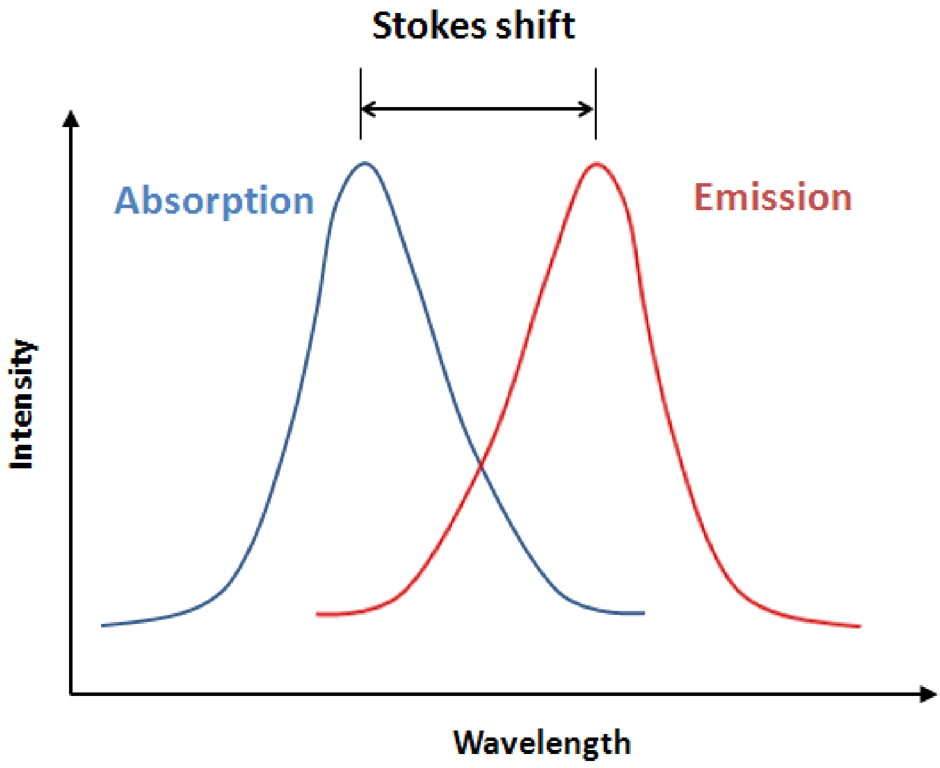

Figure 2.2: Stokes` Shift.

As described in section 2.1.1, the energy absorbed by the molecule excites the electrons from the ground state to the higher excited state. Emission of photons will occur when the electrons de-excite to the lowest vibrational energy level of the excited state by internal conversion and other non-radiative quenching processes. The emission spectrum determined by the energy level differences will be therefore shifted towards longer wavelengths compared to the absorption peak wavelength thus constituting the Stokes' Shift. Both spectra are representative of the particular molecular structure of the luminophore [2].

2.2.3 Luminescence lifetime and quantum yield

The luminescence lifetime τ and quantum yield Φ are key properties of a luminescent molecule or luminophore. The lifetime is the average time which the electron in the molecule spends in the excited state prior to returning to the ground state. After absorption of light, due to the conformational changes and the interaction between the luminophore and its environment, the luminescence intensity will decrease exponentially, what is described by the equation:

$$I(t) = I_0 e^{(-t/\tau)} \tag{2.1}$$

Where:

$I(t)$ - intensity measured at time t
I_0 - initial intensity just after excitation
τ - luminescence lifetime

The lifetime is defined as the time in which the luminescence intensity decays to 37% of its initial value just after the excitation pulse [1]. The decay can be either single exponential or multi-exponential, depending on the environment [2].

The quantum yield, Φ is a measure of the efficiency of the emission and is defined as the ratio of emitted to absorbed photons and its value varies from 0 to 1. The influence of the non-radiative processes, defined as quenching, has to be considered here. Assigning the rate for all radiative processes as Γ and non-radiative processes as k_{nr}, the quantum yield can be expressed as:

$$\phi = \frac{\Gamma}{\Gamma + k_{nr}} \tag{2.2}$$

and it will be always less than unity because of the presence of luminescence energy depleting processes [1].

2.2.4 Luminescence quenching

All the processes which contribute to the decrease of luminescence intensity of the luminophore, are defined as luminescence quenching phenomena [1]. This is due to the presence of excited state relaxation processes which occur without emitting photons such as static quenching, dynamic (collisional) quenching as well as energy transfer or electron transfer events. In case of static and dynamic quenching, the molecule of quencher and the luminophore have to be in contact in order to generate non-radiative processes. Static quenching is present when a non-luminescent complex between the molecule of quencher and a non-excited molecule of luminophore is created, which leads to a decrease in the luminescence intensity. Dynamic quenching occurs when the indicator molecule is in its excited state. By collision with quencher molecules, the luminophore returns to the ground state without emitting photons. As a consequence, a change either in the luminophore lifetime or its intensity can be observed.

Oxygen, one of the two analytes of interest in this work, acts as a quencher with regard to the emission of some luminescent complexes including the ruthenium complexes used here. Hence, a more detailed description of the dynamic quenching process and its application for oxygen sensing is discussed in section 2.3.3.

2.3 Optical Chemical Sensors

2.3.1 Introduction

Optical sensors became more widely used within the last decade due to their many unique features, some of which are listed below:

- No requirement for separate reference sensor

- Lack of electrical and electromagnetic interferences
- Appropriate for real-time monitoring of the analyte
- Energy-efficient
- Inexpensive
- Easy to miniaturise
- Non sample consuming

Having just few limitations coming from the fluorophore photobleaching and leaching which reduce sensor long-term stability and lack of compatibility with measurement of turbid samples, optical sensors found a wide range of applications in environmental and biomedical field. In this section an overview of oxygen and pH sensors is given together with main principles which lie behind optical oxygen and pH sensing. At the end, oxygen and pH-sensitive dyes are reviewed.

2.3.2 Overview of oxygen and pH sensors

The level of oxygen can be measured by several different techniques [3]. The traditional detection methods such as Winkler titration [4] and Clark electrode [5] are not always satisfactory, because of their time and analyte consuming nature respectively. A technique, which overcomes these limitations, is based on the optical detection of the luminescence signal, which is gradually quenched with increasing amount of oxygen. The luminophore is usually entrapped inside a hydrophobic oxygen-permeable matrix, which reduces dye leaching and minimizes possible interferences coming from the environment. Since the discovery of luminescence quenching phenomena in 1930's by Kautsky and Hirsch [6], many different matrices have been developed. Due to very good mechanical and chemical stability, polymers have become very popular in this application [7, 8]. Other candidates for luminophore immobilizing agent are sol-gel materials. In relatively simple way, the property of the matrix can be optimised for a particular application. For oxygen sensing hydrophobic, organically modified silicates (ORMOSILs) have been developed. Sol-gel derived materials have many advantages over polymeric matrices such as: higher chemical, mechanical and thermal stability as well as better optical transparency [9].

The most common device used for pH determination is the pH electrode. Despite many advantages such as simplicity of usage, cheapness and reliability, the electrode is not suitable for many applications because of its fixed size and design. Additionally drifting of the signal in time excludes the possibility of acquiring long-term measurements. As in the case of oxygen detection, an optical sensor provides an excellent alternative for pH measurements. The changes in pH are recorded based on the changes in the absorbance, luminescence or reflectance of the indicator molecules immobilized in a proton-permeable matrix. This simple (sensor) architecture facilitates the device miniaturization process and provides some flexibility in the design. The sigmoidal sensor response within a narrow dynamic range (±1.5pKa, where pKa is a negative logarithm of dissociation constant), results in high sensor resolution. Some attempts have been made to widen the dynamic range of the sensor by incorporating an indicator with two pKa values [10] or several indicators with different pKa values [11].

pH optical sensors have evolved in time from simple colorimetric strips [12], through fibre optic absorption-based sensors [13], in various luminescent pH indicators immobilized in different polymer [14-16] and sol-gel derived [17, 18] matrices.

2.3.3 Principles of optical O_2 and pH sensing

O_2 sensing

Oxygen, due to its small dimensions and neutral charge, which enable its fast diffusion and facilitate the probability of collision, is considered as a very efficient luminescence quencher [1, 19]. In an environment where more oxygen is present the quenching process will be more efficient therefore less luminescence of the indicator molecules will be observed. This dependence of luminescence signal from oxygen concentration has been applied here for oxygen sensing. The luminophores with longer lifetimes, such as ruthenium (II) complexes have become very popular in this application [20]. When the oxygen molecule collides with an excited ruthenium complex, the dye molecule returns to its ground state without luminescence emission and the oxygen molecule is brought from its triplet ground state to the excited state (Figure 2.3).

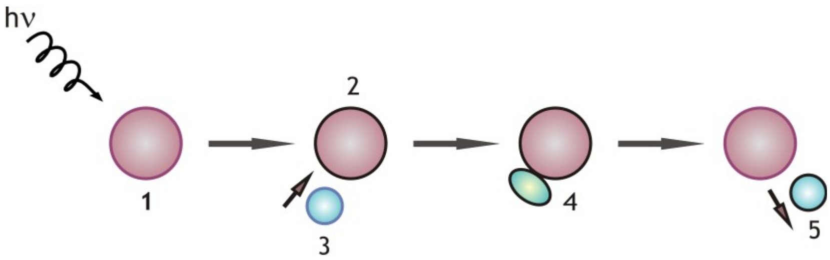

Figure 2.3: Schematic representation of the dynamic quenching phenomenon. 1 - luminophore in its ground state, 2 - luminophore in its excited state, 3 – quencher in its ground state, 4 - collision, 5 - quencher in its excited state.

As mentioned in section 2.2.1 ruthenium complexes belong to the group of transition-metal-ligand complexes (MLCs). The population of singlet and long-lived triplet states characteristic for this type of luminophores, results in the presence of an intersystem crossing. After absorption of photons, the electrons can be transferred from singlet excited states to the triplet states, from where a return to the ground state might occur once again by the quenching event or by non-radiative decay [21]. A schematic representation of this process is presented in Figure 2.4.

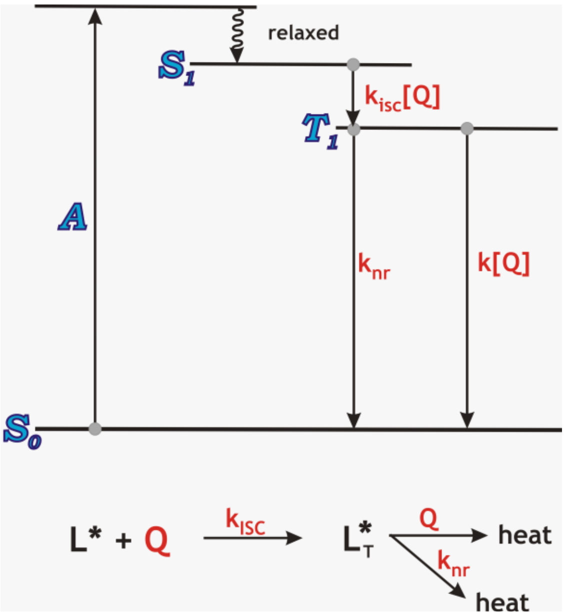

Figure 2.4: Simplified Jablonski diagram illustrating the mechanism of quenching by intersystem crossing. A - absorption of light, S_0 - singlet ground state, S_1 - first singlet excited state, T_1 - first triplet excited state, Q - quencher, k_{ISC} - rate of singlet to triplet intersystem crossing, k_{nr} - non-radiative decay rate, L* - luminophore in the excited singlet state, L^*_T - luminophore in the excited triplet state.

Due to a collisional character of the quenching process, the intensity and the lifetime of luminophore are strictly related to the partial pressure of oxygen, that is described by the Stern-Volmer equation (Equation 2.3) [22]:

$$\frac{I_0}{I} = \frac{\tau_0}{\tau} = 1 + K_{SV} \cdot pO_2 = 1 + k_q \tau_o \cdot pO_2 \tag{2.3}$$

$$K_{SV} = k_q \tau_0 = k_q (k_r + k_{nr})^{-1} \tag{2.4}$$

$$k_q = 4\pi g R^* ND \tag{2.5}$$

Where:

I_0, I - the luminescence intensity of the luminophore in the absence and presence of O_2

τ_0, τ - the luminescence lifetime of the luminophore in the absence and presence of O_2

K_{SV} - Stern-Volmer quenching constant

pO_2 - partial pressure of O_2

k_q - bi-molecular quenching constant

The lifetime of the luminophore is dependent on both radiative (k_r) and non-radiative decay rates (k_{nr}), as presented in Equation 2.4. The bi-molecular quenching constant is related to the diffusion coefficient, D (Equation 2.5), which results in dependence of the dynamic quenching process on the temperature. The other symbols in the above equation represent the spin statistical factor (g), the collision radius (R^*) and Avogadro's number (N).

Based on equation 2.3, the Stern-Volmer plot showing the dependence of I_0/I or τ_0/τ versus pO_2 can be drawn. In a homogeneous environment, this plot is represented as a straight line with a vertical intercept at 1 and slope equal to K_{SV}, which is used then as a value describing sensor sensitivity. In a lot of cases, microenvironment variations leads to different local quenching profiles, for which other non-linear models have been established [23-25]. When two different microenvironments with Stern-Volmer constants K_{SV1} and K_{SV2} are present in the luminophore-doped sensing matrix, the two-site Demas model can be applied to describe the quenching processes. This fitting is based on Equation 2.6 presented below:

$$\frac{I_0}{I} = \frac{\tau_0}{\tau} = \left[\frac{f_1}{1 + K_{SV1} \cdot pO_2} + \frac{f_2}{1 + K_{SV2} \cdot pO_2} \right]^{-1} \tag{2.6}$$

Although Demas [26] et al. found this model very useful to describe their data, the authors underlined as well that a lot of attention has been paid to avoid overinterpretation of the results.

pH sensing

pH sensing using optical detection usually relies on the change in the absorption or luminescence intensity under different hydrogen ion concentrations, that is presented in Figure 2.5.

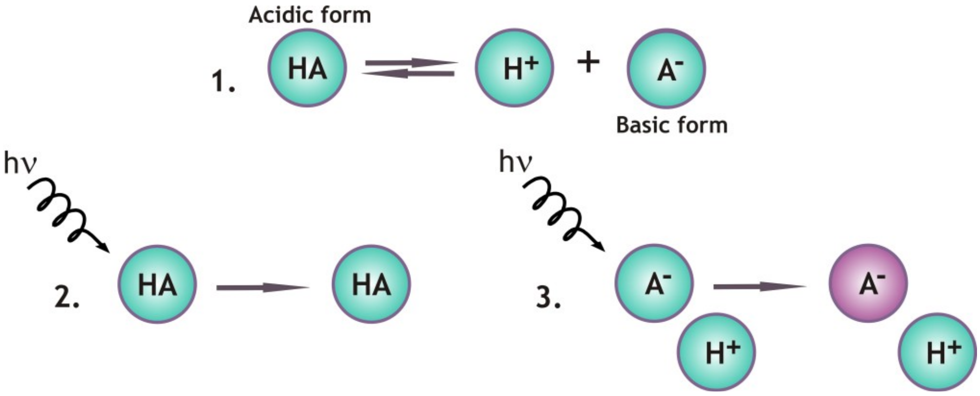

Figure 2.5: Schematic representation of luminescence-based pH sensing. 1 – pH indicator at equilibrium e.g., weak acid HA at equilibrium with its conjugate base A^-, 2 - protonated (acidic) form HA when excited does not change its luminescence properties, 3 - deprotonated (basic) form A^- changes its luminescence properties upon excitation.

By tuning the pKa value of the pH indicator to the pH range of interest, which should be approximately between ±1.5pH unit of the pKa, a pH sensor for a particular application can be designed. The value which is read by the optical sensor is equal to the concentration of protonated (acidic) and deprotonated (basic) form of the pH-sensitive fluorophore. For simplicity, in the first chapter, the general definition of pH was introduced in Equation 1.1. Focusing on the principles of pH sensing, this equation has to be modified to following:

$$pH = -\log a_{H^+} \tag{2.7}$$

where a_{H+} is hydrogen ions activity (or more precisely hydronium ions, H_3O^+). The activity of the ions is a function of not only their concentration but also it depends through the activity coefficient value f_{H+}, on the ionic strength of the environment, as presented in Equation 2.8

$$a_{H^+} = f_{H^+} \cdot \left[H^+\right] \tag{2.8}$$

Consequently, the Henderson-Hasselbalch formula (see Equation 1.5) can be written as:

$$pH = pKa + \log \frac{a_{[R-COO^-]}}{a_{[R-COOH]}} = pKa + \log \frac{c_{[R-COO^-]} \cdot f_{[R-COO^-]}}{c_{[R-COOH]} \cdot f_{[R-COOH]}} \tag{2.9}$$

This means that, for any pH measurement the ionic strength has to be defined. Moreover, the calibration plot and pKa value have to be measured at the same ionic strength and temperature as the final experimental conditions [27].

2.3.4 Luminophores for optical sensing of O_2 and pH

Luminophores for O_2 sensing

Oxygen sensing requires luminophores with a long decay time, which would enable monitoring the changes in the intensity or lifetime under different oxygen levels. Other features which have to be taken into consideration when choosing a complex for oxygen sensing are high quantum efficiency, analyte specificity, photo stability and chemical resistance. The first complexes used in this field which belong to the group of polycyclic aromatic hydrocarbons (PAHs), did not fulfil these criteria [28-30]. The achievements in organic chemistry significantly improved oxygen sensing capabilities. Complexes with lifetimes as long as thousands μs were synthesised, which significantly improved the oxygen sensor performance. The most popular oxygen indicators, together with their lifetimes and quantum efficiency, are shown in Table 2.1.

Table 2.1: Oxygen-sensitive luminophores and their optical properties.

Indicator	Unquenched Lifetime (μs)	Quantum Yield	References
($[Ru(dpp)_3]^{2+}$	6.3	0.35	[31,32]
($[Ru(phen)_3]^{2+}$	0.74	0.08	[31,32]
($[Ru(bpy)_3]^{2+}$	0.6	0.042	[31,33]
Pd-coproporphyrin	1200	0.2	[33,34]

Pt-coproporphyrin	100	0.4	[34]
Pd-meso-tetra-(4-carboxy-phenyl)tetrabenzoporphyrin-dendrimer	276	0.12	[35,36]
Pd-meso-tetra-(4-carboxyphenyl)porphyrin-dendrimer	738	0.1	[37]
Pd-meso-tetra(4-Carboxyphenyl)Porphine	705	0.06	[35]
$Ir(Cs)_2(acac)$	20.8	0.54	[38]

From the detection point of view, the long lifetime of these luminophores together with large Stokes shifts and high quantum efficiencies result in less expensive and simpler optics and electronics.

For this intracellular oxygen sensing investigation, the ruthenium complex [Ru(II)-tris(4,7-diphenyl-1,10-phenanthroline)]dichloride ($[Ru(dpp)_3]^{2+}$) was used. Its chemical structure together with the absorption and emission are presented in Figure 2.6 a, b.

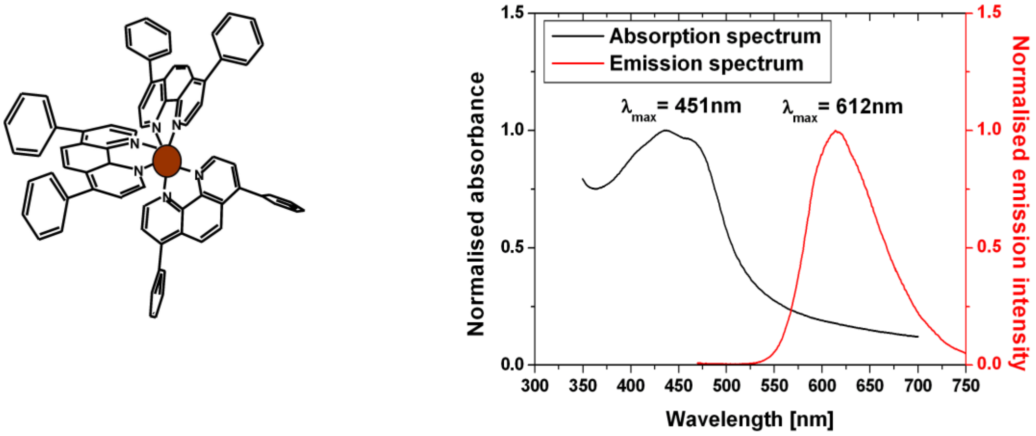

a) b)

Figure 2.6: a) Chemical structure [39], b) spectroscopic characterisation of $[Ru(dpp)_3]^{2+}$.

This luminophore, besides its good photostability and high quantum yield (~0.4), has several other features which are very attractive from the point of view of optical detection such as large Stokes shift (~150nm), absorption band in the blue region of the spectrum (~450nm), which makes it compatible with low-price light emitting diodes (LEDs) and, crucial in this oxygen sensing application, relatively long luminescence lifetime (~5μs under nitrogen saturated conditions) originating in its triplet-to-ligand charge transfer (MLCT) nature [22]. In addition, very low solubility of ($[Ru(dpp)_3]^{2+}$) in an aqueous environment significantly reduces leaching of the dye from the silica nanoparticles into the intracellular environment, which is a big advantage in this intracellular sensing application.

The other group of oxygen indicators used in the optical detection systems are the colorimetric dyes, mainly represented by haemoglobin [40], myoglobin [41] and redox dye-based complexes [42]. However these dyes have a narrow range of application due to their special storage requirements in order to keep them stable.

Luminophores for pH sensing

There are several criteria, which have to be considered while choosing the pH indicator, which are listed below:

- excitation and emission wavelength included between 405-550nm and 550-700nm, respectively
- large Stokes' shift
- pKa value matched to the application
- high quantum yield
- high photostability
- no cross-sensitivity to ionic strength and other analytes

The common pH indicators are based on the change in the absorbance spectrum. Examples such as phenol red [43], bromocresol green [44], bromothymol blue, cresol purple [45], congo red [46] and phenolphthalein [47] can be found in the literature. An alternative group of pH-sensitive complexes are luminescent-based indicators, which thanks to their better selectivity and sensitivity are more frequently used for optical sensing application. None of them however fulfils all of the desired criteria. Due to its low cost, lack of cross-sensitivity with oxygen, low cytotoxicity and improved photostability, 1-hydroxypyrene-3,6,8-trisulfonic acid (HPTS) is one of the most popular in this group [48] and it was chosen at the beginning for these studies. With a pKa value around 7.3, this luminophore is suitable for the sensing within cytosolic pH. The presence of the sulfonate groups in its structure results in very good solubility of this dye in water. This luminophore with two different absorption maxima (404nm and 455nm for acidic and basic form, respectively) and with one emission peak at 515nm belongs to a class of self-referencing dyes used for the ratiometric detection (see section 2.5.2).The big limitation, which have to be overcome when applying this dye for the intracellular measurements, is its lack of cell permeability. The strategies to deliver this dye to the interior of the cell include more invasive techniques such as microinjection and electroporation or encapsulation of the dye inside very dense, proton-permeable and cell membrane-permeable nanoparticle matrix, which would carry the pH indicator inside the cell. The other examples of pH-sensitive luminophores used for the intracellular measurements are carboxyfluorescein and its derivatives [49, 50] as well as seminaphthofluorescein (SNAFL) [51] and seminaphthorhodafluor (SNARF) [52]. The high quantum yield of carboxyfluorescein in basic environment together with a possibility of its covalent attachment to the surface of a sensor make it very attractive candidate for the cytosolic investigation. However moderate photostability of this dye, excludes its application for long-term monitoring of pH. In regard to SNAFL and SNARF indicators, these self-referenced fluorophores have many attractive features such as very limited dependence of their ratiometric properties on their concentration and the ionic strength of the intracellular environment, long wavelength excitation resulting in reduced cell photodamage and facilitated simultaneous detection as well as the possibility to bind them covalently inside the cell for the prolonged studies. The main drawbacks of these luminophores are their low quantum yield and a high cost. The latest examples of pH-sensitive dyes are more photostable iminocoumarin and lipophilic fluorescein derivatives, pH probes with multiple pKa values from 1.7 to 9.0 excitable with UV as well as pH-sensitive ruthenium metal-ligand complex and lanthanide.

2.4 Silica nanoparticles for intracellular sensing

2.4.1 Introduction

In this section silica nanoparticles and their application for monitoring oxygen and pH inside the cell are described. The advantages of miniaturization of the optical sensor to nanometre dimension, especially important in the cellular context, are presented first. This is followed by a State of the Art review of oxygen and pH nanosensors. The technique used in this work to synthesise nanoparticles is then introduced. The last section contains a brief description of organically modified silicates (ORMOSILs) and their application for oxygen sensing.

2.4.2 Optical Nanosensors for intracellular measurements

Live cell imaging and intracellular sensing are of great importance for early diagnosis and therapeutics applications [53]. Real-time, non-invasive monitoring of processes occurring at the cellular level is not achievable by traditional optical and electrochemical sensors. For a long time the only insight inside the cell was due to analyte-specific luminescent molecular probes, which, coupled with high-resolution microscopic techniques, have provided much valuable information about biological processes. The diffusion problem, derived from sequestration of dye molecules to specific cellular compartments and their non-specific binding inside the cell, as well as other limitations associated with intensity-based measurements (i.e. photobleaching, fluctuations in source intensity), make impossible to quantify the intracellular measurements. In order to overcome these problems, optical nanosensors, named by Kopelman group as PEBBLE: photonic explorer for bioanalysis with biologically localized embedding [54, 55], have been developed. This new group of sensors is based on nanoparticle design, where luminescent molecules are incorporated inside an inert protective matrix, which minimises the possibilities of non-specific binding between proteins and molecules of the indicator dye as well as prevents potentially toxic interactions between the cellular components and the encapsulated organic compound. Due to their small dimension (20-600nm), the spherical nanosensors occupy from 1ppm to 1ppb of the mammalian cell volume, which make them relatively non-invasive and can help them evade the immune system. Other important features of nanoparticles from the bioimaging and biosensing point of view are:

- High surface-to-volume ratio, thus enhancing the accessibility of analytes/targeting factors towards indicator dyes/specific cells or compartments of cells
- High loading efficiency (both inside the NP matrix and on the surface), resulting in signal amplification
- Possibility of loading more than 1 dye into the matrix, enabling encapsulation of indicator and reference dye for ratiometric measurements and multi-analytes analysis
- Capability of targeting of nanoparticle to the location of interest by coating their surface with proteins and peptides [56]

Since PEBBLEs invention in 1990s, significant progress has been made in the nanoengineering field. Many different types of nanosensors are used at present for bioimaging and biosensing applications including silica and polymer nanoparticles, lanthanide nanoparticles, magnetic nanoparticles, metallic nanoparticles as well as quantum dots which are famous for their unique size-dependent emission properties [53].

This work focuses on the use of silica NPs, whose properties due to the versatile silica chemistry, can be easily adjusted for analyte-specific application. In addition, the negative charge on the surface of silica nanoparticles and the ease of surface modification makes them very attractive in nanotechnology. With these features, nanoparticles can bind in many ways to different bio-recognition agents such as antibodies, protein complexes, nucleic acids and many others. They can also be doped with a wide range of positively charged molecules by electrostatic interactions [57]. The optical transparency of the silica protective layer is an important aspect for detection of the embedded dye luminescence as the dye spectrum is not altered to any large extent by the matrix. The photostability of the dye is also enhanced by its incorporation in the silica matrix [58]. Other features of the silica matrix which are important for in vivo applications are dispersibility in water, resistance to microbial attack and lack of influence of solvent polarity on nanoparticle size.

Despite these numerous advantages, much research is still required before these new probes can be introduced onto the market. There is still a limited understanding of the nanoparticle behaviour in biological systems. Questions regarding the detailed interaction of nanoparticles with the organism and toxicity effects have not yet been answered. However the vision of early detection of diseases is a powerful engine for the robust toxicological investigation, which hopefully will facilitate the implementation of nanotechnology in the biomedical field in the very near future [59, 60].

2.4.3 O_2 and pH-sensitive nanoparticles – state-of-the-art

Although the mechanism of optical oxygen sensing is well known and many oxygen sensors have been developed (see section 2.3.2), sensing of oxygen inside the cell still remains cumbersome [61]. The issues related to the intracellular delivery of the sensor and its calibration, ideally performed inside the cells, make quantitative oxygen studies very challenging. The first dissolved oxygen nanosensor applied in the intracellular environment was developed by the Kopelman group in 2001 [62]. This ratiometric sensor composed of an oxygen-sensitive ruthenium complex and Oregon Green 488-dextran as a reference dye embedded into silica matrix, was introduced into C6 glioma cells and measurements of oxygen inside the cells were successfully performed. The sensitivity of this sensor, expressed by the quenching response to dissolved oxygen (Q_{DO}), was calculated to be equal to 80%, based on the equation:

$$Q_{DO} = \frac{I_{N_2} - I_{O_2}}{I_{N_2}} \times 100\% \tag{2.10}$$

where I_{N2} is the luminescence intensity of the oxygen-sensitive luminophore in the absence of oxygen and I_{O2} is the luminescence intensity in the oxygen-saturated environment. In the case of ratiometric measurements, the symbol I stands for the ratio of luminescent indicator to the reference dye intensities. A few years later, the same group have exploited the concept of organically modified silicates (ORMOSILs) and silicones for nanosensing applications. This novel approach resulted in the fabrication of nanoparticles with a hydrophobic matrix consisted of phenyltrimethoxysilane (PTMS) and methyltrimethoxysilane (MTMS) [63] or polydecylmethacrylate (PDMA) [64]. Apart from the change in the matrix, the ruthenium complex was exchanged with the platinum (II) octaethylporphine, which due to its much longer lifetime (60-90 μs) and unaffected by the light scattering and auto-fluorescence infrared emission is more suitable for this oxygen biosensing application. For these hydrophobic nanosensors, the highest sensitivity to dissolved oxygen was achieved (Q_{DO}=97%). Other matrices for dissolved oxygen sensing were developed based on polyelectrolyte layers [65] and liposomes [66], both doped with ruthenium complexes; however, the quenching responses of these nanosensors to dissolved oxygen were much lower than the ones measured for platinum-doped nanoparticles (Q_{DO} equal to 60% and 76% respectively). Additionally, the nanoparticles made from a hydrophobic copolymer of styrene and vinylpyrrolidone which can host a wide range of oxygen-sensitive luminophores (with a hydrophilic poly(vinylpyrrolidine) shell) have been reported in the literature [67].

In parallel to ratiometric luminescence-based measurements, different optical techniques employing the luminophore lifetime [68-71] and luminescence anisotropy [72] have been investigated.

Beside oxygen sensitivity, an important feature of the intracellular nanosensor is its ability to penetrate the cell membrane without any physiological disruption. A big improvement has been made in this area since the creation of first PEBBLEs, which were introduced to the cell by a gene gun technique [73]. Papkovsky et al. developed the strategy of self-loading oxygen sensors with the cell-penetrating peptides, which when conjugated with Pt(II)-coproporphyrin oxygen-sensitive molecules of dye were transported inside the cell. This concept then was adapted into the field of nanosensing, where ratiometric luminescent nanoparticles were coated with these peptides [74] or with amino groups [75] in order to facilitate their cellular uptake. Some limitations of these probes, such as variations in the nanoparticle uptake between different cell lines and issues related to photostability and brightness, have been overcome by incorporation of a platinum complex into a cationic polymeric nanoparticle matrix. The positive charge of the nanosensor allows it to easily penetrate through the membrane, which results in similar cell loading efficiency for different mammalian cell types. The long-lifetime phosphorescent dye with its high photostability and brightness contributes to the high performance of the nanosensor. Up-to-date, the studies presented by

Papkovsky et al. have shown the greatest potential for this intracellular oxygen investigation.

As with oxygen, the first pH nanosensors derive from the Kopelman group and they belong to the category of polymeric PEBBLEs. Different pH indicators (i.e. fluorescein and its derivatives, SNAFL) and the internal standard sulforhodamine 101 were entrapped within acrylamide nanoparticle matrices for the ratiometric intracellular measurement [73, 76]. The performance of these nanosensors was highly reduced by leaching of dye molecules from the matrix (45% within 48 hours) [77], which led to their cytotoxicity and unsatisfactory calibration, due to the presence of free dye molecules in the cell and different leaching rates for the indicator and reference dye respectively. To overcome this problem, Rosenzweig et al. covalently attached amine-reactive forms of pH-sensitive Oregon Green and pH insensitive Texas Red to the surface of submicrometer polystyrene nanoparticles, which were then introduced to a macrophage cell line through a phagocytic pathway [78]. These nanoparticles, with a dynamic range between 4.5 and 7.0 and sensitivity of 0.1 pH units, were able to detect the change in lysosome pH from 4.8 to 6.5 under chloroquine stimulation. However, unshielded molecules of the luminophores were still in contact with intracellular components and their rate of photobleaching was comparable to that of free dye molecules. The next improvement was to inertly bind luminophores inside the nanoparticle structure through covalent attachment, which was demonstrated by Sun et al. [77]. In this work, a fluoresceinamine and rhodamine B derivatives were modified with acrylamide functional group and incorporated inside the hydrophilic polyacrylamide nanoparticles. The same strategy was applied for the silica nanoparticles. The Wiesner group synthesized a nanosensor, where a reference and sensor dyes were spatially separated in a core/shell nanoparticle construct. In this way the interaction between the sensing dye located within a shell and the hydrogen ions could occur without any interferences from the core-bounded molecules of the reference dye [79]. Other examples of this successful approach can be found in the literature [80, 81]. The luminescent pH nanosensors have a limited pH measurement range determined by pK value of the sensing dye. Recently, Aylott et al. developed pH nanosensors with tuneable pK and extended dynamic range. By incorporating two pH-sensitive fluorophores and a reference dye inside polymer nanoparticles, they were able to increase the effective dynamic range of the nanosensor from 1.15 pH units up to 2.01 pH units, which could be applied for simultaneous intracellular measurements of pH within basic cytoplasmic and acidic endosomal cell compartments [83]. The same group had several other achievements in the synthesis of pH nanosensors, which includes clickable sensing polymeric nanoparticles [84] and incorporation of pH-sensitive dyes into a nanocrystal structure [85]. All above examples of pH-sensitive nanosensors use optically inert materials for the nanoparticle matrix. To increase the brightness and optical functionality of nanosensor, a novel category of nanomaterial based on fluorescence resonance energy transfer (FRET) was designed. Semiconductor quantum dots (QD) and polymer dots (Pdots), coupled to pH-sensitive dyes, have been reported [86]. The last examples of pH-sensitive nanoparticles derive from the class of the Surface-enhanced Raman scattering (SERS) nanosensors, which being free from photobleaching and auto-fluorescence issues, are very promising candidates for intracellular studies [87,88].

2.4.4 Nanoparticle synthesis – Stöber process

In 1968 a German chemist, Werner Stöber, published his revolutionary work on the synthesis of mono-disperse silica spheres. The first one who observed the formation of the particles, as a result of mixing tetra alkyl silicates in alcohol with water under basic conditions, was Kolbe [89]. Stöber however made a detailed investigation of this process and he succeeded in achieving controlled growth at sub-micron nanoparticle size [90]. Since that time, other synthesis routes such as micro-emulsion [91] and silicon-based methods [92] have been established. However, the Stöber synthesis remains the simplest and most efficient one in comparison to others, where large amount of surfactants and time-consuming preparation of the reactants are the big limitations from the industrial/mass production point of view [93].

The following steps can be distinguished in the Stöber-based nanoparticle synthesis:

- Hydrolysis of the suitable metal alkoxides in the basic environment:

  $$Si(OR)_4 + nH_2O \rightarrow Si(OR)_{4-n}(OH)_n + nROH \qquad (2.11)$$

- Water (1) and/or alcohol (2) condensation phase

  1) $$\equiv Si\text{-}OH + HO\text{-}Si\equiv \; \rightarrow \; \equiv Si\text{-}O\text{-}Si\equiv + H_2O \qquad (2.12)$$

2) $\equiv Si\text{-}OR + HO\text{-}Si\equiv \rightarrow \equiv Si\text{-}O\text{-}Si\equiv + ROH$ (2.13)

- Formation of nanoparticles

There have been two proposed models to explain nanoparticle formation according to the Stöber process. The first is the monomer addition model which divides the Stöber process into two stages: nucleation generation and particle growth, being a result of addition of hydrolysed monomers to the polymer's surface [94, 95]. The controlled aggregation model is the second possibility which describes the formation of silica nanoparticles; it excludes the nucleation phase and predicts the grouping of sub-particles into the final particles [96-99]. Even if the exact mechanism is not clear, there is a lot of experimental data which shows a strong influence of water-to silane ratio and the nature and concentration of the catalyst and the metal alkoxides on the relative rates of hydrolysis and condensation. As a consequence, the control of the physical properties of nanoparticles such as average pore size, pore shape and NP surface area can be established [100]. There is, however, one limitation which has to be taken into consideration when designing bioimaging nano-probes and sensors which is that many biomolecules denature in the presence of alcohol and in high pH conditions. This is not an issue for the nanoparticles which are used as optical chemical sensors in this work. [101].

2.4.5 ORMOSILs and their application for oxygen sensing

Organically modified silicates (ORMOSILs) are inorganic-organic hybrid materials which, due to the same mechanism of formation as for the Stöber –based nanoparticles, belong to the same group of sol-gel derived materials [102]. The introduction of additional organosilicon results in better control of the chemical and physical parameters of the final product [103]. Following Sanchez and Ribot [104], ORMOSILs materials can be divided into two classes: embedded and grafted materials, depending on their method of formation. The materials where the organic and inorganic components are simply mixed and, in the process of co-condensation, combined together, belong to the first class. The other category corresponds to materials where the hybrid formation is facilitated by the chemical bonding between organic and inorganic compounds. The scheme of the reaction is very similar to the one in section 2.4.4

describing the Stöber process; basic hydrolysis of metal alkoxides and organoalkoxysilanes defined in sol-gel terminology as precursors, followed by their co-condensation reaction and finally nanoparticle formation. The simplified synthesis route is presented below:

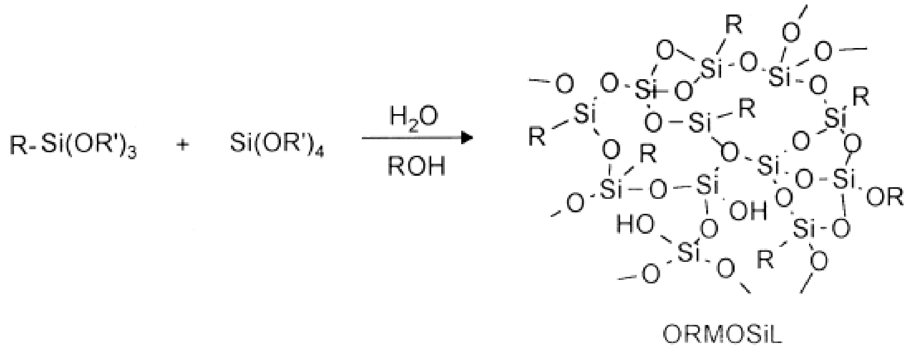

Figure 2.7: ORMOSIL formation [105].

Where R_{4-n} Si(OR′)$_n$ - organic precursor

R - desirable functional group (e. g.:CH_3, C_6H_5, $CH_2CH_2CH_2SH$)

$1 \leq n \leq 3$.

ORMOSIL nanoparticles, in comparison to the pure inorganic Stöber–derived compounds, possess many advantages some of which are listed below:

- Larger pores in the matrix , which allows for controlled biomolecule release
- Possibility of loading either hydrophilic or hydrophobic dyes/drugs and, as a consequence, improvement in the quantum yield of photoluminescence and facilitating therapeutic applications for a wider range of treatable diseases
- Expanded range of surface functionalization variants with different chemical groups
- Improved biocompatibility [106]

For dissolved oxygen sensing, due to their increased hydrophobicity and porosity of the matrix, ORMOSIL nanoparticles provide a better linearity as well as sensitivity of the sensor [63], which makes them a good candidate for this application.

2.5 Optical sensing techniques for monitoring intracellular O_2 and pH

2.5.1 Introduction

Luminescence has been used in order to study changes in concentration of the analyte. The measurements have been based on two different luminescence features: the intensity and the lifetime. Direct unreferenced luminescence-intensity detection has many drawbacks such as sensitivity to external perturbations coming from the light source and detector, inner filter effects, as well as change in the signal caused by leaching and photobleaching. To eliminate these effects, ratiometric and lifetime-based measurements have been utilized in this study and these techniques are briefly described in the following subsections.

2.5.2 Ratiometric measurements

The use of an analyte-independent reference dye, in conjunction with the sensing dye, can counteract some of the disadvantages of intensity-based sensing. Ratiometric measurements are independent of instrument fluctuations and dye concentration as well as leaching and photobleaching [63]. The measurements can be performed in three different ways:

- two excitation and one emission wavelength detection
- one excitation and two emission wavelengths detection
- two excitation and two emission wavelengths detection

An application of the dye with two different emission peaks, one dependent and another one independent on the analyte concentration, is very convenient for this ratiometric approach. In this case only one fluorophore is present in the sensing matrix, what results in a more facile synthesis route and excludes the changes in the intensity ratio due to either fluorophore leaching process or difference in the photostability between two different fluorophores.

2.5.3 Luminescence lifetime-based measurements

2.5.3.1 Phase fluorometry

The phase fluorometry method is a time–resolved luminescence technique. Because this is an indirect lifetime-based method, it has many advantages over unreferenced intensity measurements such as the possibility to resolve the emission from more than one dye, to distinguish between static and dynamic quenching, to carry out resonance energy transfer investigation, and**,** in particular, for cellular imaging there is no dependence on dye concentration, photobleaching or leaching effects. To carry out the measurement, the excitation beam is modulated usually with a sinusoidal wave at a frequency *f***,** so that its reciprocal would be comparable to the decay time of the dye τ. Hence, the resulting emitted light will have the same frequency *f* as the incident beam and will be also time delayed or phase-shifted relative to the excitation signal as presented on Figure 2.8.

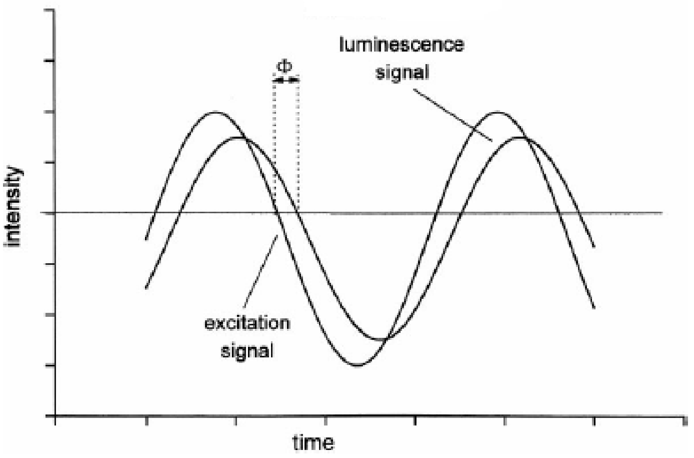

Figure 2.8: Phase shift used in phase fluorometry technique [107].

The lifetime therefore can be calculated from the equation:

$$\tau = \frac{\tan \phi}{2\pi f} \tag{2.14}$$

where Φ is a phase shift . The time of response for the sample is finite and determined by the dye lifetime. This time delay results in demodulation of the emission by a factor m_ω, defined by the equation:

$$m_{\omega} = \frac{B / A}{b / a} \tag{2.15}$$

where:

a – average intensity of the incident light

b – peak-to-peak height of the incident light

A - average intensity of the emission light

B – peak-to-peak height of the emission light

There are two factors which have to be taken into consideration:

1. decrease of the signal to noise ratio (SNR) with increasing modulation frequency
2. increase of the phase sensitivity with modulation frequency

The crucial step therefore for the phase fluorometry measurements would be to find an optimal modulation frequency for the particular dye which is consistent with its lifetime. The electronics for this method is relatively cheap and employs a light-emitting diode (LED) to excite the sample and a photodiode (PD) with amplifiers for a collection of the signal [108-110]. Note that this technique was used only to calibrate the nanosensors outside of the cell environment. The techniques used in the following sections were used for the cellular sensing.

2.5.3.2 Time-correlated single-photon counting (TCSPC)

The Time correlated single photon counting (TCSPC) method is a time–resolved technique implemented in the time domain mode. This means that the dye is excited, not as in the previous case by a sinusoidally modulated beam, but using a pulsed laser source [108]. As the name implies, this technique measures one photon per excitation pulse. To fulfil this condition the photon count rate must be lower than 1% of the excitation pulse frequency. A schematic, which shows the principle of this detection method, is presented in Figure 2.9.

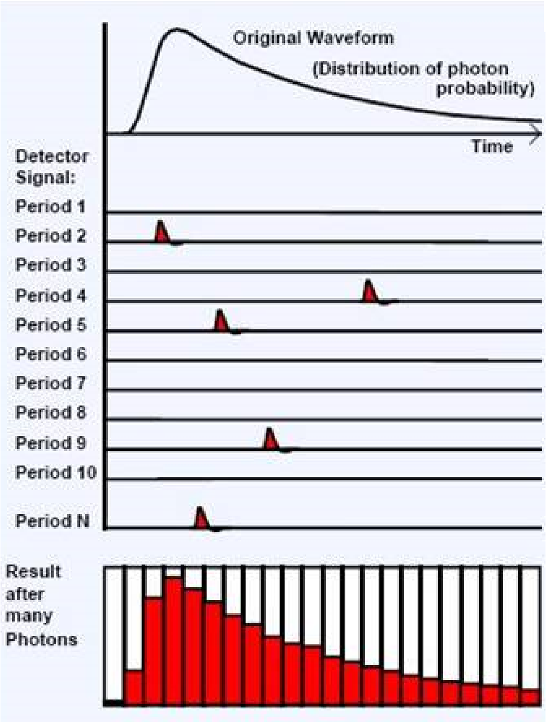

Figure 2.9: Principle of TCSPC method [111]

The photons are collected into the different acquisition channels determined by the time between the excitation pulse and photon emission. In Figure 2.9, the fluorophore decay spectrum is shown only when much less than 1 photon is detected per excitation pulse. For higher count rates, false shorter lifetimes will be detected, due to limitations in the electronics, which is unable to measure multiple photons per pulse. When many photons arrive at the detector only the first one is counted, resulting in deformation of the intensity decay and shortening of the lifetime. As for the previous frequency domain technique the lifetime of the dye is closely related to the pulse rate of the excitation wave; for TCSPC technique the laser pulse width should be comparable to the lifetime, which usually is in the nanosecond time scale. Therefore this method requires expensive electronics such as high repetition rate mode-locked picoseconds (ps) or femtoseconds (fs) light sources and for signal collection a high-speed micro-channel plate (MCP) photomultiplier tubes (PMTs) [111]. The long lifetime of oxygen-sensitive luminophores (from μs to ms) is a big limitation for this technique, as longer lifetimes require longer pulse rates with subsequently lower count rates and therefore require longer acquisition times. Cellular experiments would require high frame rates in order to monitor the intracellular processes. The data can still be acquired for longer lifetime luminophores, however higher count rates have to be applied in excess of the ideal 1-5% limit, and only part of the decay curve can be monitored in the image reconstruction process. Under these conditions there is a high probability of photon arrival events going undetected and the full TCSPC histogram cannot be accurately constructed. Nevertheless, any changes in the lifetime of the luminophore should be detected and although not ideal, qualitative information can be obtained.

2.6 Optical imaging techniques

2.6.1 Introduction

Recent research and development in genomics and molecular biology has uncovered new exciting opportunities in the area of pharmacology and medicine. The need to have an insight into what is going on inside the cell and, for example, into how the molecules of a drug interact with living cells, was a driver for the development of high resolution imaging techniques. The synthesis of new luminescent labels together with the non-invasive character of virtual sectioning of the specimen made optical techniques very attractive candidates for biomedical studies [112]. The introduction of new, intense light sources and advances in digital imaging and analysis allowed fast simultaneous imaging of different luminescent labels inside biological samples up to 100μm thick [113]. Optical microscopy evolved during this time from conventional wide-field microscopes which suffered from “out-of-focus” light decreasing the quality of the image up to the super-high resolution techniques such as stimulated emission depletion microscopy (STEM), photo-activated localisation microscopy (PALM) or stochastic optical reconstruction microscopy (STORM). In this intracellular sensing study, laser scanning confocal microscopy (LSCM) and fluorescence lifetime imaging microscopy (FLIM) were used and the general concepts behind these techniques are discussed in this section.

2.6.2 Confocal microscopy

Using a conventional epifluorescence microscope, the incident light is directed onto the entire specimen, which leads to emission of the overall luminescence from the sample. It results in a blurred image of the region of interest derived from the photons coming from the out-of-focus light. In confocal microscopy, this effect is reduced up to a certain level determined by the limit of diffraction by introducing a focused coherent excitation beam together with pinhole apertures for the light source and detector. In this way, improved spatial resolution is achieved (up to a factor of 1.4) and extremely thin (0.5 to 1.5 micrometer) optical sections can be detected. A general confocal microscope setup, presented in Figure 2.10, consists of one or more lasers, a scanning head with optical and electronic elements, a detecting unit usually composed of photomultipliers and a computer for final acquisition and display of the data.

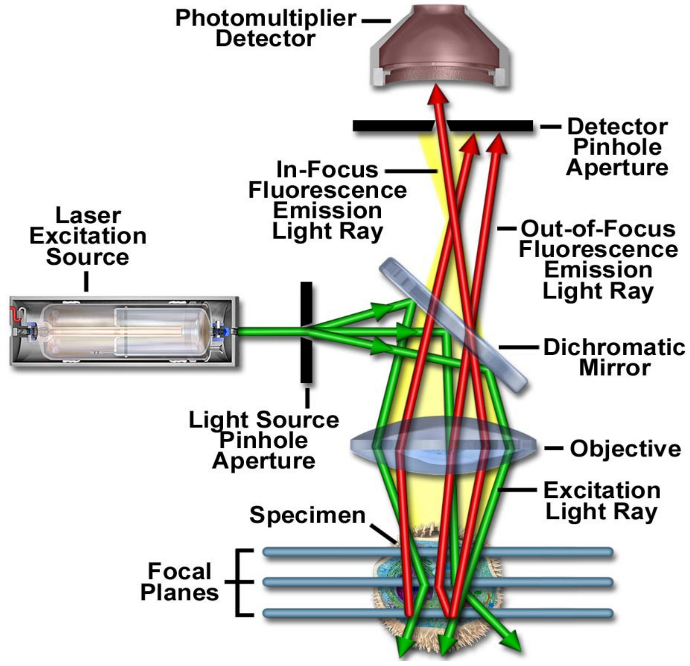

Figure 2.10: Confocal microscopy schematic [113].

The scan head of the microscope is moved across the (x,y) plane and the image is recorded using a point-by-point and line-by-line raster. The optical sectioning of the sample enables 3D reconstruction of an object of interest, which makes confocal microscopy very attractive especially in imaging of biological samples.

2.6.3 Fluorescence Lifetime Imaging Microscopy (FLIM)

Fluorescence Lifetime Imaging Microscopy (FLIM) is another technique which can be used to track the changes in complex biological systems. Unlike conventional intensity-based microscopy, as mentioned previously, lifetime measurements are insensitive to many factors such as dye concentration, photobleaching, as well as variation in excitation source intensity, gain of the detector, signal loss within the optical path or specimen, and microscope focusing. This makes FLIM measurements much more attractive in the field of intracellular imaging and sensing, where equal distribution of dye across the biological specimen is very challenging if not impossible to achieve. As molecules of dye are exposed to different microenvironments, the change in lifetime can be detected. This allows the monitoring of a range of important cellular parameters including temperature, pH, oxygen and ion concentration and molecular interactions occurring within the cell.

FLIM measurements can be divided into two categories: time–domain and frequency-domain techniques. The first one uses a pulsed laser to excite the sample and then luminescence lifetime decay is reconstructed in time. In frequency-domain FLIM the excitation source and/or detector are modulated and the lifetime is calculated from the demodulation and the phase shift of the emitted luminescence. Both of these techniques have their strong and weak points, which have to be taken into consideration in deciding about the experimental setup. The measurements done in time-domain FLIM are usually based on TCSPC technique, described in section 2.5.3.2. Very good signal to noise ratio and excellent picosecond resolution are very attractive features of this technique; however, time-consuming image acquisition can be a huge limitation in detecting dyes with long lifetimes. The frequency-domain measurements do not have the long data acquisition problem due to their high photon efficiency detection. There is also no need to deconvolute the instrumental response and the luminescence decay. However, data analysis of stretched exponential decay can be an issue on the way to obtaining accurate results.

2.7 Cellular sensing

2.7.1 Introduction

To maintain cellular homeostasis, the human body is continuously monitoring the level of the analytes which are crucial for proper functioning. Precise control over all physiological parameters requires a sophisticated network of very precise internal sensors. Since oxygen combusts the fuel that runs the human body in the process of the oxidative phosphorylation (described in section 1.2), oxygen sensing is a fundamental biological process which allows the organism to adapt and survive in continuously changing environmental conditions. A decrease in the availability of oxygen, defined as hypoxia, can result in two different types of response: acute and chronic. Acute response occurs over a timescale of seconds to minutes and is related to the ion flux through the channels located in the cell membrane which influences cell excitability, contractility, and secretory activity. When hypoxic conditions exceed the limit of a few minutes, the organism's response will be chronic. At this stage, due to activation of the hypoxia-inducible transcription factors (HIF), changes will appear at molecular level, which induce modifications in gene expression of numerous enzymes, transporters and growth factors [114]. The oxygen distribution within the body is heterogeneous, therefore the critical oxygen tension will vary between the organs and tissues (21% O_2 in the atmosphere, 14% O_2 in the alveolar air, 12% O_2 in the arterial blood, 5,3% O_2 in venous blood, 3% O_2 in tissues and 1-5% O_2 in interstitial mammalian brain tissue) [115]. Different hypotheses have been proposed to explain how the human body maintains oxygen homeostasis. Nevertheless further investigations with more sophisticated tools are required in order to decide on one coherent oxygen sensing and regulation model. It is known, however, that mammalian cells react to decreased oxygen levels at the systemic level by rapid stimulation of breathing and increase in blood pressure in order to maintain normal oxygen tension in vital organs. A crucial role is played here by the chemoreceptors, specialised nerve cells, responsible for monitoring even slight changes in oxygen concentration which are localised in the carotid bodies present in most tissues, as well as the less well-studied neuro-epithelial bodies in the lung [115, 116]. Under hypoxic condition, these cells release transmitters what leads to the depolarisation of nearby afferent nerve endings and an increase in sensory discharge. The transduction process that triggers transmitter release is not yet well understood. It has been suggested that hemeprotein plays a role and that cytochrome b-like NAD(P)H oxidase might be an attractive candidate for this protein. The hydrogen peroxide (H_2O_2) produced by this cytochrome b acts as a second messenger in regulating potassium channels and gene expression involved in hypoxia response [117].

Another important analyte for the human body is the intracellular pH. The control over this parameter is strictly connected to the process of respiration and CO_2 concentration. When dissolved in the blood, CO_2 is rapidly converted to carbonic acid, which then dissociates into a proton and a bicarbonate ion. An increase in ventilation would lead therefore to an increase in the proton concentration and a subsequent decrease in extracellular pH. As with oxygen sensing, the chemoreceptors located within the body are responsible for CO_2 and pH detection. In order to maintain the body homeostasis, the level of CO_2 has to be kept constant in the blood at 40mmHg. Even small deviations from this value, originating both from the respiratory route and from cellular metabolic disruption, will cause the organism to try to compensate by a change in the respiration rate. Extracellular changes in pH would lead to corresponding intracellular changes in proton concentration. The cell, in trying to maintain a constant value of cytosolic pH, would respond by activation of ionic pumps, which would transport the excess protons outside or inside the cell. The detailed mechanism of this intracellular pH regulation is described in reference [118] by Nattie et al.

2.7.2 Mechanism of oxygen sensing

2.7.2.1 Mechanism of oxygen sensing at the systemic level

Three steps can be distinguished in the hypoxia sensing process:

1. detection of the decrease in level of oxygen by carotid bodies and as a consequence, inhibition of potassium channels in the cell membrane

2. depolarization of the cell membrane and activation of voltage-dependent calcium channels; calcium influx

3. exocytosis of neurotransmitters, transduction of the signal to the respiratory center, hence increasing lung ventilation (Fig 2.11.)

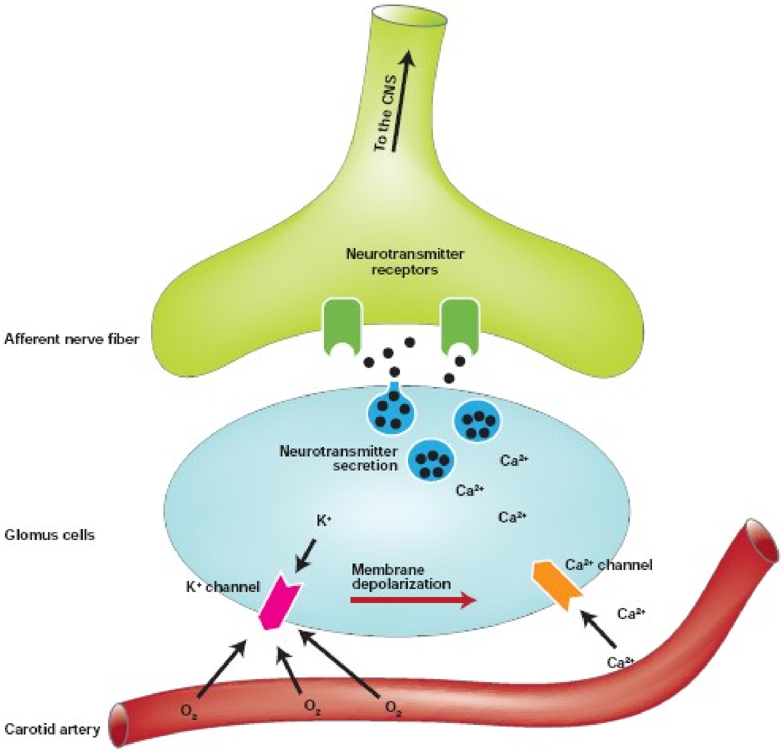

Figure 2.11: The oxygen sensing mechanism at the systemic level [116].

The neurotransmitters released at the end of the sensing process are classified into two groups: “conventional” and “unconventional”. Neurotransmitters, such as acetylcholine (ACh), ATP, catecholamines and others, which undergo the exocytosis process from the synaptic vesicles, belong to the first group. The “unconventional” group consists of neurotransmitters generated by enzymatic reactions such as gas signalling molecules: nitric oxide (NO) and carbon monoxide (CO) [116].

2.7.2.2 Mechanism of oxygen sensing at the molecular level

As was discussed in section 2.7.1, molecular level interactions associated with hypoxia are not well understood. However, a general oxygen sensing model which is illustrated in Figure 2.12 has been proposed [119].

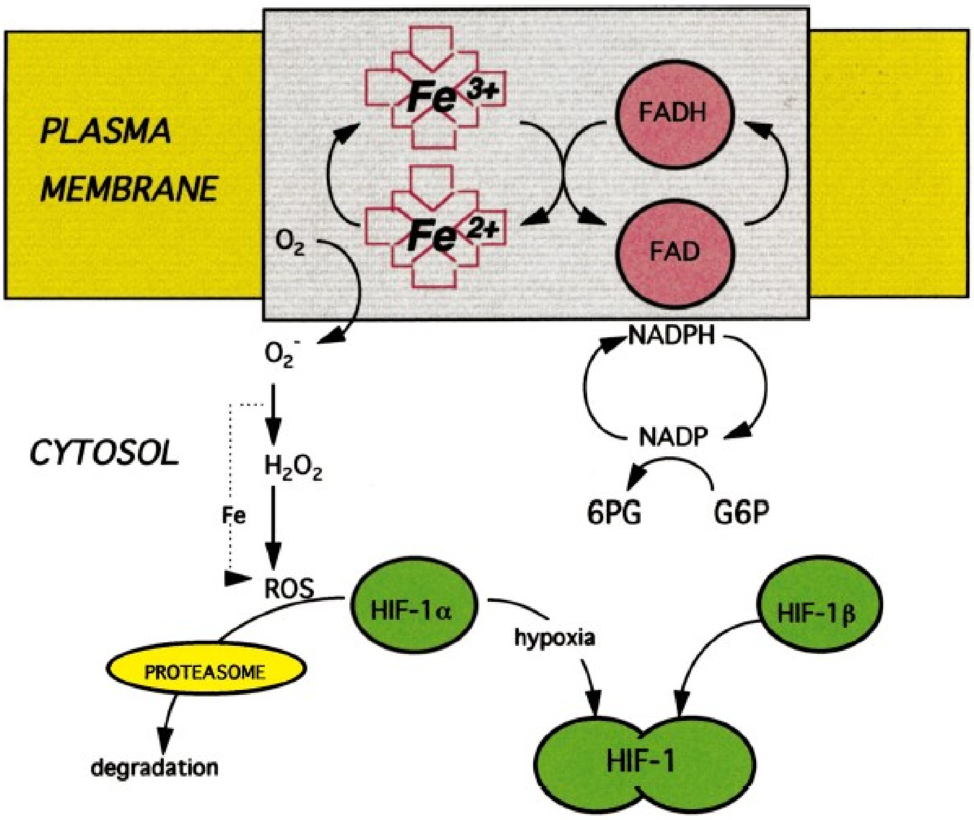

Figure 2.12: The proposed oxygen sensing mechanism at the molecular level [119].

It is proposed that the main sensing element is a cytosolic, membrane bound, multisubunit b-like cytochrome, containing a flavo-heme protein in the plasma membrane. This protein, which may behave as a nicotinamide adenine dinucleotide phosphate-oxidase (NADPH oxidase), transfers the electrons through flavin and heme to molecular oxygen, which gives as the final product the superoxide O_2^-. This superoxide is converted, in the presence of free iron, to a reactive oxygen species (ROS), which is essential in the activation of hypoxia-inducible factor (HIF-1) and for hypoxia inducible gene expression [119]. HIF-1 is a heterodimeric transcription factor, which is described by Semenza as “the master regulator of oxygen homeostasis” [120]. It maintains control over the cellular oxygen level by regulating the transcription of genes involved in adaptation to reduced oxygenation conditions. It is composed of two dimers: α-subunit (HIF-1α) and β-subunit (HIF-1β). Under normal oxygen conditions, which are defined as normoxia, these subunits are separated due to ROS-initiated degradation of HIF-1α by the proteasome. When the level of oxygen decreases, the HIF-

1β remains unaffected, while the abundance of HIF-1α significantly increases due to the ROS deficit. The translocation of the HIF-1α subunit to the nucleus occurs, where it creates an active transcriptional complex with HIF-1β [121]. This leads to up-regulation of more than 50 genes which encode the synthesis of the hypoxia-response proteins, such as for example erythropoietin (Epo), vascular endothelial growth factor (VEGF) [122], NO-synthase [123] and haem oxygenase [124]. An improved understanding of these processes in the future will, no doubt, contribute greatly to the fight against cancer as well as many cardiovascular and cerebrovascular diseases [125].

2.7.3 Mechanism of pH sensing

The cell is able to maintain the pH value at a constant level by employing ion pumps located in the membranes to transport ions in or out of the cell and intracellular organelles. This intracellular ionic transport relies on a system of different so called acid extruders and acid loaders.

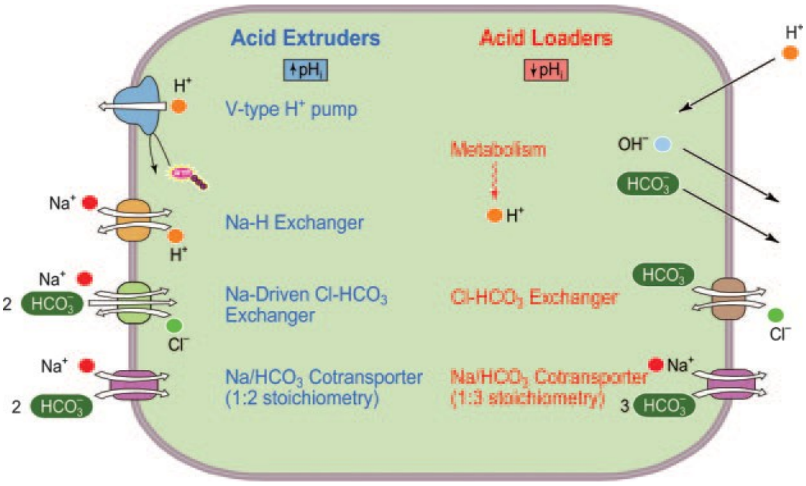

Figure 2.13: Schematic representation of acid extruders and acid loaders located in the cell membrane [126].

As shown on Fig 2.13, acid extruders are responsible for pumping out the protons from the cell and accumulating bicarbonate ions (HCO_3^-) inside the cell. This active transport uses energy either from adenosine triphosphate (ATP) hydrolysis or the sodium ion gradient. The opposite process is used by the acid loaders, which passively transport protons inside cells as well as pumping out OH^- and HCO_3^- to outside the cell.

The other factor facilitating this strict control over pH is the high buffering power, β, of the cytosol which is defined as the amount of strong base or strong acid that has to be added to a litre of solution to respectively raise or lower its pH by 1 pH unit. This is described by equation 2.16.

$$\beta = \frac{\Delta StrongBase}{\Delta pH} = -\frac{\Delta StrongAcid}{\Delta pH} \qquad (2.16)$$

This buffering power varies with pH. For closed systems, where total buffer concentration remains constant, the maximum buffering power is at a pH equal to the pKa value. In the cellular scenario, where CO_2 can easily penetrate from the extracellular milieu inside the cell, a crucial role is played by the open system category CO_2/HCO_3^- buffer pair, which contributes from a half to two thirds to the total buffering power. As for all open systems, this contribution increases exponentially with pH (Fig 2.14), which results in a large resistance of the cell to pH changes.

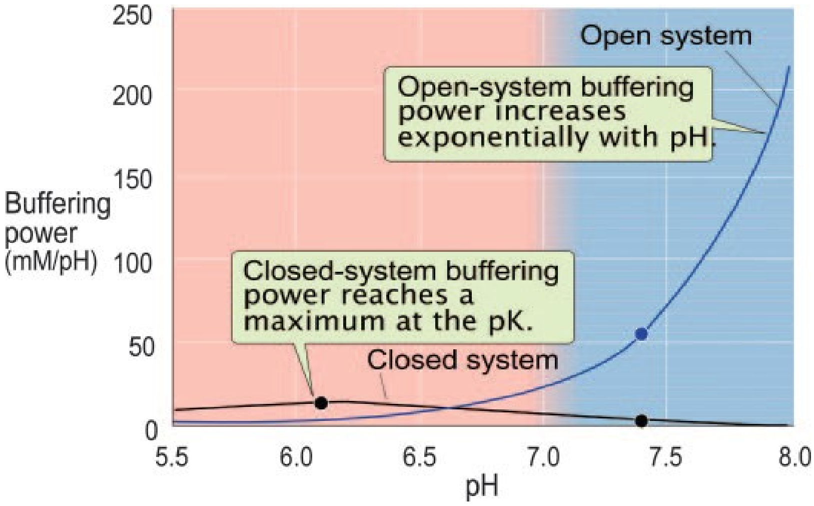

Figure 2.14: The pH dependence of buffering power in a closed and open-system [126].

By combining the ionic transport with the buffering power in a cell, a fundamental law of pH regulation can be formulated:

$$\frac{\Delta pH_i}{\Delta t} = \frac{J_E - J_L}{\beta} \qquad (2.17)$$

Where:

ΔpH_i - the rate of intracellular pH change

J_E - the rate of acid extrusion,

J_L - the rate of acid loading

From the above equation it is clear that intracellular pH will be stable only when the rate of proton extrusion and loading are the same. The cellular metabolism and changes in extracellular CO_2 concentration affect the intracellular and extracellular pH. Changes in pH on one side of the membrane induce changes in pH on the opposite side. In this way the intracellular and extracellular pH are strictly connected to each other and their changes will determine intracellular pH stability, which can be expressed in equation:

$$pH_i stability = \frac{\Delta pH_i}{\Delta pH_o} \tag{2.18}$$

where ΔpH_o describes the rate of pH change outside the cell. In normal physiological conditions, generally this ratio is around 30%, except for some pH - sensitive cells such as glomus cells of peripheral receptors [127] and certain neurons [128, 129], where its value can increase by a factor of two.

It has been suggested that the increased value of intracellular pH in cancerous cells may result in increased tolerance of the acidic environment present in a solid tumour [130, 131]. This shift to basic pH could play a role in the cellular signalling process. Therefore a better knowledge of proteomics is necessary in order to fully understand the mechanism of intracellular pH regulation.

2.8 Mechanism of nanoparticle cellular uptake

2.8.1 Introduction

In last 10 years, many different nanomaterials have been developed. Nanotechnology developments have had a large influence on both the industrial and pharmacological world. The development of polymeric micelles, quantum dots, liposomes and different types of nanoparticles for targeted drug delivery gave rise to a new era of nanomedicine [132,133]. In order to achieve the final goal, it has to be fully understood how the nanoparticles interact with the cells, how they penetrate through the cell membrane and which properties of nanomaterials are critical in this intracellular delivery process. In this section, a general overview of different nanoparticle uptake mechanisms is presented together with some examples of in vitro studies from the literature.

2.8.2 Endocytosis

Nanoparticles can enter the cell in a process called endocytosis. This process can be divided into two categories: phagocytosis and pinocytosis, which are briefly described in the following two separate sections. However, some common intracellular delivery stages for both of these categories can be distinguished and are illustrated in Figure 2.15. These stages are:

1. Engulfing of the nanoparticle in cell membrane invagination and formation of a membrane-bound vesicles, named endosomes or phagosomes depending on the uptake category.
2. Intracellular delivery of endosomes to specialised vesicular structures in order to direct the entrapped nanomaterial into diverse cellular compartments
3. Final delivery step which can undergo different scenarios such as:
    - ➢ Nanomaterial release into various intracellular structures
    - ➢ Transporting nano-cargo to the extracellular milieu.
    - ➢ Transferring nanoparticles between cells

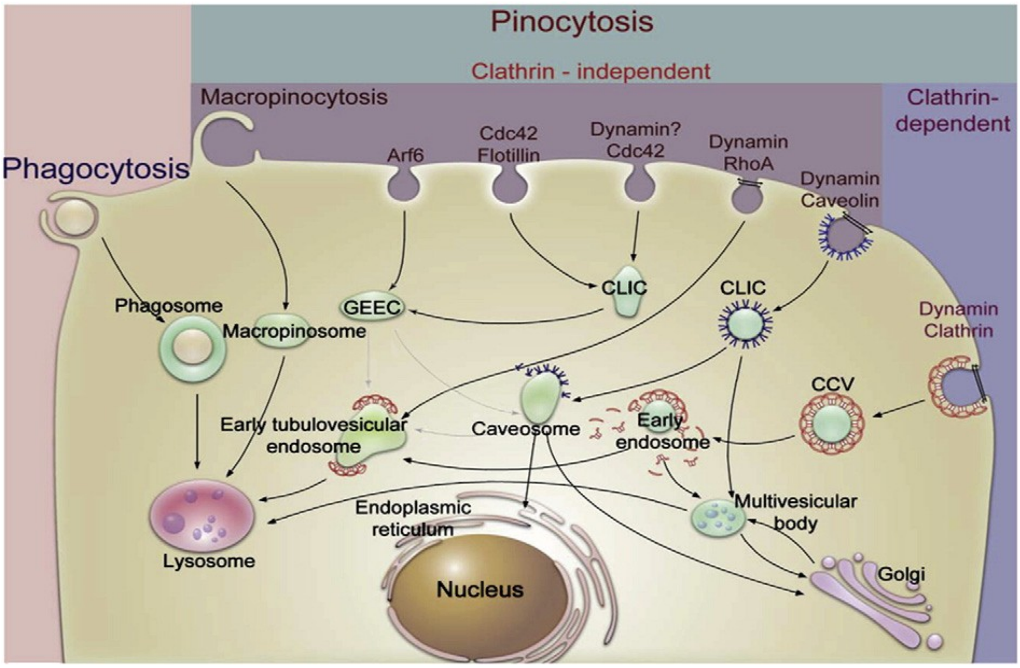

Figure 2.15: Schematic representation of different endocytotic pathways [134].

2.8.2.1 Phagocytosis

Phagocytosis is observed for macrophages, monocytes, neutrophils and dendritic cells. The particles, which are recognised in the bloodstream as phagocytic targets, are covered by proteins in a process called opsonization. These proteins are specific to the receptors located in the cell membrane of the phagocyte, which enables particle attachment to the cell surface. Then the particles are ingested by the phagosomes, which is followed by phagosome maturation, their fusion with lysosomes to the enzyme-rich structures called phagolysosomes, where the final step - degradation of the particles - occurs. It has been observed that the shape of the particle plays a much more important function than its size during phagocytotic uptake. Objects which are larger than the cell itself are able to be engulfed inside the phagosome. In the case of local particle shape, when the curvature of an object creates an angle larger than 45 degrees with the normal to the cell membrane at the point of initial contact, the phagocytosis process does not occur. This is due to the absence of actin structures which are crucial in the initial phase of the phagocytic mechanism.

2.8.2.2 Pinocytosis

This mechanism exists in all types of cells and its character varies between different cell types. The general classification is shown in Figure 2.16, where the main differentiation is based on the cytosolic protein called clathrin-1. The uptake mechanism where this protein participates in the creation of a coated pit is defined as clathrin-dependent or clathrin-mediated endocytosis (CME). All the other uptake events belong to the group of clathrin-independent processes, which are then divided into different subcategories determined by the membrane protein responsible for the uptake initialization.

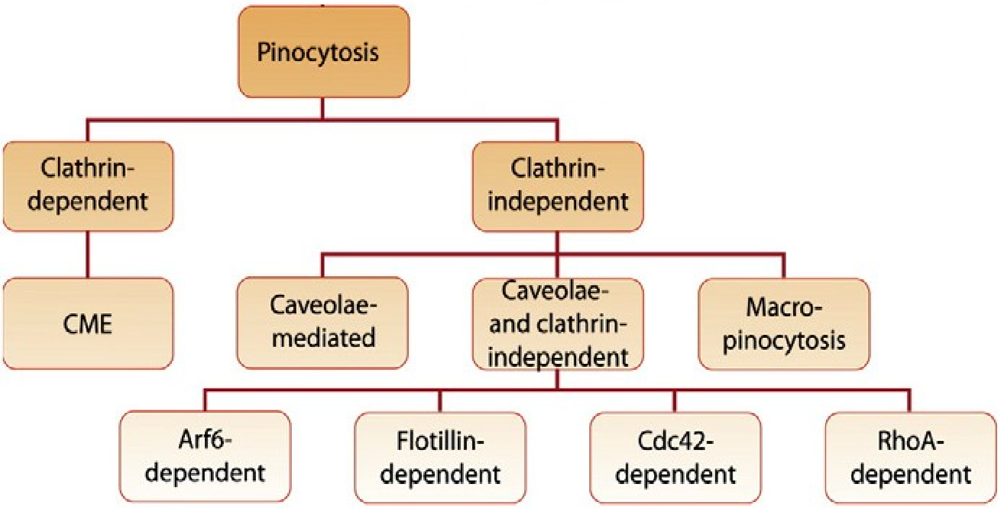

Figure 2.16: Classification of pinocytosis mechanisms [134].

An overview of all pinocytosis mechanism and their corresponding cellular functions are gathered in Table 2.2.

Table 2.2: Overview of pinocytosis processes.

Uptake category	Cell type	Mechanism	Function
Clathrin-dependent	All mammalian cells	Encapsulation of the cargo to a clathrin-1-coated pit, pinching off the vesicle from the plasma membrane by dynamin, shedding of the clathrin coat and vesicle fusion with the early endosomes, sorting of the cargo to the late endosomes/lysosomes, trans-Golgi network or to the recycling endosomes	Supplying nutrients (i.e. cholesterol, iron) Maintaining cellular homeostasis by inhibition of signalling pathways through internalization and degradation of receptors
Caveolae-mediated	Muscle, endothelial cells, fibroblasts and adipocytes	Attachment of cargo to caveolin-1 derived caveolae, formation of caveolae vesicles and their transport and fusion with caveosomes or multivescular body, delivery of the cargo to different cellular compartments	Cellular delivery of proteins and DNA Pathogens including bacteria and viruses entry pathway
Caveolae- and clathrin-independent	All cells except those with clathrin-dependent and caveolae-mediated pathways	Initiated by different endocytic proteins: Arf-6, flotillin, Cdc42 and RhoA. The intracellular transport not yet fully understood.	Transport of extracellular fluid, SV40, CTB, glycosylphosphatidylinositol (GPI)-linked proteins, interleukin-2, growth hormones crucial for cellular signalling pathways
Macropinocytosis	All cells except macrophages and brain microvessel endothelial cells	Activation of receptor tyrosine kinases by growth factors, which results in changes in the actin cytoskeleton, formation of membrane ruffles, which engulf the cargo and transport it to a large intracellular vacuole (0.5-10μm)– macropinosome	Transport of nutrients Entry route for bacteria, apoptotic bodies, necrotic cells and viruses

For nanomaterials, cellular uptake will be dependent on many different factors such as the particle charge, size, shape as well as material composition and surface chemistry. Examples from the literature show that positively charged nanomaterials use mainly clathrin-dependent and macropinocytosis routes whereas for negatively charged nanoparticles, caveolae-mediated endocytosis seems to be the most common way of entry to the cell [134]. Taking into consideration the size of the nano-cargo it has been noticed that, the smaller the size, the faster the uptake. Surprisingly, even particles as large as 5 μm may undergo pinocytosis [135]. In the case of even larger sizes, macropinocytosis could be considered. In order to target nanomaterial into specific tissue or cells, the immunological response and specificity have to be carefully considered. The approach used to date is to modify the surface of the nanomaterial with some “inert” polymer like e.g. PEG and to attach to such a coated structure receptor molecules i.e. antibodies, polypeptides, aptamers and others specific biomarkers which are specific to the cell membrane [136, 137, 138]. Nevertheless, a lot of research has to be done in order to fully control the nanoparticle uptake initially for in-vitro and eventually for in-vivo applications.

2.9 Summary

The theoretical aspects related to this interdisciplinary project have been presented. The advantages of silica nanoparticles for biological applications as well as the existing expertise in sol-gel derived optical chemical planar sensors, in the group, have been an inspiration for this nanosensing investigation. The performance of oxygen and pH-sensitive silica nanoparticles, described in the following experimental chapters, are comparable with the nanosensors presented here in the State-of-Art section. Most of the techniques used for nanoparticle characterization and the different biological protocols for nanosensors uptake have been summarized in materials and methods in the following two chapters. The last chapter is focused in the intracellular sensing studies.

References

[1] *"Jablonski diagram".* http://www.shsu.edu/~chm_tgc/chemilumdir/JABLONSKI.html.

[2] Herman, B. *Fluorescence Microscopy* BIOS Scientific Publishers, UK, 1998.

[3] Ramamoorthy, R.; Dutta, P. K.; Akbar, S. A. Oxygen sensors: Materials, methods, designs and applications *Journal of Materials Science*, **2003**, *38*, 4271–4282.

[4] Labasque,T.; Chaumery, C.; Aminot, A.; Kergoat, G. Spectrophotometric Winkler determination of dissolved oxygen: re-examination of critical factors and reliability, *Marine Chemistry*, **2004**, *88*, 53–60.

[5] Clark, L. C. Monitor and control of blood and tissue oxygen tensions. *Transactions American Society for Artificial Internal Organs*, **1956**, *2*, 41–57.

[6] Kautsky, H.; Hirsch, A. Quenching of luminescence by oxygen. *Transactions Faraday Society*, **1939**, *35*, 216–219.

[7] Shinar, R.; Zhou, Z. Q.; Choudhury, B.; Shinar, J. Structurally integrated organic light emitting device-based sensors for gas phase and dissolved oxygen. *AnalyticaChimica Acta*, **2006**, *568*, 190–199.

[8] Voraberger, H. S.; Kreimaier, H.; Biebernik, K.; Kern, W. Novel oxygen optrode withstanding autoclavation: technical solutions and performance. *Sensors and Actuators B-Chemical*, **2001**, *74*, 179–185.

[9] Brinker, C. J.; Scherer, G. W. Sol-Gel Science: *The Physics and Chemistry of Sol-Gel Processing*. Academic Press, Boston, 1990.

[10] Wolfbeis, O. S.; Marhold, H. A new group of fluorescent pH-indicators for an extended pH-range. *Fresenius Zeitschrift F¨ur Analytische Chemie*, **1987**, *327*, 347–350.

[11] Lin, J.; Liu, D. An optical pH sensor with a linear response over a broad range. *Analytica Chimica Acta*, **2000**, *408*, 49–55.

[12] Harper, G. B. Reusable glass-bound pH indicators. *Analytical Chemistry,* **1975**, *47*, 348–351.

[13] Peterson, J. I.; Goldstein, S. R.; Fitzgerald, R. V.; Buckhold, D. K. Fiber optic pH probe for physiological use. *Analytical Chemistry*, **1980**, *52*, 864–869.

[14] Hulth, S.; Aller, R. C.; Engstrom, P.; Selander, E. A pH plate fluorosensor (optode) for early diagenetic studies of marine sediments, *Limnology and Oceanography*, **2002**, *47*, 212–220.

[15] Liu, Z. H.; Liu, J. F.; Chen, T. L. Phenol red immobilized PVA membrane for an optical pH sensor with two determination ranges and long-term stability. *Sensors and Actuators B-Chemical*, **2005**, *107*, 311–316.

[16] Agayn, V. I.; Walt, D. R. Fiber-optic sensor for continuous monitoring of fermentation pH. *Bio-Technology*, **1993,** *11*, 726–729.

[17] Makote, R.; Collinson, M. M. Organically modified silicate films for stable pH sensors. *Analytica Chimica Acta*, **1999**, *394*, 195–200.

[18] Nivens, D. A.; Zhang, Y. K.; Angel, S. M. A fiber-optic pH sensor prepared using a base-catalyzed organo-silica sol-gel. *Analytica Chimica Acta*, **1998**, *376*, 235–245.

[19] Lakowicz, J. R.; Weber, G. Quenching of fluorescence by oxygen - probe for structural fluctuations in macromolecules. *Biochemistry*, **1973**, *12*, 4161– 4170.

[20] Watts, R. J.; Crosby, G. A. Spectroscopic characterization of complexes of ruthenium(II) and iridium(III) with 4,4'-diphenyl-2,2'-bipyridine and 4,7-diphenyl-1,10-phenanthroline. *Journal of the American Chemical Society*, **1971**, *93*, 3184–3188.

[21] Parmente, C. S.; Rau, J. D. Fluorescence quenching in aromatic hydrocarbons by oxygen. *Journal of Chemical Physics*, **1969**, *51*, 2242–2246.

[22] Lakowicz, J. R. *Principles of Fluorescence Spectroscopy, Chapter 8 and 9*. Springer-Verlag, New York, 3rd edition, 2006.

[23] Bacon, J. R.; Demas, J. N. Determination of oxygen concentrations by luminescence quenching of a polymer-immobilized transition-metal complex.

Analytical Chemistry, **1987**, *59*, 2780–2785.

[24] Carraway, E. R.; Demas, J. N.; DeGraff, B. A. Luminescence quenching mechanism for microheterogeneous systems. *Analytical Chemistry*, **1991**, *63*, 332– 336.

[25] Xu, W. Y.; McDonough, R. C.; Langsdorf, B.; Demas, J. N.; DeGraff, B. A. Oxygen sensors based on luminescence quenching - interactions of metal-complexes with the polymer supports. *Analytical Chemistry*, **1994**, *66*, 4133–4141.

[26] Demas, J. N.; DeGraff, B. A. Luminescence-based sensors – microheterogeneous and temperature effects. *Sensors and Actuators B-Chemical*, **1993**, *11*, 35–41.

[27] Edmonds, T. E.; Flatters, N. J.; Jones, C. F.; Miller, J. N. Determination of pH with acid-base indicators - implications for optical fiber probes. *Talanta*, **1988**, *35*, 103–107.

[28] Cox, M. E.; Dunn, B. Detection of oxygen by fluorescence quenching. *Applied Optics*, **1985**, *24*, 2114–2120.

[29] Wolfbeis, O. S.; Posch, H. E.; Kroneis, H. W. Fiber optical fluorosensor for determination of halothane and/or oxygen. *Analytical Chemistry*, **1985**, *57*, 2556–2561.

[30] Xu, W. Y.; Schmidt, R.; Whaley, M.; Demas, J. N.; DeGraff, B. A.; Karikari, E. K.; Farmer, B. L. Oxygen sensors based on luminescence quenching - interactions of pyrene with the polymer supports. *Analytical Chemistry*, **1995**, *67*, 3172– 3180.

[31] Mills, A. Optical oxygen sensors. *Platinum Met. Rev.* **1997**, *41*, 115-127.

[32] Klimant, I.; Wolfbeis, O.S. Oxygen-sensitive luminescent materials based on silicone-soluble ruthenium diimine complexes. *Anal. Chem.* **1995**, *67*, 3160-3166.

[33] Vanderkooi, J.M.; Maniara, G.; Green, T.J.; Wilson, D.F. An optical method for measurement of dioxygen concentration based upon quenching of phosphorescence. *J. Biol. Chem.* **1987**, *262*,5476-5482.

[34] Papkovsky, D.B. Luminescent porphyrins as probes for optical (Bio)sensors. *Sens. Actuat.B-Chem.* **1993**, *11*, 293-300.

[35] Lo, L.W.; Koch, C.J.; Wilson, D.F. Calibration of oxygen-dependent quenching of the phosphorescence of Pd-meso-tetra (4-carboxyphenyl) porphine: A phosphor with

general application for measuring oxygen concentration in biological systems. *Anal. Biochem.* **1996**, *236*,153-160.

[36] Apreleva, S.V.; Wilson, D.F.; Vinogradov, S.A. Tomographic imaging of oxygen by phosphorescence lifetime. *Appl. Opt.* **2006**, *45*, 8547-8559.

[37] Dunphy, I.; Vinogradov, S.A.; Wilson, D.F. Oxyphor R2 and G2: Phosphors for measuring oxygen by oxygen-dependent quenching of phosphorescence. *Anal. Biochem.* **2002**, *310*,191-198.

[38] Borisov, S. M.; Klimant, I. Luminescent nanobeads for optical sensing and imaging of dissolved oxygen. *Microchim. Acta* **2009***, 164*, 7-15.

[39] D. Wencel, Sol-gel-derived optical oxygen, pH and dissolved carbon dioxide sensors. Ph. D. Thesis, Dublin City University, 2008.

[40] Zhujun, Z.; Seitz, W. R. Optical sensor for oxygen based on immobilized hemoglobin. *Analytical Chemistry*, **1986**, *58*, 220–222.

[41] Chung, K. E.; Lan, E. H.; Davidson, M. S.; Dunn, B. S.; Valentine, J. S.; Zink, J. I. Measurement of dissolved oxygen in water using glass-encapsulated myoglobin. *Analytical Chemistry*, **1995**, *67*, 1505–1509.

[42] Mills, A. Oxygen indicators and intelligent inks for packaging food. *Chemical SocietyReviews*, **2005**, *34*, 1003–1011.

[43] Wang, E. J.; Chow, K. F.; Kwan, V.; Chin, T.; Wong, C.; Bocarsly, A. Fast and long term optical sensors for pH based on sol-gels. *Analytica Chimica Acta*, **2003**, *495*, 45–50.

[44] Ismail, F.; Malins, C.; Goddard, N. J. Alkali treatment of dye-doped sol-gel glass films for rapid optical pH sensing. *Analyst*, **2002**, *127*, 253–257.

[45] Kosch, U.; Klimant, I.; Wolfbeis, O. S. Long-lifetime based pH micro-optodes without oxygen interference. *Fresenius Journal of Analytical Chemistry*, **1999**, *364*, 48–53.

[46] Liu, J. N.; Shahriari, M. R., Sigel, G. H. Development of a porous polymer pH

optrode. *Optics Letters*, **1992**, *17*, 1815–1817.

[47] Liu, Z. H.; Luo, F. L.; Chen, T. L. Phenolphthalein immobilized membrane for an optical pH sensor. *Analytica Chimica Acta*, **2004**, *510*, 189–194.

[48] Lee, S. H.; Kumar, J.; Tripathy, S. K. Thin film optical sensors employing polyelectrolyte assembly. *Langmuir*, **2000**, *16*, 10482–10489.

[49] Cajlakovic, M.; Lobnik, A.; Werner, T. Stability of new optical pH sensing material based on cross-linked poly(vinyl alcohol) copolymer. *Analytica Chimica Acta*, **2002**, *455*, 207–213.

[50] Lobnik, A.; Oehme, I.; Murkovic, I.; Wolfbeis, O. S. pH optical sensors based on sol-gels: Chemical doping versus covalent immobilization. *Analytica Chimica Acta*, **1998**, *367*, 159–165.

[51] Aslan, K.; Lakowicz, J. R.; Szmacinski, H.; Geddes, C. D. Enhanced ratiometric pH sensing using SNAFL-2 on silver island films: Metal-enhanced fluorescence sensing. *Journal of Fluorescence*, **2005**, *15*, 37–40.

[52] Parker, J. W.; Laksin, O.; Yu, C. ; Lau, M. L.; Klima, S.; Fisher, R.; Scott, I.; Atwater, B. W. Fiber-optic sensors for pH and carbon dioxide using a self-referencing dye. *Analytical Chemistry*, **1993**, *65*, 2329–2334.

[53] Ismail, F.; Malins, C.; Goddard, N. Alkali treatment of dye-doped sol-gel glass films for rapid optical pH sensing. *Analyst* **2002***, 127*, 253-257.

[54] Lee, Y. K.; Smith, R.; Kopelman, R. Nanoparticle PEBBLE Sensors in Live Cells and In Vivo. *Annu. Rev. Anal. Chem.,* **2009**, *2*, 57-76.

[55] Buck, S. M.; Koo, Y. L.; Park, E.; Xu, H.; Philbert, M. A.; Brasuel, M. A.; Kopelman. R. Optochemical nananosensor PEBBLEs: photonic explorers for bioanalysis with biologically localized embedding. *Current Opinion in Chemical Biology,* **2004**, *8*, 540-546.

[56] Lee, Y. K.; Kopelman, R. Optical nanoparticle sensors for quantitative intracellular imaging. *Wiley interdiscipl. Rev. Nanomed. Nanobiotechnol.,* **2009**, *1*, 98-110.

[57] Jin, Y.; Lohstreter, S.; Pierce, D. T.; Parisien, J.; Wu, M.; Hall III, C.; Zhao, J. X. Silica Nanoparticles with Continuously Tunable Sizes: Synthesis and Size Effects on Cellular Contrast Imaging. *Chem. Mater.,* **2008**, *20*, 4411-4419.

[58] Song, C.; Ye, Z.; Wang, G.; Jin, D.; Yuan, J.; Guan, Y.; Piper, J. Preparation and time-gated luminescence bioimaging application of ruthenium complex covalently bound silica nanoparticles. *Talanta* **2009***, 79*, 103-108.

[59] Tallury, P.; Payton, K.; Santra, S. Silica-based multimodal/multifunctional nanoparticles for bioimaging and biosensing applications. *Nanomedicine*, **2008**, *3*, 579-592.

[60] Kandlikar, M.; Ramachandran, G.; Maynard, A.; Murdock, B.; Toscano, W. A. Health risk assessment for nanoparticles: A case for using expert judgment. *J. Nanopart. Res.* **2007***, 9*, 137-156.

[61] Fercher, A.; Borisov, S. M.; Zhdanov, A. V.; Klimant, I.; Papkovsky, D. B. Intracellular O_2 Sensing Probe Based on Cell-Penetrating Phosphorescent Nanoparticles. *ACS Nano* **2011***, 5*, 5499-5508.

[62] Xu, H.; Aylott, J. W.; Kopelman, R.; Miller, T. J.; Philbert, M. A. A real-time ratiometric method for the determination of molecular oxygen inside living cells using sol-gel-based spherical optical nanosensors with applications to rat C6 glioma. *Anal. Chem.* **2001***, 73*, 4124-4133.

[63] Koo, Y. E. L.; Cao, Y. F.; Kopelman, R.; Koo, S. M.; Brasuel, M.; Philbert, M. A. Real-time measurements of dissolved oxygen inside live cells by organically modified silicate fluorescent nanosensors. *Anal. Chem.* **2004***, 76*, 2498-2505.

[64] Cao, Y. F.; Koo, Y. E. L.; Kopelman, R. Poly(decyl methacrylate)-based fluorescent PEBBLE swarm nanosensors for measuring dissolved oxygen in biosamples. *Analyst* **2004***, 129*, 745-750.

[65] Guice, K. B.; Caldorera, M. E.; McShane, M. J. Nanoscale internally referenced oxygen sensors produced from self-assembled nanofilms on fluorescent nanoparticles. *J. Biomed. Opt.,* **2005**, *10*, 064031.

[66] Cheng, Z. L.; Aspinwall, C. A. Nanometre-sized molecular oxygen sensors prepared from polymer stabilized phospholipid vesicles. *Analyst,***2006***, 131*, 236–43.

[67] Borisov, S. M.; Klimant, I. Luminescent nanobeads for optical sensing and imaging of dissolved oxygen. *Microchim. Acta* **2009***, 164*, 7-15.

[68] Schmälzlin, E.; Van Dongen J. T.; Klimant, I.; Marmod´ee, B.; Steup, M. et al. An optical multifrequency phase-modulation method using microbeads for measuring intracellular oxygen concentrations in plants. *Biophys. J.,* **2005***, 89*, 1339–45.

[69] Schmälzlin, E.; Walz, B.; Klimant, I.; Schewe, B.; Löhmannsröben, H. G. Monitoring hormone-induced oxygen consumption in the salivary glands of the blowfly, *Calliphora vicina*, by use of luminescent microbeads. *Sens. Actuators B,* **2006***, 119*, 251–54.

[70] Dmitriev, R. I.; Ropiak, H. M.; Yashunsky, D. V.; Ponomarev, G. V.; Zhdanov, A. V.; Papkovsky, D. B. Bactenecin 7 Peptide Fragment as a Tool for Intracellular Delivery of a Phosphorescent Oxygen Sensor. *FEBS J.,* **2010**, *277*, 4651–4661.

[71] Dmitriev, R. I.; Zhdanov, A. V.; Ponomarev, G. V.; Yashunski, D. V.; Papkovsky, D. B. Intracellular Oxygen-Sensitive Phosphorescent Probes Based on Cell-Penetrating Peptides. *Anal. Biochem.*, **2010**, *398*, 24–33.

[72] Horvath, T.; Monson, E.; Sumner, J.; Xu, H.; Kopelman, R. Use of steady-state fluorescence anisotropy with PEBBLE nanosensors for chemical analysis. *Proc. SPIE (Int. Soc. Photonic Eng.),* **2002***, 4626*, 482–92.

[73] Clark, H.; Barker, S.; Brasuel, M.; Miller, M.; Monson, E.; Parus, S.; Shi, Z.; Song, A.; Thorsrud, B.; Kopelman, R.; Ade, A.; Meixner, W.; Athey, B.; Hoyer, M.; Hill, D.; Lightle, R.; Philbert, M. Subcellular optochemical nanobiosensors: probes encapsulated by biologically localised embedding (PEBBLEs). *Sens. Actuator B-Chem.,* **1998**, *51*, 12-16.

[74] Koo Lee, Y.-E.; Ulbrich, E. E.; Kim, G.; Hah, H.; Strollo, C.; Fan,W.; Gurjar, R.; Koo, S.; Kopelman, R. Near Infrared Luminescent Oxygen Nanosensors with Nanoparticle Matrix Tailored Sensitivity. *Anal. Chem.,* **2010**, *82*, 8446–8455.

[75] Wang, X.-d.; Gorris, H. H.; Stolwijk, J. A.; Meier, R. J.; Groegel, D. B. M.; Wegener, J.; Wolfbeis, O. S. Self-Referenced RGB Colour Imaging of Intracellular Oxygen. *Chem. Sci.,* **2011**, *2*, 901–906.

[76] Clark, H.; Kopelman, R.; Tjalkens, R.; Philbert, M. Optical nanosensors for chemical analysis inside single living cells. 2. Sensors for pH and calcium and the intracellular application of PEBBLE sensors. *Anal. Chem.,* **1999***, 71*, 4837-4843.

[77] Sun, H.; Scharff-Poulsen, A. M.; Gu, H.; Almdal, K. Synthesis and characterization of ratiometric, pH sensing nanoparticles with covalently attached fluorescent dyes. *Chemistry of Materials,* **2006***, 18*, 3381-3384.

[78] Ji, J.; Rosenzweig, N.; Griffin, C.; Rosenzweig, Z. Synthesis and application of submicrometer fluorescence sensing particles for lysosomal pH measurements in murine macrophages. *Anal. Chem.,* **2000***, 72*, 3497-3503.

[79] Ow, H.; Larson, D.; Srivastava, M.; Baird, B.; Webb, W.; Wiesner, U. Bright and stable core-shell fluorescent silica nanoparticles. *Nano Letters,* **2005***, 5*, 113-117.

[80] Gao, F.; Tang, L.; Dai, L.; Wang, L. A fluorescence ratiometric nano-pH sensor based on dual-fluorophore-doped silica nanoparticles. *Spectrochimica Acta Part A-Molecular and Biomolecular Spectroscopy,* **2007***, 67*, 517-521.

[81] Doussineau, T.; Smaihi, M.; Mohr, G. J. Two-Dye Core/Shell Zeolite Nanoparticles: A New Tool for Ratiometric pH Measurements. *Advanced Functional Materials,* **2009***, 19*, 117-122.

[82] Burns, A.; Ow, H.; Wiesner, U. Fluorescent core-shell silica nanoparticles: towards "Lab on a Particle" architectures for nanobiotechnology. *Chem. Soc. Rev.,* **2006***, 35*, 1028-1042.

[83] Chauhan, V. M.; Burnett, G. R.; Aylott, J. W. Dual-fluorophore ratiometric pH nanosensor with tuneable pKa and extended dynamic range. *Analyst,* **2011***, 136*, 1799-1801.

[84] Welser, K.; Perera, M. D. A.; Aylott, J. W.; Chan, W. C. A facile method to clickable sensing polymeric nanoparticles. *Chem. Commun.,* **2009**, 6601-6603.

[85] Nielsen, L. J.; Eyley, S.; Thielemans, W.; Aylott, J. W. Dual fluorescent labelling of cellulose nanocrystals for pH sensing. *Chem. Commun.,* **2010***, 46*, 8929-8931.

[86] Tomasulo, M.; Yildiz, I.; Raymo, F. pH-Sensitive quantum dots. *J Phys Chem B,* **2006***, 110*, 3853-3855.

[87] Jensen, R. A.; Sherin, J.; Emory, S. R. Single nanoparticle based optical pH probe. *Appl. Spectrosc.,* **2007***, 61,* 832-838.

[88] Wang, Z.; Bonoiu, A.; Samoc, M.; Cui, Y.; Prasad, P. N. Biological pH sensing based on surface enhanced Raman scattering through a 2-aminothiophenol-silver probe. *Biosens. Bioelectron.,* **2008***, 23,* 886-91.

[89] Kolbe, G. Das komplexchemische Verhalten der Kieselsäure", PhD Thesis, Friedrich-Schiller Universität Jena, 1956.

[90] Stöber, W.; Fink, A. Controlled Growth of Monodisperse Silica Spheres in the Micron Size Range. *Journal of Colloid and Interface Science*, **1968**, *26*, 62-69.

[91] Pileni, M. P. The role of soft colloidal templates in controlling the size and shape of inorganic nanocrystals. *Nature Materials*, **2003**, *2*, 145-150.

[92] Balthis, J. H.; Mendenhall, P. Preparation of sols from finely divided silicon. USP 2614994, 1952.

[93] Wang, X.; Shen, Z.; Sang, T.; Cheng, X.; Li, M.; Chen, L.; Wang, Z. Preparation of spherical silica particles by Stöber process with high concentration of tetra-ethyl-orthosilicate. *Journal of Colloid and Interface Science,* **2010**, *341*, 23-29.

[94] Matsoukas, T.; Gulari, E. Dynamics of growth of silica particles from ammonia-catalyzed hydrolysis of tetra-ethyl-silicate. *J. Colloid Interface Sci.,* **1988**, *124*, 252-261.

[95] Matsoukas, T.; Gulari, E. Monomer-addition growth with a slow initiation step: A growth model for silica particles from alkoxides. *J. Colloid Interface Sci.,* **1989**, *132*, 13-21.

[96] Bogush, G. H.; Zukoski IV, C. F. Studies of the kinetics of the precipitation of uniform silica particles through the hydrolysis and condensation of silicon alkoxides. *J.*

Colloid Interface Sci. **1991**, *142*, 1-18.

[97] Bogush, G. H.; Zukoski IV, C. F. Uniform silica particle precipitation: An aggregative growth model. *J. Colloid Interface Sci.,* **1991**, *142*, 19-34.

[98] Van Blaaderen, A.; Van Geest, J.; Vrij, A. Monodisperse colloidal silica spheres from tetraalkoxysilanes: Particle formation and growth mechanism. *J. Colloid Interface Sci.*, **1992**, *154*, 481-501.

[99] Chen, S. L.; Dong, P.; Yang, G. H.; Yang, J. J. Kinetics of formation of monodisperse colloidal silica particles through the hydrolysis and condensation of tetraethylorthosilicate. *Ind. Eng. Chem. Res.,* **1996**, *35*, 4487-4493.

[100] Collinson, M.M. Sol-gel strategies for the preparation of selective materials for chemical analysis. *Critical Reviews in Analytical Chemistry,* **1999**, *29*, 289-311.

[101] Knopp, D.; Tang, D.; Niessner, R. Review: Bioanalytical applications of biomolecule-functionalized nanometer-sized doped silica particles. *Analytica Chimica Acta,* **2009**, *647*, 14-30.

[102] Seddon, A. B. Sol-gel derived organic-inorganic hybrid materials for photonic applications. *IEE Proc.-Circuits Devices Syst.,* **1998**, *145*, 369-372.

[103] Tripathi, V. S.; Kandimalla, V. B.; Ju, H. Preparation of ormosil and its applications in the immobilizing biomolecules. *Sensors and Actuators B*, **2006**, *114*, 1071-1082.

[104] Sanchez, C.; Ribot, F. Design of hybrid inorganic-organic materials synthesized via sol-gel chemistry. *New J. Chem.,* **1994**, *18*, 1007-1047.

[105] Collinson, M. M. Recent trends in analytical applications of organically modified silicate materials. *Trends in Analytical Chemistry*, **2002**, *21*, 30-38.

[106] Qian, J.; Li, X.; Wei, M.; Gao, X.; Xu, Z.; He, S. Bio-molecule-conjugated fluorescent organically modified silica nanoparticles as optical probes for cancer cell imaging. *Opt. Express*, **2008**, *16*, 19568-19578.

[107] McDonagh, C.; Kolle, C.; McEvoy, A. K.; Dowling, D. L.; Cafolla, A. A.; Cullen,

S. J.; MacCraith, B. D. Phase fluorometric dissolved oxygen sensor. *Sensors and Actuators B*, **2001**, *74*, 124-130.

[108] Lakowicz, J. R. *Principles of Fluorescence Spectroscopy.* Kluwer Academic / Plenum Press, New York, 1999.

[109] Higgins, C.; Wencel, D.; Burke, C. S.; MacCraith, B. D.; McDonagh, C. Novel hybrid optical sensor materials for in-breath O_2 analysis. *Analyst,* **2008***, 133*, 241-247.

[110] Wencel, D.; Higgins, C.; Klukowska, A.; MacCraith, B. D.; McDonagh, C. Novel sol-gel derived films for luminescence-based oxygen and pH sensing. *Materials Science-Poland,* **2007***, 25*, 767-779.

[111] Goldman, R. D.; Spector, D. L. *Live Cell Imaging, A Laboratory Manual.* Cold Spring Harbor Laboratory Press, New York, 2005.

[112] Davidson, M.W.; Abramowitz, M. *Optical Microscopy.* Encyclopedia of Imaging Science and Technology, Wiley-Interscience, New York, 2002.

[113] Claxton, N. S.; Fellers, T. J.; Davidson, M. W. *Laser scanning confocal microscopy*, Department of Optical Microscopy and Digital Imaging, National High Magnetic Field Laboratory, The Florida State University, 2005, Unpublished (http://www.olympusfluoview.com/theory/LSCMIntro.pdf).

[114] López-Barneo, J.; Pardal, R.; Ortega-Sáenz, P. Cellular Mechanisms of Oxygen Sensing. *Annu. Rev. Physiol.,* **2001**, *63*, 259-287.

[115] Sharp, F. R.; Bernaudin, M. HIF1 and Oxygen Sensing in the Brain. *Nat. Rev. Neurosci.*, **2004**, *5*, 437-448.

[116] Bronstein, N. Ion Channels and Oxygen Sensing in the Cartoid Body. *Modulator*, **2008**, *22*, 18-22.

[117] Acker, H. Mechanisms and meaning of cellular oxygen sensing in the organism. *Respir. Physiol.*, **1994**, *95*, 1-10.

[118] Nattie, E.; Li, A. Central chemoreception 2005: A brief review. *Autonomic Neuroscience,* **2006**, *126-127*, 332-338.

[119] Zhu, H.; Bunn, H. F. Oxygen sensing and signalling: impact on the regulation of physiologically important genes. *Respir. Physiol.*, **1999**, *115*, 239-247.

[120] Semenza, G. L. Hypoxia-inducible factor 1: master regulator of O_2 homeostasis. *Current Opinion in Genetics & Development*, **1998**, *8*, 588-594.

[121] Wenger, R. H. Cellular adaptation to hypoxia: O_2-sensing protein hydroxylases, hypoxia-inducible transcription factors, and O_2-regulated gene expression. *FASEB J.,* **2002**, *16*, 1151-1162.

[122] Pugh, C. W.; Ratcliffe, P. J. Regulation of angiogenesis by hypoxia: role of the HIF system. *Nat. Med.*, **2003**, *9*, 677-684.

[123] Melillo, G.; Musso, T.; Sica, A.; Taylor, L. S.; Cox, G. W.; Varesio, L. A hypoxia-responsive element mediates a novel pathway of activation of the inducible nitric oxide synthase promoter. *J. Exp. Med.,* **1995**, *182*, 1683-1693.

[124] Lee, C.; Jiang, B.H.; Chin, B.Y.; Iyer, N.V.; Alam, J.; Semenza, G. L.; Choi, A. M. Hypoxia-inducible factor-1 mediates transcriptional activation of the heme oxygenase-1 gene in response to hypoxia *J. Biol. Chem.*, **1997**, *272*, 5375-5381.

[125] Metzen, E.; Ratcliffe, P. J. HIF hydroxylation and cellular oxygen sensing. *Biol. Chem.*, **2004**, *385*, 223-230.

[126] Boron, W. Regulation of intracellular pH. *Adv. Physiol. Educ.* **2004***, 28*, 160-179.

[127] Buckler, K. J.; Vaughan-Jones, R. D.; Peers, C.; Lagadic-Gossmann, D.; Nye, P. C. G. Effects of extracellular pH, pCO_2 and HCO_3^- on intracellular pH in isolated type-1 cells of the neonatal rat carotid body. *J Physiol.,***1991**, *444*, 703–721.

[128] Ritucci, N.A.; Chambers-Kersh, L.; Dean, J. B.; Putnam, R. W. Intracellular pH regulation in neurons from chemosensitive and nonchemosensitive areas of the medulla. *Am J Physiol Regul Integr Comp Physiol.,* **1998**, *275*, 1152–1163.

[129] Ritucci, N. A.; Dean, J. B.; Putnam, R.W. Intracellular pH response to hypercapnia in neurons from chemosensitive areas of the medulla. *Am J Physiol Regul Integr Comp Physiol.,* **1997**, *273*, 433–441.

[130] Gillies, R. J.; Martı´nez-Zaguila´n, R.; Peterson, E. P.; Perona, R. Role of intracellular pH in mammalian cell proliferation. *Cell Physiol Biochem.,,***1992**, *2*, 159–179.

[131] Stubbs, M.; McSheehy, P. M.; Griffiths, J. R.; Bashford, C. L. Causes and consequences of tumour acidity and implications for treatment. *Mol Med Today,* **2000**, *6*, 15–19.

[132] Kabanov, A. V.; Alakhov, V. Y. Pluronic (R) block copolymers in drug delivery: From micellar nanocontainers to biological response modifiers. *Critical Reviews in Therapeutic Drug Carrier Systems*, **2002**, *19*, 1–72.

[133] Duncan, R. The dawning era of polymer therapeutics. *Nature Review Drug Discovery,* **2003**, *2*, 347–360.

[134] Sahay, G.; Alakhova, D. Y.; Kabanov, A. V. Endocytosis of nanomedicines. *J. Controlled Release* **2010***, 145*, 182-195.

[135] Cannon, G.; Swanson, J. The macrophage capacity for phagocytosis. *Journal of Cell Science,* **1992**, *101*, 907–913.

[136] Farokhzad, O. C.; Langer, R. Nanomedicine: Developing smarter therapeutic and diagnostic modalities. *Advanced Drug Delivery Reviews*, **2006**, *58*, 1456–1459.

[137] Davis, M. E.; Chen, Z.; Shin, D. M. Nanoparticle therapeutics: an emerging treatment modality for cancer. *Nature Review Drug Discovery*, **2008**, *7*, 771–782.

[138] Esfand, R.; Tomalia, D. A. Poly(amidoamine) (PAMAM) dendrimers: from biomimicry to drug delivery and biomedical applications. *Drug Discovery Today*, **2001**, *6*, 427–436.

Chapter 3

Oxygen-sensitive silica nanoparticles

3.1 Introduction

In this chapter the development of novel oxygen-sensitive nanoparticles is described. The tuning of the nanosensor sensitivity to oxygen was successfully accomplished by the incorporation of an organically modified precursor into the silica matrix. Due to the poor solubility of PTMS-based nanoparticles in aqueous solution, observed by Kopelman [1], the nanosensors were prepared from a mixture of tetraethylorthosilicate (TEOS) and methyltriethoxysilane (MTEOS) to give a highly oxygen-permeable matrix. For dissolved oxygen detection, where the concentration of the oxygen molecules is lower than in the gas phase, a porous matrix, which is sufficiently hydrophobic, is essential for obtaining a sensitive sensor as the oxygen gas preferentially partitions out of the aqueous solution into the hydrophobic environment of the matrix. By combining two different silica precursors, composite nanoparticles for oxygen detection were synthesised. The ruthenium (II)-tris(4,7-diphenyl-1,10-phenanthroline)$^{2+}$ ($[Ru(dpp)_3]^{2+}$) complex, with a long lifetime of 5.3 μs and high luminescence quantum yield of ~ 30%, was employed as the oxygen-sensitive dye [1]. Thanks to the positive charge of the dye and its very low solubility in water, simple physical entrapment was used in the synthesis. Two different types of nanoparticles were developed during the project. Initially, a nanoparticle containing only the ($[Ru(dpp)_3]^{2+}$) complex was synthesised which was designed to be used for lifetime-based sensing. The second formulation involved the co-encapsulation of a nanosecond lifetime oxygen insensitive reference dye, ATTO488 N-hydroxy-succinimidyl-esters (ATTO488 NHS-ester) in addition to the ($[Ru(dpp)_3]^{2+}$) complex within the nanoparticle matrix to enable ratiometric detection. This approach, described in detail in section 2.5.2, is a good compromise between fluorophore concentration-dependent intensity-based measurements and lifetime-based detection, which is still not so common due to the requirement for relatively expensive electronics. This chapter reports the synthesis and characterisation of the particles which were designed with a size range and surface properties which are compatible with cellular uptake. A novel approach derived from a modified Stöber synthesis, described below, was used in order to achieve this goal. A gradual improvement in nanoparticle oxygen-sensitivity was achieved as the synthesis was modified from the initial, almost insensitive TEOS-based to the organically modified (so-called composite) nanoparticles with enhanced oxygen-permeability. Full investigations of both nanosensors, for lifetime- and ratiometric-based detection, including nanoparticle optical properties characterization as well as nanoparticle size and surface charge measurements, are described. The chapter concludes with the results from nanosensor oxygen calibration in water and a summary.

3.2 Materials and methods

3.2.1 Reagents and materials

Absolute ethanol (EtOH), 0.1 M hydrochloric acid (HCl), 28% (v/v) ammonium hydroxide solution (NH_4OH), anhydrous dimethyl sulfoxide (DMSO) and the silica precursors TEOS, MTEOS and aminopropyltriethoxysilane (APTES) as well as $[Ru(dpp)_3]Cl_2$ were purchased from Sigma Aldrich. ATTO488 NHS-ester was obtained from ATTO-TEC GmbH, Germany. Aqueous solutions of nanoparticles were prepared from deionised (DI) water.

3.2.2 Fabrication of O_2 nanosensors

Conventional Stöber-based nanoparticle synthesis:

This protocol was generally based on the classical Stöber method. Prior to the nanoparticle synthesis a stock solution of ([Ru(dpp)$_3$]$^{2+}$) was prepared by dissolving 0.02g of ([Ru(dpp)$_3$]$^{2+}$) in 10ml of EtOH. Then 26µl of this stock solution was mixed on the stirrer with 12.2ml of EtOH and 0.5ml of TEOS in a polystopper glass vial. After stirring for 15 minutes, 0.75ml of NH_4OH was added dropwise to the reaction mixture to initiate the formation of nanoparticles. After 30 minutes, a second silica precursor, MTEOS, in amount of 0.447ml was added and the final mixture was stirred for 24 hours at room temperature. The final molar ratio of silica precursors to dye was equal 100000. It was observed during the optimization process (presented in the experimental section) that the higher the amount of ([Ru(dpp)$_3$]$^{2+}$) that was used for the reaction the less spherical were the nanoparticles formed. This amount was determined to be sufficient for intracellular imaging and sensing. The nanoparticles were collected by centrifugation and resuspended in EtOH using ultrasonication, which was followed by three washing steps in EtOH. The nanosensors were centrifuged always with the same speed of 8320rcf and for an equal time of 30 minutes.

As a control, TEOS-based nanoparticles were synthesized according to the same protocol. To maintain the same molar ratios in the synthesis, the amount of TEOS was increased from 0.5ml to 1ml (added in one step, 15 minutes before pipetting NH_4OH). The nanoparticles were centrifuged and washed in EtOH as described in the paragraph above.

Novel modified Stöber – based nanoparticle synthesis for lifetime detection:

Based on the prior experience in the research group with sol-gel films, where hydrolysis of different organically modified precursors was carried out in an acidic environment, a new method of introducing this approach into the nanoparticle synthesis was developed. The nanoparticles were synthesized in two steps. At the start, 0.5ml of TEOS was added to 12.2ml of EtOH and all reagents were mixed on the stirrer in a polystopper glass vial for 15 minutes. The nanoparticle formation was then started by the dropwise addition of 0.75ml of NH_4OH to the reaction mixture. The second step of this modified Stöber synthesis was based on initiating the process of hydrolysis and condensation of MTEOS outside of the main reaction vial, which was done in the following way: 3.24ml of the same ([Ru(dpp)$_3$]$^{2+}$) stock solution prepared for the Stöber synthesis was mixed by stirring with 2.02ml of EtOH and 2.86ml of MTEOS in poly stopper glass vial for 15 minutes. Then 1.037ml of HCl was pipetted dropwise into the reaction mixture. The exothermic hydrolysis of MTEOS liberates heat, so that the temperature of the reaction mixture increased over a 15-minute period. After this time, 0.5ml of the mixture containing prehydrolysed MTEOS was added to the reaction vial. The time interval between initiating the reaction with TEOS and addition of the ethanol mixture with prehydrolysed MTEOS and ($[Ru(dpp)_3]^{2+}$) was optimized to 6 hours. For the shorter time intervals, the precipitate was observed in the reaction vial a few minutes after the addition of the MTEOS mixture. The reaction mixture was left on the stirrer for another 20 hours at room temperature. The nanoparticles were obtained by centrifugation at 8320rcf for 30 min and washed with EtOH (8320rcf, 30 min/3x).

Fabrication of nanoparticles for ratiometric detection

The novel modified Stöber approach was also employed for the synthesis of the nanoparticles for ratiometric detection. Here, an additional step was added to the protocol in order to introduce the oxygen-insensitive ATTO488NHS ester into the nanoparticle matrix, the chemical structure of which is presented in Figure 3.1.

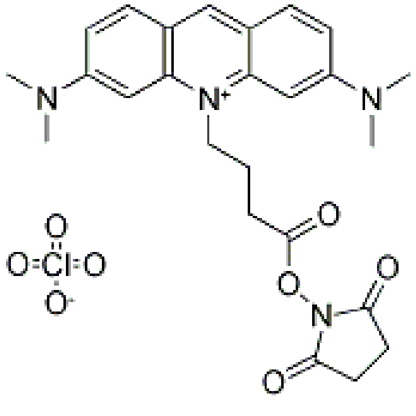

Figure 3.1: Chemical structure of ATTO488NHS ester.

The fluorophore was covalently attached to the silica matrix by reacting ATTO488NHS ester with APTES yielding the reactive ATTO488NHS ester-APTES conjugate prior to the nanoparticle synthesis. This NHS-ester derivative upon the reaction with APTES forms the amide bond, which then is used to immobilize ATTO488 within the nanoparticle core. A 2×10^{-3}M stock solution of 29.4µl of ATTO488NHS in DMSO and 0.5µl of APTES were added to 20.6µl of DMSO and stirred for 3 hours. The reaction mixture, due to its very small volume (50µl), was carried out in a 2ml eppendorf held in a poly stopper glass vial on the stirrer. The resulting ATTO488NHS ester-APTES conjugate was used without further purification.

The nanoparticle synthesis was initiated as described in detail in the previous section. Briefly, an ethanolic solution with TEOS was prepared on the stirrer; this was followed by the addition of NH_4OH. After 3 hours of the reaction, ATTO488NHS ester conjugate was added to the reaction. After another 3 h time interval, the mixture of prehydrolysed MTEOS was introduced to the reaction mixture and the nanoparticle forming mixture were left on the stirrer for another 20 hours at room temperature. The nanoparticles were collected by centrifuge (8320rcf, 30min) and three washing steps in EtOH were performed.

All samples were stored in the dark under ambient conditions.

3.2.3 Experimental characterisation systems

3.2.3.1 Phase fluorometry setup

The oxygen-sensitivity of the nanoparticles was measured using a phase fluorometry-based oxygen reader acquired from a partner company, DELTA, Denmark. The principle of phase fluorometry has already been described in section 2.5.3.1. Briefly, the reader consists of an optical fibre which directs light from a blue LED, corresponding to the absorption band of the ruthenium complex, into the sample and the emitted luminescence is directed back up the fibre, and, using appropriate filtering, is detected using a photodiode detector. To generate the different mixtures of calibration gases in a controlled way, two mass flow controllers (Celerity, Ireland) and the control unit (National Instruments, Ireland) were employed. For operating the mass flow controller system and collecting and displaying experimental data, the data acquisition and control software was developed, using LabVIEW™.

An aqueous solution of nanoparticles placed in a 50 ml plastic centrifuge tube (VWR, Ireland) was mounted in a clamp and attached to a holder. To create an air-tight chamber, the tube was closed with a silicone stopper (Fisher Scientific, Ireland). The flow of the calibration gases, which was controlled by mass flow controllers (Celerity, Ireland) and the control unit (National Instruments, Ireland), was bubbled using plastic tubing (Tygon, USA) and a needle punched directly through the stopper into the sample. Another needle was used as an outlet to release the pressure created while the sample was degassing. Each sample, containing nanoparticles re-suspended in water (7mg/ml), was bubbled with different oxygen and nitrogen mixtures for 5 minutes. The first step (0% O_2, 100% N_2) was set for 10 minutes to allow complete removal of oxygen from the nanoparticle solution. The excitation light from a 450nm blue LED, which was modulated at a frequency of 20 kHz, was delivered through an optical fiber, as described above, which was attached to the bottom of the sample. The modulation frequency f_{opt} was optimized for the luminophore lifetime τ, according to the Equation 3.1.

$$2\pi f_{opt}\tau = 1 \tag{3.1}$$

The emitted light was collected by the same optical fiber and transported back to the oxygen reader for the analysis. A red emission filter was used to isolate the emission from ($[Ru(dpp)_3]^{2+}$)-doped nanoparticles. The measurement was done every 3 seconds. Photodiode was used for the detection.

3.2.3.2 Dynamic Light Scattering (DLS)

The size and zeta potential of the nanoparticles were determined using a Delta^{TM}NanoC Particle Analyzer (Beckman Coulter, USA) equipped with a two 30mW 658nm laser diodes as a light source, designed for separate size and zeta potential measurements. The samples, in aqueous solution, were transferred to a disposable plastic cuvette and flow cell for size and zeta potential measurements, respectively. The signal was collected by a photomultiplier tube and then was fed to a digital autocorrelator for the nanoparticle size and zeta potential calculation. The Polydispersity index was measured from the size distribution of the nanoparticle population. Each value reported was an average of five measurements.

3.2.3.3 Transmission Electron Microscopy (TEM)

Transmission electron microscopy was performed by Ms Tiina Toivonen at University College Dublin using a Tecnai G2 20 Twin microscope (FEI, USA). One drop (around 10µl) of the diluted sample in EtOH (concentration ~ 1 mg/ml) was dried on a 300mesh copper grid with formvar / carbon film obtained from Agar Scientific, UK. The samples were then stored for analysis.

3.2.3.4 Spectrofluorometry

The luminescence emission spectra of the nanoparticles were acquired using a FluoroMax-2 spectrofluorometer (Horiba Jobin Yvon, USA) equipped with a continuous wave 150 W xenon lamp as a light source. The nanoparticles were dispersed in DI water in a quartz cuvette for standard excitation and emission spectra measurements. The excitation spectra were obtained for 520nm and/or 610nm emission wavelength, which corresponds to ATTO488 and ($[Ru(dpp)_3]^{2+}$) emission peaks, respectively. The emission spectra were collected for 450nm wavelength excitation.

For the oxygen calibration of the nanoparticles, designed for the ratiometric detection, a 1.8 ml quartz flow cell with 10 mm path length obtained from Starna Scientific Limited, UK was used. Before each measurement, samples were transferred into a 50ml plastic centrifuge tube with a silicone stopper and degassed using the mass flow controller setup described in section 3.2.3.1. Then each sample was transferred with a flow rate 15mms^{-1} to a flow cell using a Minipuls-3 peristaltic pump (Gilson, France) and the plastic tubing (Tygon, USA) for the measurements. The samples were excited at 450nm wavelength. The emitted light was forwarded through the monochromator to the photomultiplier detector.

The spectrofluorometer was employed to monitor the luminescence of the nanoparticles undergoing the leaching experiment (described in section 3.2.3.5).

All the measurements were carried out for equally diluted (10x) nanoparticle stocks. The slits on the excitation and emission monochromators were set to 3nm.

3.2.3.5 Leaching studies

2.5ml of the aqueous solution of the nanoparticles co-encapsulated with a water-soluble ATTO488 and water-insoluble ($[Ru(dpp)_3]^{2+}$) were transferred into the FLOAT-A-LYSER G2 dialysis device (Spectra/Por®, USA) with a re-sealable screw cap, a weighted bottom and a flotation ring (shown in Figure 3.2).

Figure 3.2: FLOAT-A-LYSER G2 dialysis device.

Prior to usage, the dialysis membrane was washed three times in deionized water according to the manufacturer's instructions. The device was then placed inside a 1L glass beaker filled with deionized water and left on the stirrer for 24 hours. As recommended, within this time the deionized water in the beaker was exchanged for fresh water twice (after 4 and 8 hours of dialysis). The sample was transferred from the dialysis device to a quartz cuvette for the luminescence measurements every few hours and the emission spectra of the nanoparticles were recorded as described in the previous section.

3.3 Development of O_2 - sensitive nanoparticles

3.3.1 Introduction

There are several conditions which have to be fulfilled by the nanoparticles in order to use them for intracellular sensing studies. The nanoparticles have to be small enough to be non-toxic and passively transported through the cellular membrane. It has been shown as well that the charge on the nanoparticle surface plays a very important role in the uptake mechanism [2]. The results vary considerably between different nanomaterials, cell lines and even research groups. It seems, however, that nanoparticles in the size range between 20 and 50 nm and with a positive charge on their surface are easily engulfed by the cells [3]. In this intracellular sensing approach some additional features have to be taken into consideration, such as hydrophobicity and porosity of the nanoparticles which are important for the nanosensor oxygen response. On the other hand, as mentioned already, the nanoparticles have to be dispersable in the aqueous cellular environment, therefore a certain hydrophobic – hydrophilic balance has to be established in order to satisfy both of these criteria. The nanoparticle optimization process is described below.

3.3.2 Optimization of nanoparticle size and shape

The properties of nanoparticles synthesised by the Stöber method are dependent on many parameters including the nature and concentration of the catalyst, the silicon alkoxide precursors type, as well as water-to-silane ratio, pH, temperature and humidity [4]. Changes in one or more parameters have an impact on the relative rate of hydrolysis and condensation (described in section 2.4.4), which then influences the shape, size, porosity and hydrophobicity of the final nanoconstructs. Due to the previous experience of the group with ($[Ru(dpp)_3]^{2+}$)-doped sol-gel materials, the same dye was chosen for the detection of intracellular oxygen. Taking into account the good solubility of ($[Ru(dpp)_3]^{2+}$) in EtOH, the Stöber nanoparticle synthesis seemed to be the best approach. The alternative techniques for the silica nanoparticle synthesis, such as well-established microemulsion [5] and less common lysine-catalysed emulsion [6] had to be excluded from the investigation, because of their aqueous reaction environment. In the course of the project, many different (~100) formulations were used in order to optimise the nanoparticles for maximum oxygen response while retaining other desirable morphological properties such as size and monodispersity. A summary of approaches used is described in Table 3.1.

Table 3.1: Summary of results obtained from the optimization of Stöber nanoparticle synthesis. For simplicity, an alphabetical nomenclature was introduced to the table. P – precursor, C- catalyst, D – dye, S- solvent, 2"x"- twice amount of moles of "x", PDI – polydispersity index.

PRECURSORS	**CATALYST**	**DYE**	**SOLVENT**	**SIZE [nm]**	**PDI**
P	C	D	S	~230	0.095
P	C	2D	S	Precipitate	
P	2C	D	S	~480	0.195
P	C	D	½ S	Precipitate	
½ P	C	D	S	~160	0.047
2P	C	D	S	~100	0.04
5P	C	D	S	~80	0.089
P	5C	D	S	Precipitate	

As can be seen from the data presented in Table 3.1, with an increase in amount of the catalyst (NH_4OH) the size of the nanoparticles increased (from 230nm to 480nm). When a certain level of the catalyst was exceeded, nanoparticles did not form. In the case of the silica precursor, when the amount was decreased (½ P) or increased (2P, 5P), the size of the nanoparticles measured on DLS was always smaller than for the initial recipe. The PDI index, which indicates the degree of the sample monodispersity (PDI should be ≤ 0.2 for a stable colloidal suspension of nanoparticles [7]), in most cases was less than 0.1. The amount of solvent and dye played as well a crucial role in the formation of the nanoparticles. When their initial values were changed (2D, ½ S), nanoparticles were not formed. To gain better insight into the nanoparticle formation, the TEM technique was also used in these studies. The results obtained from TEM imaging are presented in Figure 3.3.

R=100000	R=50000
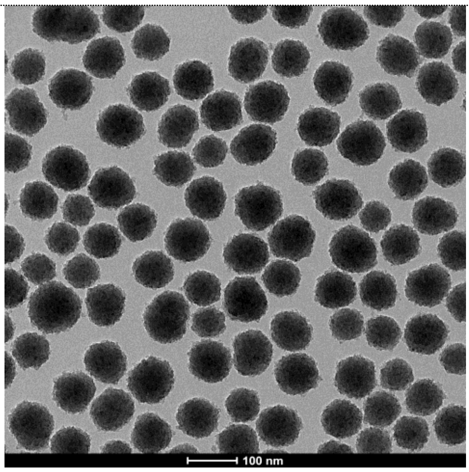 	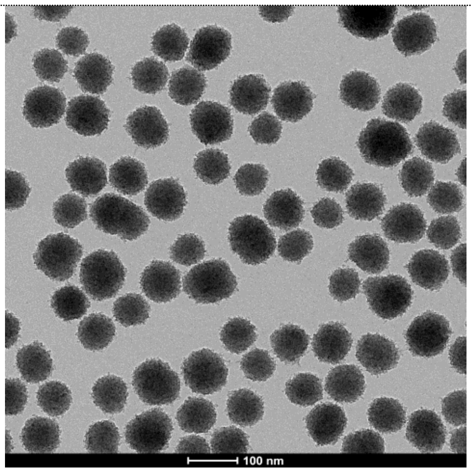
R=20000	R=10000
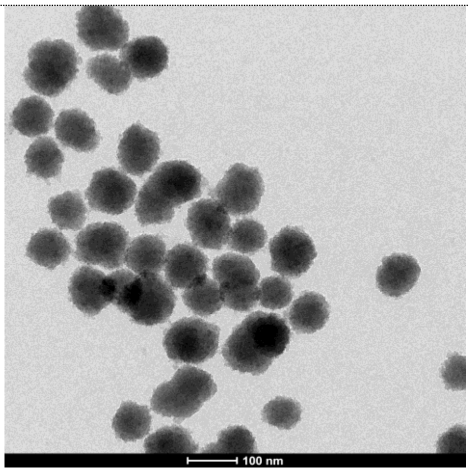 	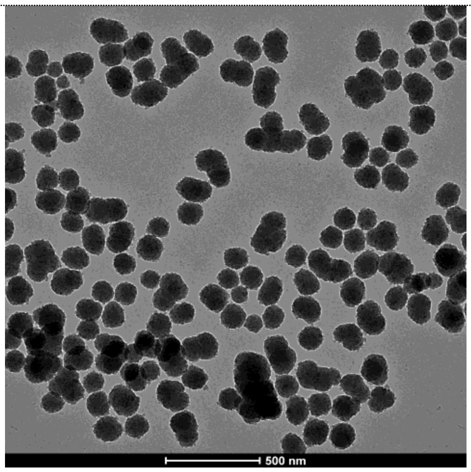
Temperature of reaction: 50°C	Reaction without stirring
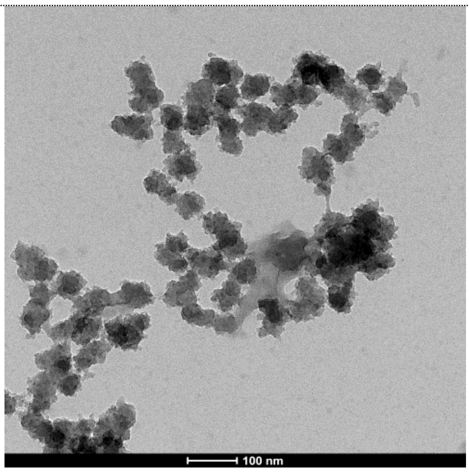 	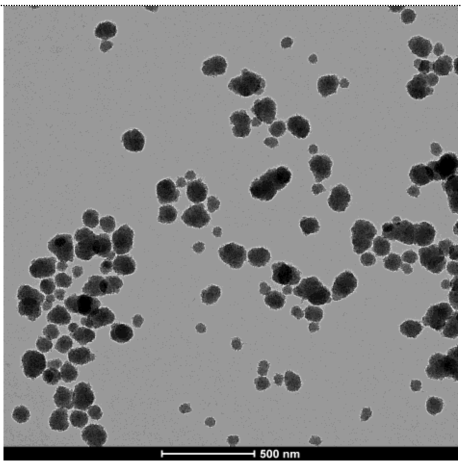

Figure 3.3: TEM images of the nanoparticles synthesized during the optimization process. R – molar ratio of silica precursor to dye.

The TEM images contributed some valuable information to the whole optimization process. It was found that factors such as higher temperature of the reaction (50^{o}C), elimination of stirring during the nanoparticle synthesis (sample mixed only within first 30 minutes) and increase in amount of dye (from R=100000 to R=10000), which was observed to act as a catalyst have a negative impact on the formation of the nanoparticles. Despite the many parameters which severely influence the final reaction product, a successful protocol for the synthesis of the composite nanoparticles was established (described in section 3.2.2).

3.3.3 Optimization of nanoparticle oxygen response

3.3.3.1 Optical properties of ($[Ru(dpp)_3]^{2+}$)-doped nanoparticles

To fulfil all the optical nanosensor criteria, the oxygen-sensitivity of the nanoparticles had to be optimized on the phase fluorometry setup, the principles of which are described in section 2.5.3.1. Prior to this step, the optical properties of the nanoparticles were characterized on the spectrofluorometer. The excitation and emission spectra of ($[Ru(dpp)_3]^{2+}$)-doped nanoparticles dispersed in water were compared to the spectra of the free dye dissolved in EtOH. The spectroscopic results from this analysis are presented in Figure 3.4.

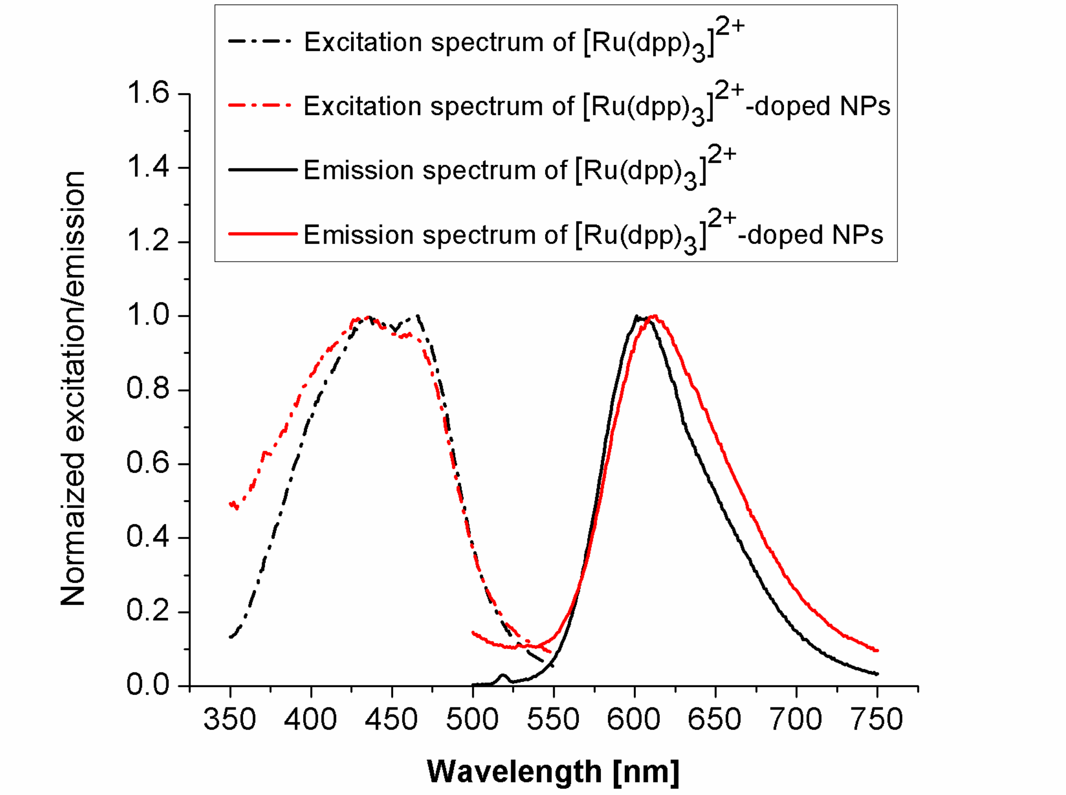

Figure 3.4: Normalized excitation and emission spectra of ($[Ru(dpp)_3]^{2+}$) (λ_{exc}=450nm, λ_{em}=610nm) dissolved in EtOH and ($[Ru(dpp)_3]^{2+}$)-doped nanoparticles dispersed in DI water.

As can be observed in Figure 3.4, the emission spectrum of ($[Ru(dpp)_3]^{2+}$)-doped nanoparticles with the emission peak at 610nm were slightly shifted toward the longer wavelengths (~10nm) with respect to the free ($[Ru(dpp)_3]^{2+}$) dye emission peak. This can be explained by the difference in ($[Ru(dpp)_3]^{2+}$) microenvironments (EtOH versus a composite nanoparticle in water), which has been shown to influence the optical properties of the fluorophore [8]. As well as the other favourable features of good photostability, long μs lifetime and high quantum yield which were mentioned in section 2.3.4, the large Stokes shift of ($[Ru(dpp)_3]^{2+}$) allows for a relatively simple experimental set up for sensing. All of the optical properties of ($[Ru(dpp)_3]^{2+}$) discussed above support the choice of this dye for these intracellular oxygen studies.

3.3.3.2 Oxygen-sensitivity performance of ($[Ru(dpp)_3]^{2+}$)-doped nanoparticles synthesized by the classical Stöber method

Having characterized the optical properties of the ($[Ru(dpp)_3]^{2+}$)-doped nanoparticles, oxygen-sensitivity tests were performed using the phase fluorometry setup described in section 3.2.3.1. In the standard experimental procedure, in parallel with oxygen response scans, all samples were investigated for their size and the surface charge (defined as a zeta potential) using DLS and TEM techniques. The cumulative data from all the techniques mentioned above, are presented and discussed below. As the starting point, TEOS-based nanoparticles doped with ($[Ru(dpp)_3]^{2+}$) were synthesized according to the Stöber protocol described in section 3.2.2 and characterized. As observed before in the literature, the dense hydrophilic silica matrix formed as a result of hydrolysis and condensation of TEOS has a low level of permeability to oxygen [10]. Therefore the results obtained for TEOS-based nanoparticles were used as a control in the development of the composite nanoparticles with enhanced oxygen-sensitivity. In the next step, the composite nanoparticles were synthesized based on the same protocol. The results from these comparative studies are presented in Figure 3.5.

<table>
<tr><th colspan="2">Stöber method</th></tr>
<tr><th>TEOS-based nanoparticles</th><th>Composite nanoparticles</th></tr>
<tr><td colspan="2">a) DLS data</td></tr>
<tr><td>Hydrodynamic diameter :
96.3 nm ±15.5nm
PDI = 0.045
Zeta potential = -49.6 mV</td><td>Hydrodynamic diameter:
101.2 nm ± 16.6 nm
PDI = 0.033
Zeta potential = -46.8 mV</td></tr>
<tr><td colspan="2">b) TEM (scale bar: 50nm)</td></tr>
<tr><td>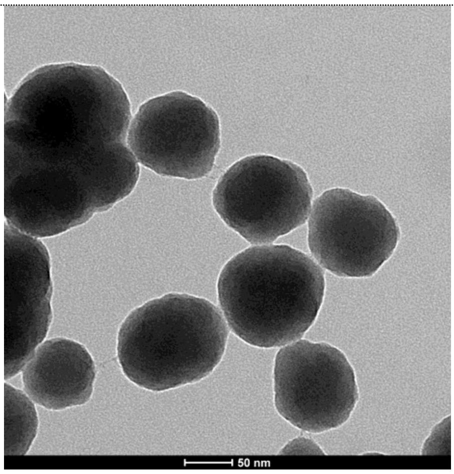 </td><td>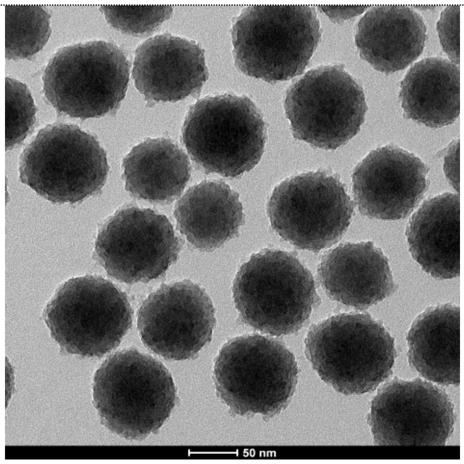 </td></tr>
<tr><td colspan="2">c) Phase angle response</td></tr>
<tr><td>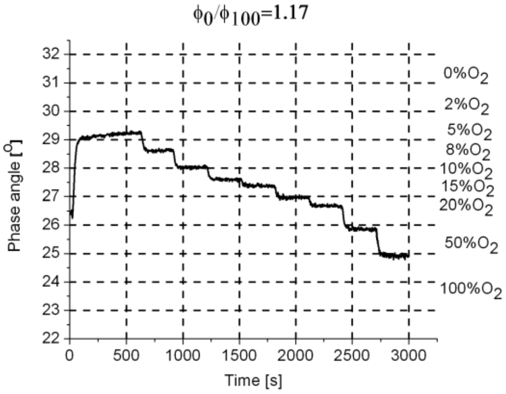 </td><td>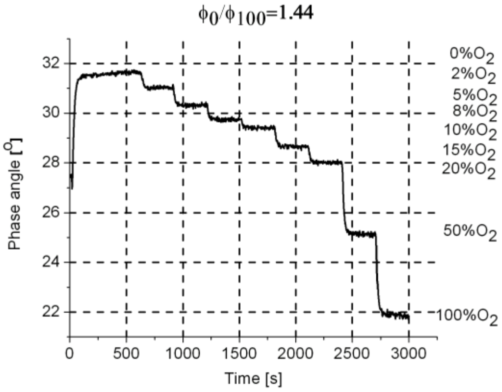 </td></tr>
</table>

d) Calibration curve – full oxygen concentration range

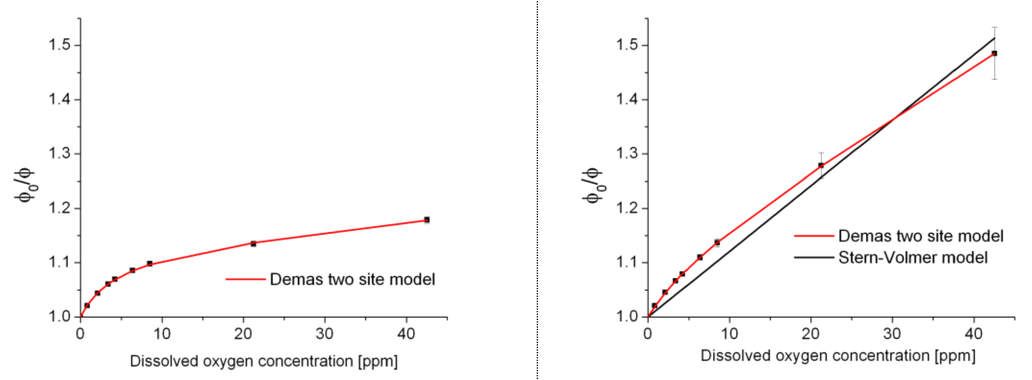

e) Calibration curve – physiological oxygen concentration range

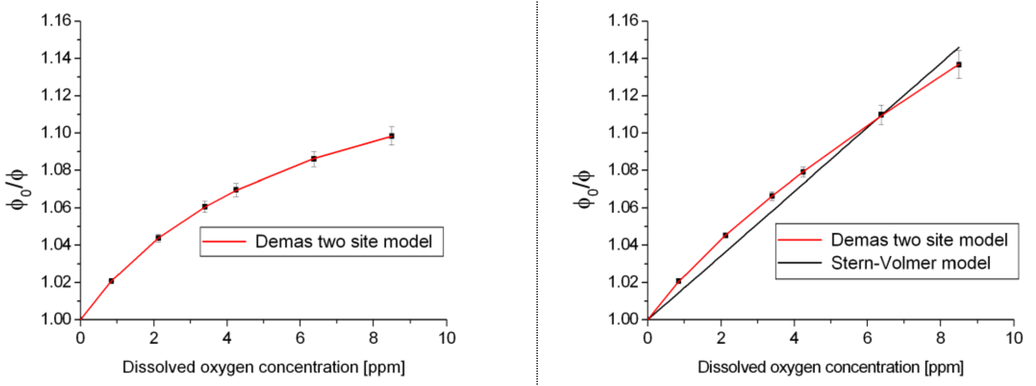

Figure 3.5: The results obtained for TEOS-based and composite nanoparticles doped with ($[Ru(dpp)_3]^{2+}$) prepared according to the Stöber method: a) size and zeta potential measurements, b) TEM imaging, c) phase angle response, d) calibration curve in the full dissolved oxygen concentration range, e) calibration curve in the physiological dissolved oxygen concentration range.

DLS analysis of TEOS-based and the composite nanoparticles revealed homogenous nanoparticle populations with an average hydrodynamic diameter of 96.3 nm and 101.2 nm, respectively. Very good monodispersity of the nanoparticles in solution is manifest in the low PDI value (<0.1). Depending on the charge on the surface of the nanoparticle, which is influencing on the zeta potential value, the measured sample in liquid can aggregate (-30mV< zeta potential <+30mV) or remain stable (-30mV >zeta potential> +30mV) The excellent stability of the nanoparticles in water was confirmed by the high zeta potential values equal to – 49.6 mV and – 46.8 mV, respectively. The size of the nanoparticles measured from TEM images is smaller than that measured by DLS, due to the difference between the hydrodynamic diameter of nanoparticles in solutions and the more precise TEM measurements of the dry nanoparticle cores [9]. TEM images confirmed the lack of nanoparticle aggregates within the sample. The structure of TEOS-based nanoparticles was observed to be more regular compared to that of the composite nanoparticles. Within the synthesis optimization it was noticed that increasing the amount of MTEOS (up to the molar ratio: TEOS:MTEOS=1:4) results in a rougher, less regular nanoparticle surface, which was thought to indirectly prove the presence of the symmetric, non-hydrolysed methyl group coming from MTEOS. Based on the new findings, this hypothesis was modified in time and it will be further discussed in section 3.3.3.3.

With regard to the oxygen-sensitivity of the nanoparticles, as can be observed from the data, (see Figure 3.5c) the phase angle decreases as the amount of oxygen in the gas mixture blown through the sample increases, what is related to a decrease in the lifetime of ($[Ru(dpp)_3]^{2+}$), caused by the oxygen quenching effect (described in section 2.3.3). As expected, a larger oxygen response ($\Phi_0/\Phi = 1.44$, where Φ_0/Φ is used as a measure of maximum oxygen sensitivity) than for TEOS-based nanoparticles is detected for the composite one, whose increased sensitivity is observed at very low (0 – 5%) and very high (50-100%) O_2 concentration in the gas mixture. Outside this range of concentration (5-50%) the sensitivity of both nanosensors remains the same. The dissolved oxygen concentrations, expressed in ppm, were then calculated based on the solubility constant of oxygen in water at 21°C (0.004252g of O_2 in 100g of H_2O) [10]. The calibration plots (Φ_0/Φ versus $[O_2]$) were drawn and fitted to a linear Stern-Volmer and non-linear Demas two-site models (Equation 2.3 and Equation 2.6 in section 2.3.3) within full and physiological dissolved oxygen concentration range, which is shown in Figure 3.5 d, e. The Demas model gave an excellent correlation (r^2=0.999) over the full as well as physiological oxygen concentration range for the composite nanoparticles (see data in Table 3.2). From the error assigned to K_{SV2} parameter, it is visible that Demas model is not relevant to the TEOS-based nanoparticles. The very short linear range for TEOS-based nanoparticles is associated with their very limited permeability to oxygen caused by their dense silica network ($\Phi_0/\Phi = 1.17$). Due to this limited sensitivity, the data for these nanoparticles could not be fitted to the Stern-Volmer model. The poor fitting to this linear model (r^2=0.978) was observed as well for the composite nanoparticles (r^2=0.978). The calibration is based on the performance of three samples. The error bars associated with the nanoparticle solutions are very small. This illustrates very good reproducibility of the nanoparticle synthesis.

Table 3.2: Stern-Volmer and Demas fitting parameters for pure TEOS-based and composite nanoparticles prepared by the Stöber method. Terms from Equation 2.6, r^2 = regression.

NPs	**Stern-Volmer model - full oxygen concentration range**			
	$K_{SV}[O_2]^{-1}$	r^2		
Composite	0.0121 ± 0.0005	0.972		
NPs	**Stern-Volmer model - physiological concentration range**			
	$K_{SV}[O_2]^{-1}$	r^2		
Composite	0.0172 ± 0.0006	0.978		
	Demas model – full oxygen concentration range			
	f_1	$K_{SV1}[O_2]^{-1}$	$K_{SV2}[O_2]^{-1}$	r^2
TEOS	0.11 ± 0.01	0.2574 ± 0.0186	0.0013 ± 0.0044	0.999
Composite	0.11 ± 0.01	0.1541 ± 0.0105	0.0083 ± 0.0001	0.999
	Demas model – physiological concentration range			
	f_1	$K_{SV1}[O_2]^{-1}$	$K_{SV2}[O_2]^{-1}$	r^2
TEOS	0.14 ± 0.01	0.1968 ± 0.0077	0.0001 ± 0.0003	0.999
Composite	0.06 ± 0.01	0.2741 ± 0.0408	0.0105 ± 0.0006	0.999

Based on the data from Table 3.2, the most readily quenched site, K_{SV1}, of the composite nanoparticles is around 1.5 times higher than that of TEOS-based one at physiological oxygen concentration range. The two different microenvironments within the nanoparticle structure are described by f_1 and f_2 parameter values. The recovered values for f_1 for both TEOS-based and composite nanoparticles, are very small (0.14±0.01 and 0.06±0.01 respectively). It indicates that only 14% and 6% of ($[Ru(dpp)_3]^{2+}$) molecules that are immobilized within the nanoparticle structures are located within the oxygen-permeable microenvironments with higher oxygen permeability (K_{SV1}> K_{SV2}). Taking into account the above findings and comparing the maximum oxygen sensitivity obtained for the composite nanoparticles (Φ_0/Φ = 1.44) to the literature ($\Phi_0/\Phi = 2.7$) [10], further steps to improve the nanosensor oxygen response were taken.

3.3.3.3 Development of ($[Ru(dpp)_3]^{2+}$)-doped nanoparticles with enhanced oxygen-sensitivity

As discussed before in the introduction, it was established from work on thin film oxygen sensors, that a hydrophobic matrix optimises the oxygen response [11]. An increase in the amount of the methyl group within the nanoparticle structure should result therefore in a better oxygen response. The new modified Stöber approach, described in section 3.2.2, was used to synthesize composite nanoparticles with enhanced sensitivity. The hydrolysis and condensation of MTEOS, before adding to the reaction mixture, was initiated in the acidic environment. The amount of MTEOS and the time of addition were optimised. The full characterization of the nanoparticles is presented in Figure 3.6.

Modified Stöber method
Composite nanoparticles
a) DLS data
Hydrodynamic diameter 90.6 nm ± 17.8 nm **PDI** = 0.048 **Zeta potential** = -43.7 mV
b) TEM imaging (scale bar: 50nm) 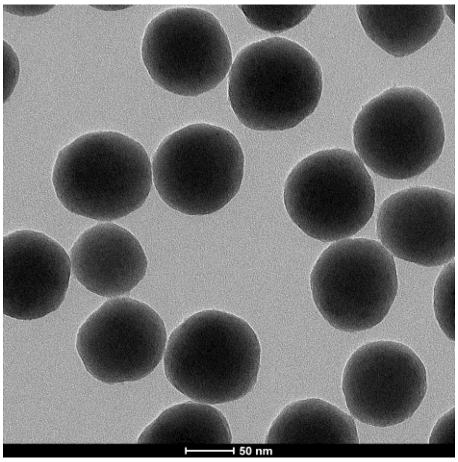

c) Phase angle response

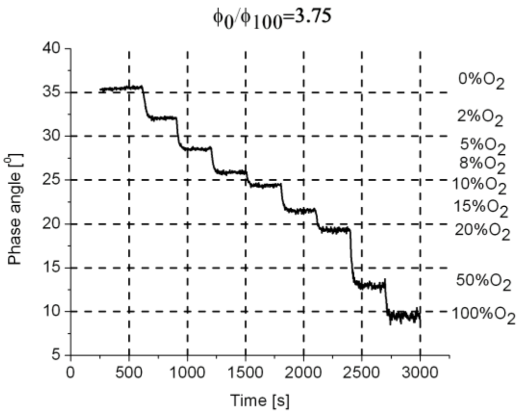

d) Calibration curve – full oxygen concentration range

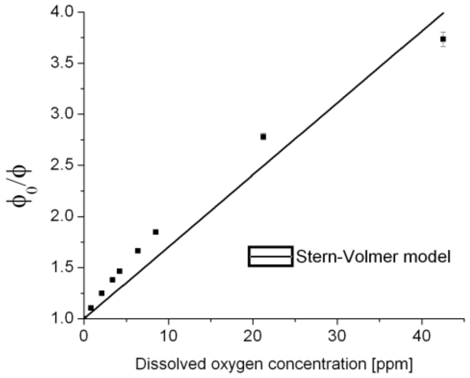

e) Calibration curve – physiological oxygen concentration range

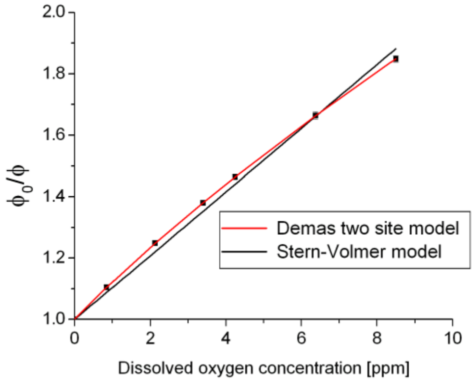

Figure 3.6: The results obtained for the composite nanoparticles doped with ($[Ru(dpp)_3]^{2+}$) prepared according to the new modified Stöber method: a) size and zeta potential measurements, b) TEM imaging, c) phase angle oxygen response, d) calibration curve within full dissolved oxygen concentration range, e) calibration curve within physiological dissolved oxygen concentration range.

The nanoparticles synthesised by this new modified Stöber approach have a hydrodynamic diameter equal to 90.6 nm ± 17.8 nm and low PDI value equal to 0.048. These results, together with a high zeta potential value (described in section 3.3.3.2), indicate the excellent stability of the composite nanoparticles in water. TEM imaging reveals the smaller size of the nanoparticles, as discussed earlier, by drying the nanoparticle solution on the TEM grids. Moreover, the shape of the nanoparticles observed on the TEM image is spherical, which is in contrast to the previous findings for the composite nanoparticles prepared via the classical Stöber method. It was postulated in the previous section for the composite nanoparticles prepared via a conventional Stöber method that as the amount of MTEOS used for the reaction increases, a greater degree of hydrophobicity is introduced into the nanoparticle. This was thought to increase the roughness of the nanoparticle surface. Based on the TEM images obtained for the nanoparticles synthesized via the modified Stöber synthesis, this hypothesis has to be revised. This huge contrast in the nanoparticle shape fabricated by these two different approaches (classical and new modified Stöber synthesis), may be caused by the different MTEOS hydrolysis environment. In the case of the previous approach based on the classical Stöber method, the introduction of MTEOS to the reaction environment with high pH seems not to facilitate the incorporation of this precursor to the nanoparticles. As a possible consequence, only a small fraction of MTEOS used for the reaction may contribute to the formation of the composite nanoparticles.

A significant enhancement in the oxygen-sensitivity ($\Phi_0/\Phi = 3.75$) was observed for the composite nanoparticles synthesized via new modified Stöber technique within the full dissolved oxygen concentration range (0ppm-42.5ppm). In the dissolved oxygen concentration range from 0 to 10ppm, the Demas model gave an excellent correlation with the data ($r^2 = 0.999$) (see data in Table 3.3), that indicates the presence of two independent luminophore micro-domains with different accessibilities. However, in this intracellular sensing application, where the concentration of dissolved oxygen is very small (7.4ppm under ambient condition), a good correlation to the Stern-Volmer model is observed ($r^2 = 0.994$), which simplifies the process of the nanosensor calibration to a Stern-Volmer-derived linear calibration plot. The fitting was performed as well for the data points obtained from the full oxygen concentration range. It was not possible to fit the data to the Demas model (possibly another model suitable for fitting the data from three or more micro-domains required). Further inspection of the data from Table 3.3 reveals that even if the Ksv_1 value (0.20) obtained for these new nanoparticles is lower than the one obtained for the composite nanoparticles obtained via the conventional Stöber method (0.27), a much larger fraction of ($[Ru(dpp)_3]^{2+}$) molecules is located in the microenvironment permeable to the oxygen for the newly synthesised nanoparticles (f_1 =0.54) The recovered value for f_1 for the nanoparticles synthesised by Stöber method without prehydrolysis of MTEOS is 0.06±0.01 (see data in Table 3.2), which combined with a more efficient quenching effect mentioned above, could suggest that this small fraction of ($[Ru(dpp)_3]^{2+}$) molecules exposed to the oxygen are located on the surface of the nanoparticles.

Table 3.3: Stern-Volmer and Demas fitting parameters for the composite nanoparticles doped with ($[Ru(dpp)_3]^{2+}$) prepared by the new modified Stöber method.
Terms from Equation 2.6: r^2 = regression.

Stern-Volmer model – full oxygen concentration range			
$K_{SV}[O_2]^{-1}$	r^2		
0.0704 ± 0.004	0.951		
Stern-Volmer model – physiological oxygen concentration range			
$K_{SV}[O_2]^{-1}$	r^2		
0.1037 ± 0.0019	0.994		
Demas model – physiological oxygen concentration range			
f_1	$K_{SV1}[O_2]^{-1}$	$K_{SV2}[O_2]^{-1}$	r^2
0.54 ± 0.05	0.2014 ± 0.0133	0.0403 ± 0.0055	0.999

3.3.3.4 Development of composite nanoparticles for ratiometric detection

Taking into consideration the complexity of the electronics and the relatively high cost of the equipment required for lifetime-based imaging, composite nanoparticles suitable for the standard fluorescence microscopy instrumentation were developed in parallel. A second fluorophore, ATTO488, acting as a reference dye, was co-encapsulated with ($[Ru(dpp)_3]^{2+}$) in the nanoparticle matrix in order to perform the dual emission-based ratiometric measurements, described in section 2.5.2. Due to the wide absorption spectrum of the ruthenium dye complex, it was possible to excite both dyes with the same excitation wavelength of 488nm. The ratio of luminescence intensities emitted at 520nm for the reference dye and 610nm for oxygen-sensitive complex was calculated for different concentration of oxygen, which was then utilized in the microscopy imaging studies. The synthesis was based on the protocol described in detail in the nanosensor fabrication section. Prior to the oxygen-sensitivity measurements, the optical properties of these nanoparticles were analysed on the spectrofluorometer and the optical spectra obtained from these measurements are presented in Figure 3.7.

a) ATTO488 spectra ($\lambda_{exc\ max} = 500nm$, $\lambda_{em\ max} = 525nm$)

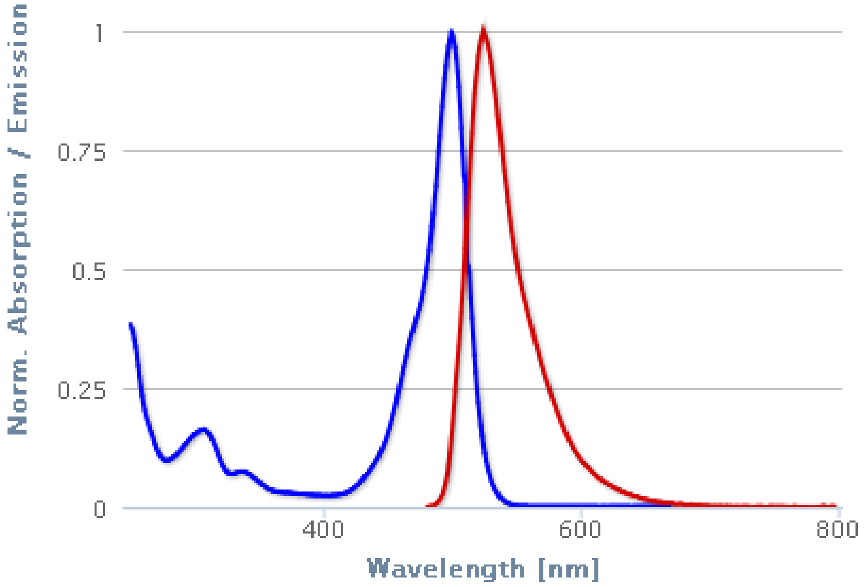

b) ($[Ru(dpp)_3]^{2+}$)/ATTO488 – doped nanoparticle (NP) and free ruthenium spectra

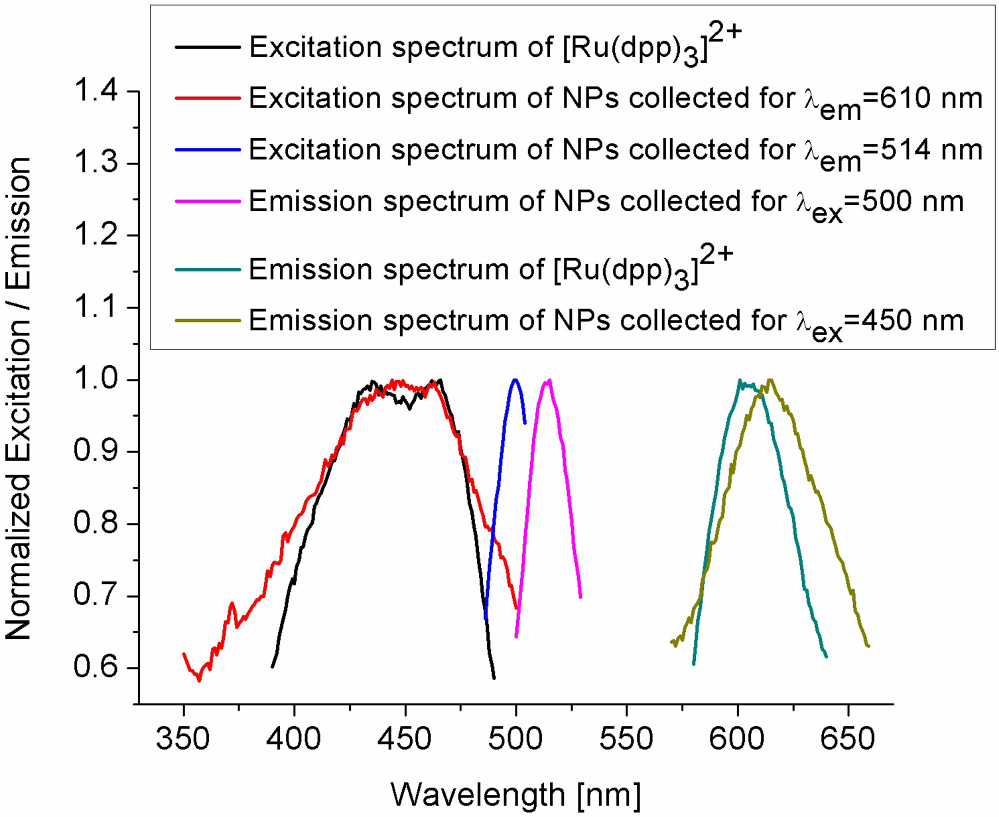

Figure 3.7: a) Normalized absorption and emission spectra of ATTO488 (λ_{exc}=488nm) dissolved in water [12], b) Normalized excitation and emission spectra of ($[Ru(dpp)_3]^{2+}$)/ATTO488 – doped nanoparticle in water. The spectra of a free ($[Ru(dpp)_3]^{2+}$) dissolved in EtOH presented in section 3.3.3.1 was added to the graph.

As shown in Figure 3.7b, the excitation peaks of the spectra collected for ($[Ru(dpp)_3]^{2+}$)/ATTO488 – doped nanoparticles and free fluorophores overlap very well. In the case of the emission spectra, a small shift toward a longer wavelengths is observed for the ($[Ru(dpp)_3]^{2+}$)/ATTO488 – doped nanoparticles with respect to the free dye molecules, which was already mentioned before and attributed to the difference in the microenvironment of ($[Ru(dpp)_3]^{2+}$) (see section 3.3.3.1).

($[Ru(dpp)_3]^{2+}$)/ATTO488 - doped composite nanoparticles were then investigated for their size, zeta potential and oxygen sensitivity and the results from this analysis are presented in Figure 3.8.

Modified Stöber method

Composite nanoparticles for the ratiometric detection

a) DLS analysis

Hydrodynamic diameter = 87.3 nm ± 15.2 nm

PDI = 0.067

Zeta potential = - 46.22 mV

b) TEM imaging (scale bar: 50nm)

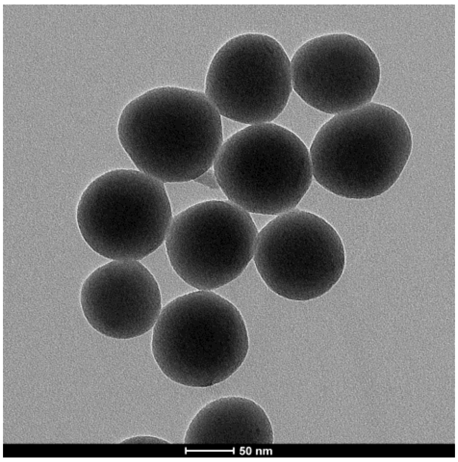

c) Spectrofluorometry

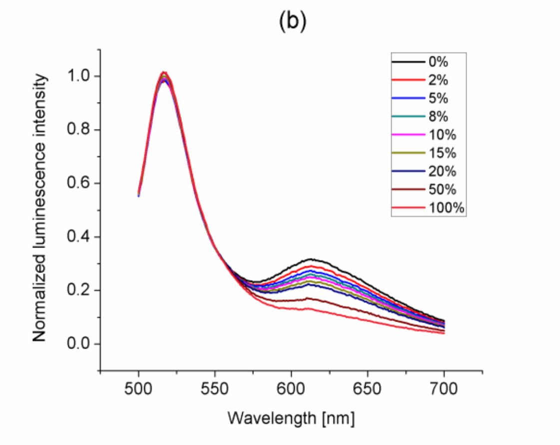

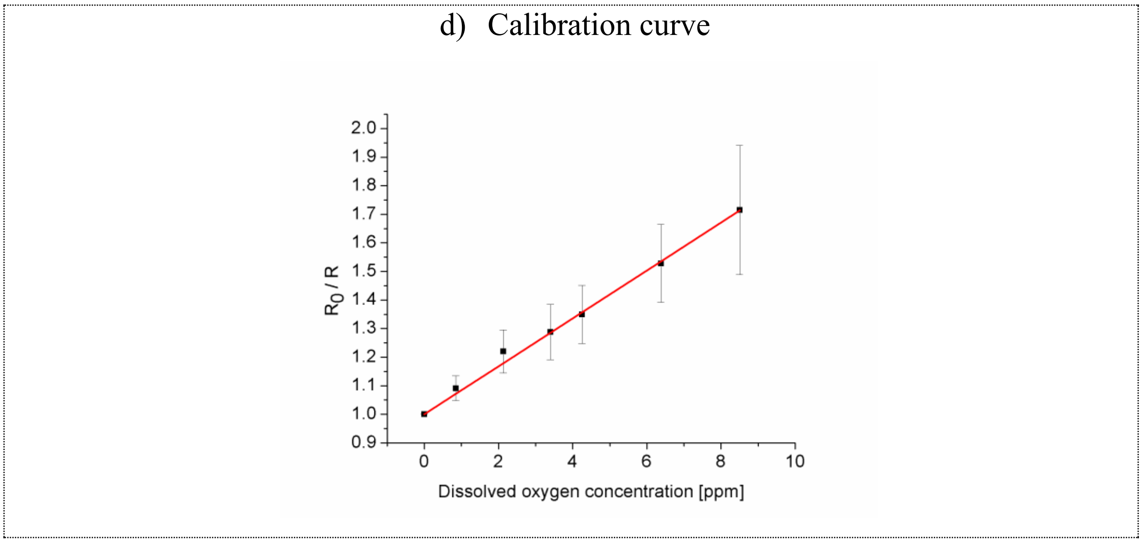
d) Calibration curve

Figure 3.8: The results obtained for the composite nanoparticles doped with ($[Ru(dpp)_3]^{2+}$) and ATTO488 prepared according to the new modified Stöber method: a) size and zeta potential measurements, b) TEM imaging, c) oxygen-sensitivity spectrofluorometric analysis, d)calibration curve within physiological dissolved oxygen concentration range. R_0 is the ratio between the fluorescence intensities of ATTO488 and ($[Ru(dpp)_3]^{2+}$) in the absence of oxygen, and R is the ratio at a given oxygen concentration.

As expected, based on the previous results obtained for the ($[Ru(dpp)_3]^{2+}$)-doped nanoparticles (see section 3.3.3.2), the hydrodynamic diameter of the nanoparticles co-encapsulated with ($[Ru(dpp)_3]^{2+}$) and ATTO488 equal to 87.3 nm ± 15.2 nm is slightly bigger than the nanoparticle size measured by TEM (~60nm). A homogeneous, monodispersed population of nanoparticles is presented on the TEM image, which is also well confirmed by DLS (PDI<0.1). The good stability of the nanoparticles in water is confirmed by the high zeta potential value measured on DLS (discussed in the previous section). The quasi-linearity ($r^2 = 0.994$) of the Stern-Volmer plot suggests a single microenvironment for the fluorophore exposed to the oxygen [10]. Very large error bars were obtained for this calibration experiment, which possibly derives from the imperfect experimental calibration setup (described in section 3.2.3.4). The oxygen-sensitivity of the ($[Ru(dpp)_3]^{2+}$)/ATTO488-doped nanoparticles is smaller (~1.3 times) than for nanoparticles containing only the ($[Ru(dpp)_3]^{2+}$) complex (based on K_{SV1} values for data obtained within the physiological concentration range in Table 3.3 and Table 3.4). It is possible that the small amount of APTES, present in the reaction mixture, acts as a catalyst, which results in a more dense silica network.

Table 3.4: Stern-Volmer fitting parameters for the composite nanoparticles doped with ($[Ru(dpp)_3]^{2+}$) and ATTO488NHS ester prepared by the new modified Stöber method.
Terms from Equation 2.6: r^2 – regression.

NPs doped with	**Stern-Volmer model**	
	$K_{SV}[O_2]^{-1}$	r^2
($[Ru(dpp)_3]^{2+}$) / ATTO488	0.0843 ± 0.0016	0.994

Due to very good solubility of ATTO488 in water, the leaching studies were performed for the nanoparticles according to the protocol described in section 3.2.3.5. The results from this experiment are presented in Figure 3.9.

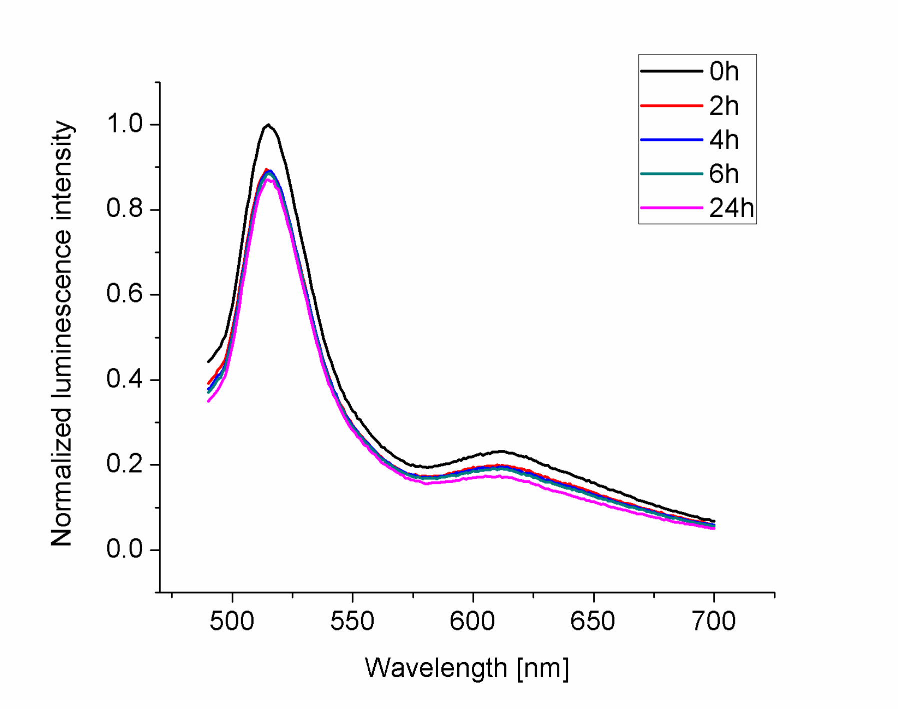

Figure 3.9: The data collected from the leaching experiment done for the nanoparticles co-encapsulated with ($[Ru(dpp)_3]^{2+}$) and ATTO488.

There is a small drop (~10%) in the luminescence intensity of both fluorophores observed within the first 2 hours. After this, no leaching is detected. This experiment indirectly proves the successful covalent immobilization of highly-water soluble ATTO488 within the nanoparticle structure.

3.3.4 Temporal stability

The stability of the composite nanoparticles with enhanced oxygen-sensitivity was monitored over time. Due to the problem with repeatability of the measurements done with a flow cell and peristaltic pump on the spectrofluorimeter (note a huge error bar on Figure 3.8 d,) the stability studies were done only for ($[Ru(dpp)_3]^{2+}$)-doped composite nanoparticles using the phase fluorometry setup. The oxygen response curves were measured in 7 day intervals (up to 4 weeks since transferring the nanoparticles into the water). The results from this temporal stability study are presented in Figure 3.10.

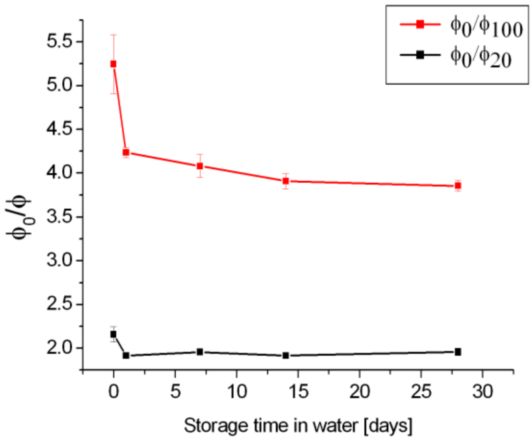

Figure 3.10: Effect of storage time in water on oxygen nanosensor sensitivity.

From these data, it can be seen that a decrease in oxygen-sensitivity was observed within the first 24 hours, which is possibly caused by an on-going precursor hydrolysis process occurring within the nanoparticle matrix when stored in the aqueous environment. For the samples kept in ethanol, no change in nanosensor sensitivity was observed, which confirmed the above hypothesis. All data shown, including calibration plots presented in the previous sections, were carried out for the stable samples only.

3.3.5. Reversibility studies

Reversibility studies were performed on the phase fluorometry setup (described in section 3.2.3.1) for the best performing sample - ($[Ru(dpp)_3]^{2+}$)-doped composite nanoparticles prepared by modified Stöber method. The results from phase angle response are presented in Figure 3.11.

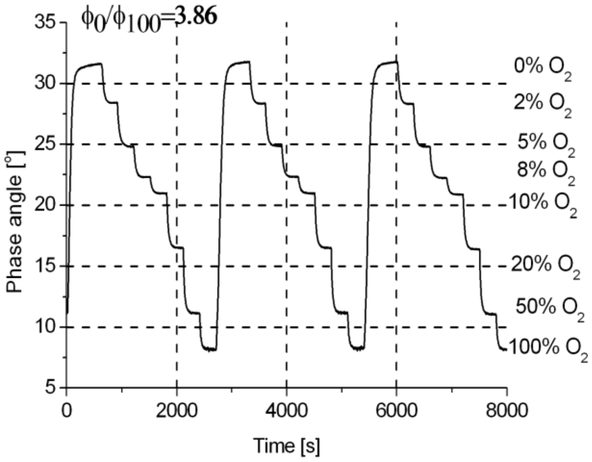

Figure 3.11: Reversibility studies done for the composite nanoparticles doped with ($[Ru(dpp)_3]^{2+}$) prepared by modified Stöber method.

From the obtained results, very good reversibility compared with examples in the literature [10] is observed for the composite nanoparticles over the full dissolved oxygen concentration region.

3.4 Conclusions

In this chapter, the development of oxygen-sensitive composite nanoparticles was described. The synthesis parameters were optimized in order to achieve spherical, monodispersed nanoparticles within a size range compatible with the cellular sensing experiments. Two new approaches, classical and new modified Stöber-based nanoparticle synthesis, were investigated. A significant enhancement in the oxygen-sensitivity of the composite nanoparticles was successfully achieved due to the introduction of the new modified Stöber synthesis route. This improvement may be caused by a more efficient incorporation of pre-hydrolysed MTEOS into the nanoparticle matrix; however, some more detailed studies of nanoparticle composition and porosity such as Fourier Transform Infrared Spectroscopy (FTIR), X-ray Photoelectron Spectroscopy (XPS) and BET, are required to prove this hypothesis. The ($[Ru(dpp)_3]^{2+}$)-doped nanosensor displayed very good repeatability, reversibility and temporal stability.

The other goal, the design and development of composite nanoparticles for ratiometric measurements, was also successfully accomplished. The introduction of APTES to the reaction environment for the covalent binding of the reference dye – ATTO488NHS ester to the composite nanoparticle resulted in a relative decrease in the nanosensor oxygen response compared to that obtained for the composite nanoparticles doped only with ($[Ru(dpp)_3]^{2+}$). It is proposed that the catalytic activity of APTES present in the reaction mixture may influence the reaction kinetics and may result in a denser silica network. Some further studies on the nanoparticle porosity are necessary to confirm this hypothesis. It was shown, based on the leaching studies, that the highly water-soluble ATTO488NHS ester is well incorporated in the nanoparticle structure, which allows for reliable ratiometric detection.

Finally, it was shown that, in the physiological range of oxygen concentration, both types of nanosensor, for the lifetime- and ratiometric-detection, are well fitted to the linear Stern-Volmer plot, which simplifies the process of the data analysis.

References

[1] Buck, S. M.; Koo, Y. E. L.; Park, E.; Xu, H.; Philbert, M. A.; Brasuel, M. A.; Kopelman, R. Optochemical nanosensor PEBBLEs: photonic explorers for bioanalysis with biologically localized embedding. *Curr. Opin. Chem. Biol.,* **2004***, 8*, 540-546.

[2] Albanese, A.; Tang, P. S.; Chan, W. C. W. The effect of nanoparticle size, shape, and surface chemistry on biological systems. *Annu. Rev. Biomed. Eng.,* **2012***, 14*, 1-16.

[3] Iversen, T.; Skotland, T.; Sandvig, K. Endocytosis and intracellular transport of nanoparticles: Present knowledge and need for future studies. *Nano Today,* **2011***, 6*, 176-185.

[4] S. H.; Herricks, T.; Lee, Y. T.; Xia, Y. N. Synthesis and characterization of monodisperse silica colloids loaded with superparamagnetic iron oxide nanoparticles. *Chemical Physics Letters,* **2005***, 401*, 19-23.

[5] Bagwe, R. P.; Yang, C.; Hilliard, L. R.; Tan, W. Optimization of dye-doped silica nanoparticles prepared using a reverse microemulsion method. *Langmuir,* **2004***, 20*, 8336-8342.

[6] Fouilloux, S.; Desert, A.; Tache, O.; Spalla, O.; Daillant, J.; Thill, A. SAXS exploration of the synthesis of ultra monodisperse silica nanoparticles and quantitative nucleation growth modeling. *J. Colloid Interface Sci.,* **2010***, 346*, 79-86.

[7] Bihari, P.; Vippola, M.; Schultes, S.; Praetner, M.; Khandoga, A. G.; Reichel, C. A.; Coester, C.; Tuomi, T.; Rehberg, M.; Krombach, F. Optimized dispersion of nanoparticles for biological in vitro and in vivo studies. *Particle and Fibre Toxicology,* **2008***, 5*, 14.

[8] Moreno, M. J.; Monson, E.; Reddy, R. G.; Rehemtulla, A.; Ross, B. D.; Philbert, M.; Schneider, R. J.; Kopelman, R. Production of singlet oxygen by $Ru(dpp(SO_3)_2)_3$ incorporated in polyacrylamide PEBBLES. *Sensors Actuators B: Chem.,* **2003***, 90*, 82-89.

[9] Tang, Y.; Tehan, E.; Tao, Z.; Bright, F. Sol-gel-derived sensor materials that yield linear calibration plots, high sensitivity, and long-term stability. *Anal. Chem.* **2003***, 75*, 2407-2413.

[10] Xu, H.; Aylott, J. W.; Kopelman, R.; Miller, T. J.; Philbert, M. A. A real-time ratiometric method for the determination of molecular oxygen inside living cells using sol-gel-based spherical optical nanosensors with applications to rat C6 glioma. *Anal. Chem.,* **2001***, 73*, 4124-4133.

[11] Wencel, D. Sol-gel-derived optical oxygen, pH and dissolved carbon dioxide sensors. Ph. D. Thesis, Dublin City University, 2008.

[12] “Excitation and emission spectra of ATTO488”. http://www.fluorophores.tugraz.at/Substance/150.

Chapter 4

pH-sensitive silica nanoparticles

4.1 Introduction

In this chapter, the synthesis and characterization of ratiometric pH-sensitive nanoparticles are described. To facilitate proton ingress into the nanoparticle matrix, the hydrophilic TEOS precursor was used for the nanoparticle synthesis. In order to perform the ratiometric measurements, which are described in section 2.5.2, the pH-sensitive fluorescein isothiocyanate (FITC) and the pH-insensitive Texas Red used as a reference dye, were covalently bound to the nanoparticle matrix. Another approach involving the physical entrapment of the pH-sensitive dye HPTS, was investigated in parallel. The dual-excitation nature of HPTS, which allows for the ratiometric detection without incorporation of the reference dye into the nanoparticle structure, is a very attractive feature from the optical detection point of view. In the experimental part of the chapter, the characterisation results of all nanoparticles, namely their size and zeta potential (described in section 3.3.3.2) using DLS and TEM techniques are presented. The nanosensors were then calibrated ex-vivo on the microplate reader. The conclusions from these preliminary results are presented at the end.

4.2 Materials and methods

4.2.1 Reagents and materials

TEOS, APTES, EtOH, NH_4OH (28% v/v), DMSO anhydrous and fluorescein 5(6)-isothiocyanate (FITC) were purchased from Sigma Aldrich. Sulforhodamine 101 acid chloride (Texas Red-X), succinimidyl ester, mixed isomers was obtained from Molecular Probes. Potassium salts of hydrogen phosphate (K_2HPO_4) and dihydrogen phosphate (KH_2PO_4), used to prepare buffer solutions of defined pH, were purchased from Sigma Aldrich. Standard buffer solutions (pH 4.0, 7.0 and 10.0) were obtained from VWR International. Polystyrene bottom transparent 96-well microplates were obtained from Thermo Fisher Scientific. Aqueous solutions used for nanoparticle dispersion were prepared from deionised (DI) water. All chemicals were of analytical grade and were used without further purification.

4.2.2 Buffer preparation

10mM phosphate buffers stock solutions with acidic and basic pH were prepared by dissolving 1.36g of KH_2PO_4 and 1.74g of K_2HPO_4 in 1 L of DI water, respectively. By combining the stock solutions in different proportion, calibration buffers of the desired pH were obtained. To adjust the value of pH to a certain level, a pH meter calibrated with standard buffer solutions (pH 4.0, pH 7.0 and pH 10.0) was used. The preparation of buffer solution at pH 10.0 required the addition of sodium hydroxide.

4.2.3 Fabrication of pH nanosensors

The (W/O) reverse microemulsion synthesis of HPTS-doped nanoparticles

The HPTS-doped nanoparticles were synthesized by a standard (W/O) quaternary reverse microemulsion protocol found in the literature [1]. First, 7.5ml of cyclohexane, 1.77ml of Triton X-100 and 1.6ml of n-hexanol were mixed on the stirrer at room temperature to generate the microemulsion system. Then, 0.48ml of 20mM HPTS aquatic solution was added to the mixture. After 10 minutes, 100µl of TEOS was pipetted to the reaction vial. Thirty minutes later, 60µl of NH_4OH was introduced to initiate the hydrolysis of TEOS. The reaction was allowed to stir for 24 hours at room temperature. To recover the nanoparticles, the microemulsion was broken by the addition of 20ml of EtOH. At the end of the process, the nanoparticles were washed by centrifugation (8320rcf, 30 minutes) 3 times with EtOH and final washing with water was carried out. After each centrifuge step (8320rcf, 30 minutes) the nanoparticles were dispersed in EtOH and finally in DI water using an ultrasonicator.

Conventional Stöber synthesis of FITC/Texas Red-doped nanoparticles

The nanoparticles containing pH-sensitive FITC and Texas Red acting as the reference dye were successfully fabricated using the conventional Stöber synthesis. FITC was incorporated into the nanoparticle structure through the isothiocyanate amine-reactive linker. For the conjugation of the reference dye with the nanoparticle matrix, a modified form of Texas Red with NHS ester was chosen. This NHS-ester derivative, upon the reaction with APTES, forms an amide bond, which then is used to immobilize Texas Red within the nanoparticle core.

This additional step therefore was done prior to the nanoparticle synthesis, when both of the fluorophores were linked to APTES according to the protocol reported in the literature [2]. Stock solution of FITC in DMSO (11.8µl of $5x10^{-3}$M) was mixed with 37.7µl of DMSO and 0.5µl of APTES and left on the stirrer for 3 hours. In parallel, 4.9 µl of $12x10^{-3}$M stock solution of Texas Red NHS ester in DMSO and 0.5µl of APTES were added to 45.1µl of DMSO and left to react for 3 hours. These reactions were carried out in 2ml eppendorfs inserted into a glass vial, which then were put on the stirrer. The resulting FITC-APTES and Texas Red-APTES conjugates were used without further purification.

The main reaction mixture was prepared in a glass vial according to the conventional Stöber synthesis described in section 3.2.2. TEOS (0.5ml) was added to 12.2 ml of EtOH and mixed on the stirrer for 15 minutes. Then the formation of nanoparticles was initiated by addition of 0.75 ml of NH_4OH to the reaction mixture. Three hours later, Texas Red-APTES conjugate was pipetted into a reaction vial. After another 3 hours, the FITC-APTES conjugate was introduced to the reaction mixture, which was followed by the addition of 0.5ml of TEOS. After 24 hours of synthesis, the nanoparticles were collected and washed three times in EtOH using the centrifuge (8320rcf, 30 minutes). The sample was then stored in the dark under ambient conditions. The synthesis and subsequent experiments were performed at room temperature.

4.2.4 Experimental characterisation systems

4.2.4.1 Fluorescence measurements

Fluorescence spectra were recorded using the FluoroMax-2 spectrofluorometer described in section 3.2.3.4. Nanoparticles were dispersed in water and transferred to a quartz cuvette for the measurements. The excitation spectra were acquired with an emission wavelength set at 515nm for HPTS and FITC and 609nm for Texas Red to match the maximum emission of these fluorophores. The emission spectra were collected employing excitation wavelengths of 490nm and 589nm, which corresponds to excitation peaks of FITC and Texas Red, respectively. 490nm excitation wavelength was used for HPTS. In all measurements 3nm passbands were used for the excitation and emission monochromators.

Calibration experiments were performed on a Safire II microplate reader (Tecan System Inc., Austria). Before measurements, the nanoparticles were diluted in the buffer solutions with different pH (in the range 4.0 to 10.0). Three replicates of 250µl of each nanoparticles buffer solution were pipetted into the 96-well microplate. The same excitation and emission wavelengths were set for the excitation and emission measurements as that applied on FluoroMax-2 spectrofluorometer (see above). In all measurements the bandwidth was set at 5nm and the temperature at 21^{0}C.

Fluorescence spectra obtain from the leaching experiments were acquired on the FluoroMax-2 according to the protocol described in section 3.2.3.5.

4.2.4.2 Other characterisation techniques

The pH of the buffer solutions was measured using a digital Orion Benchtop 420 A+ calibrated with three standard buffers of pH 4.0, 7.0 and 10.0 at room temperature.
The size and the zeta potential of the nanoparticles were investigated using the DLS and TEM instrumentation described in section 3.2.3.2 and 3.2.3.3, respectively.

4.3 Development of pH-sensitive nanoparticles

4.3.1 Development of HPTS-doped nanoparticles synthesised by a (W/O) reverse microemulsion method

The first approach was to employ a very photostable and highly fluorescent HPTS with a pKa around 7.3 to monitor the cytosolic intracellular pH. As mentioned in the introduction, HPTS as a self-referencing dye with two excitation wavelengths at 405nm and 450nm is a perfect candidate for the fabrication of the nanoparticles designed for the ratiometric detection. The HPTS-doped nanoparticles were synthesized using the microemulsion technique (described in section 4.2.3). The data acquired from the nanoparticle characterisation is presented in Figure 4.1.

Microemulsion method

HPTS-doped nanoparticles for the ratiometric detection

a) DLS analysis

Hydrodynamic diameter = 84.1 nm ± 14.9 nm

PDI = 0.109

Zeta potential = -47.4 mV

b) TEM imaging (scale bar: 50nm)

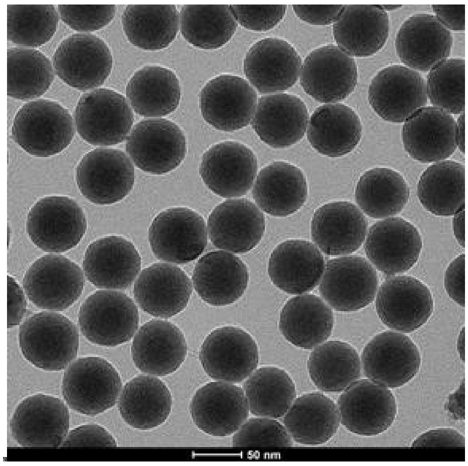

c) Spectroscopic characterization of HPTS

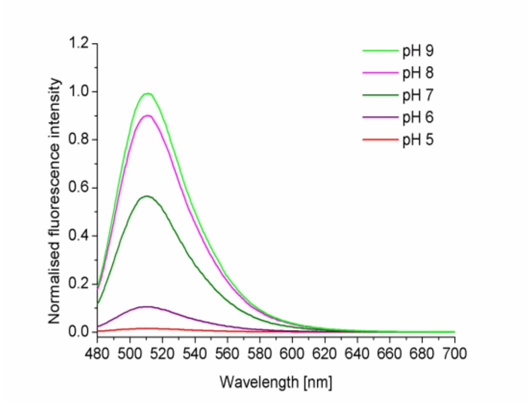

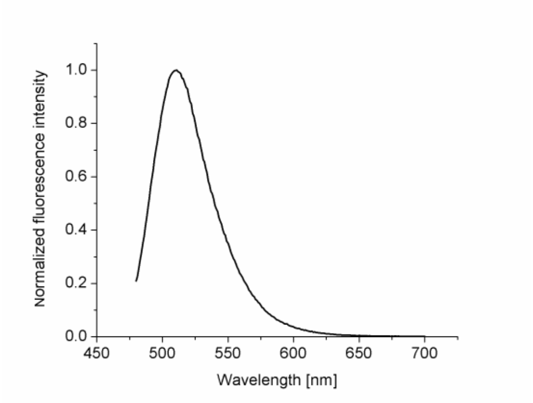

d) Excitation spectra of HPTS-doped nanoparticles (λ_{em} = 515 nm)

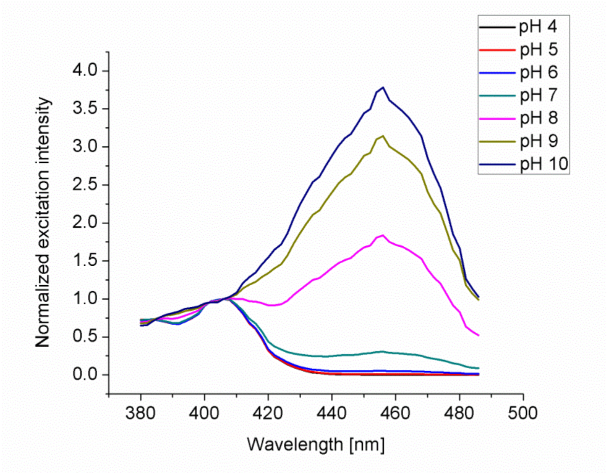

e) Calibration plot obtained for HPTS-doped nanoparticles

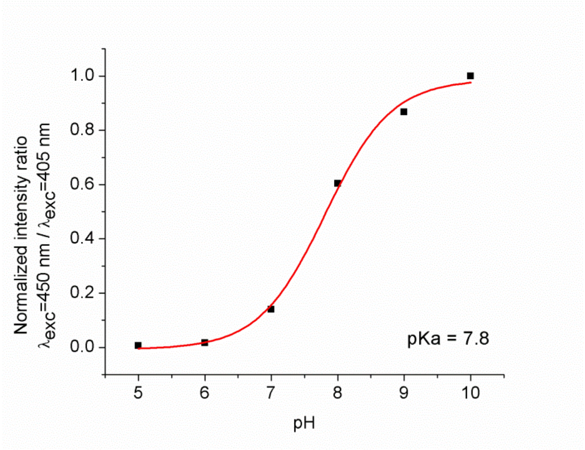

Figure 4.1: The results obtained for the nanoparticles doped with HPTS prepared according to the microemulsion method: a) size and zeta potential measurements, b) TEM imaging, c) spectroscopic characterization of HPTS (excitation spectra – left, emission spectrum - right), d) fluorescence spectra acquired for the nanoparticles dispersed in the buffer solution with different pH, e) calibration plot.

The hydrodynamic diameter of HPTS-nanoparticles measured by DLS is around 85nm. The TEM images revealed a monodispersed population of nanoparticles with an average size of around 60 nm. As explained in section 3.3.3.2, the sample before TEM measurement is dried on a TEM grid, which results in a smaller size of the nanoparticle detected by this technique compared to that measured using DLS. A low zeta potential value (~-47mV) obtained from DLS indicates a good stability of the nanoparticles in water [3]. The excitation spectra were collected for the emission wavelength of HPTS at 515 nm. From the spectra measured for the nanoparticles dispersed in the buffer solutions with different pH, the calibration plot was obtained. This plot was used to quantify the pKa value of HPTS-doped nanoparticles (pKa~7.8). A shift in pKa of the nanoparticles toward a higher value compared to that one reported for the free dye molecules (7.3) is observed, which is possibly caused by the different microenvironment of HPTS [4].

Due to the very good solubility of HPTS in water, a leaching experiment was performed for the nanoparticles. The data obtained from this study is presented in Figure 4.2.

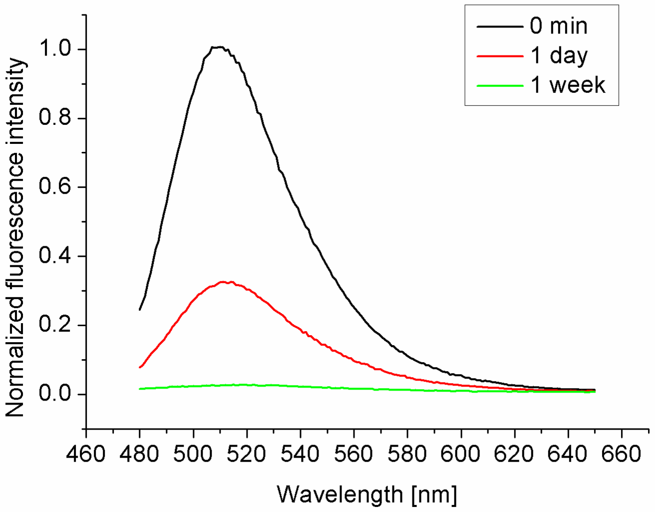

Figure 4.2: Leaching study done for the HPTS-doped nanoparticles synthesized by the microemulsion technique.

As can be observed from the spectroscopic measurements, an extensive (almost 100%) leaching of HPTS from the nanoparticle matrix was detected. Despite many different strategies from the literature including addition of a positively charged cationic surfactant to a classical Stöber synthesis [5], optimisation of the reverse microemulsion method for obtaining denser nanoparticle structure [6] as well as exchanging HPTS for its less water-soluble derivative [7], the leaching problem was not solved and therefore the synthesis of HPTS-doped nanoparticles was not continued.

4.3.2 Development of FITC/Texas Red-doped nanoparticles synthesised by a conventional Stöber method

The most successful approach to pH-sensitive nanoparticle synthesis was based on the conventional Stöber method described in section 4.2.3. To immobilize the fluorophores within the nanoparticle matrix and eliminate the leaching problem, both fluorophores, FITC and Texas Red, were covalently bound to the nanoparticle silica network. The nanoparticles were then characterized and the results are presented in Figure 4.3.

Conventional Stöber method
FITC/Texas Red-doped nanoparticles for the ratiometric detection
a) DLS analysis
Hydrodynamic diameter = 85.3 nm ± 13.5 nm **PDI** = 0.089 **Zeta potential** = -48.4 mV
b) TEM imaging (scale bar: 50nm)
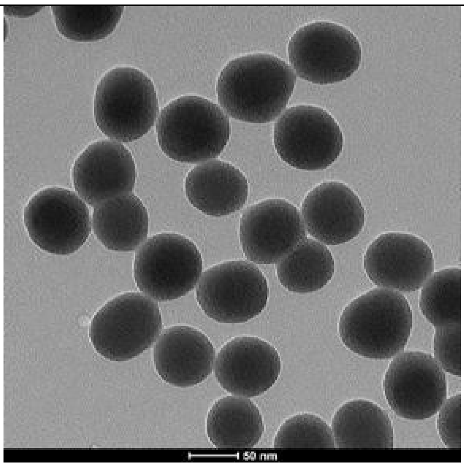

<table>
<tr><td colspan="2">c) Spectroscopic characterization</td></tr>
<tr><td>FITC</td><td>Texas Red</td></tr>
<tr><td>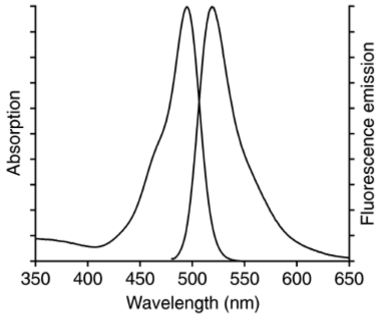 </td><td>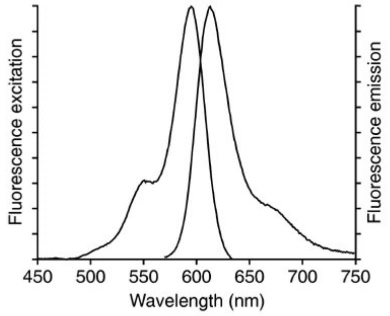 </td></tr>
<tr><td colspan="2">d) Emission spectra (calibration experiment)
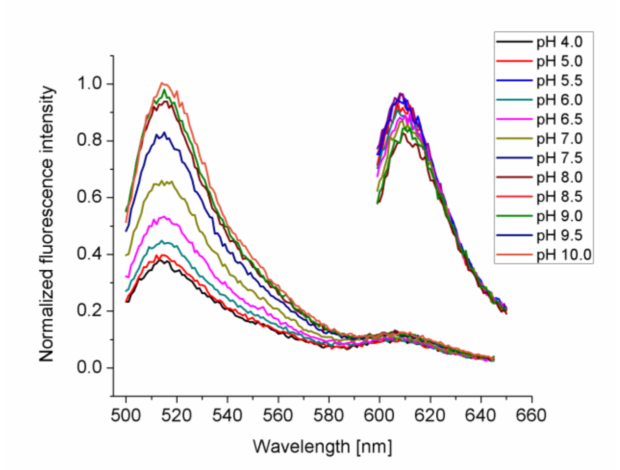 </td></tr>
<tr><td colspan="2">e) Calibration plot
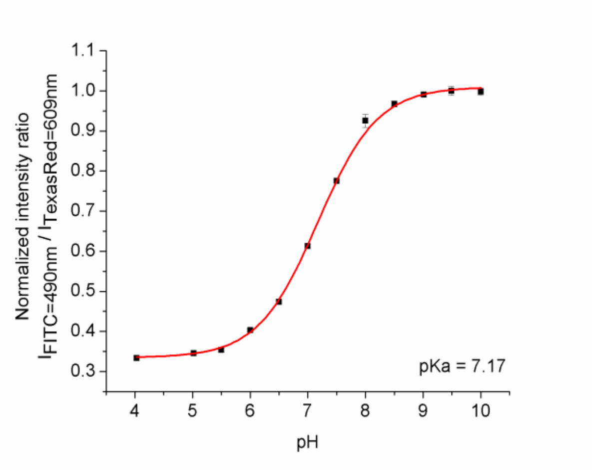 </td></tr>
</table>

Figure 4.3: The results obtained for the nanoparticles containing FITC and Texas Red prepared according to the Stöber method: a) size and zeta potential measurements, b) TEM imaging, c) spectroscopic characterization of FITC and Texas Red, d) fluorescence spectra acquired for the nanoparticles dispersed in the buffer solution with different pH, e) calibration plot.

The hydrodynamic size and PDI obtained from DLS measurements for FITC/Texas Red-doped nanoparticles were equal to 75.3 nm ± 13.5 nm and 0.089, respectively. The DLS results were verified, by an alternative method, TEM, which revealed the population of monodispersed nanoparticles on the images with an average size of around 50nm measured for the dried sample (the difference in the nanoparticle size between DLS and TEM was described in previous section). The calibration plot was acquired based on the emission spectra collected for excitation wavelengths of FITC and Texas Red at 490nm and 589nm, respectively. Then, from the ratio of the intensity maxima ($I_{FITC}/I_{Texas\ Red}$) at different pH, the sigmoidal fit was obtained. The value of pKa was equal 7.17, which means that these FITC/Texas Red –doped nanoparticles are suitable for the cellular application. When comparing this value to pKa of free molecules of FITC dissolved in water (pKa~6.4 [8]), the shift toward higher pKa value is observed, what can be a result of different luminophore microenvironment [9].

4.4 Conclusions

The synthesis and characterization of pH-sensitive nanoparticles was described in this chapter. Both techniques, the conventional Stöber and the microemulsion technique, were employed for the nanoparticle fabrication. In the first approach, highly photo stable HPTS was used for the synthesis but unfortunately this water-soluble fluorophore was almost completely leaching out from the nanoparticles within 1 week. The new successful strategy was based on a covalent binding of pH-sensitive FITC and Texas Red, used as the reference dye, to the nanoparticle matrix. These nanoparticles, obtained via conventional Stöber method were then characterized, calibrated and sigmoidal fit was done for obtained data. The pKa was calculated from the calibration plot and its value was around 7.2. It implies that this sensor could be suitable for intracellular measurement of pH within the cytosol where the pH is around 7.4. For sensing pH values inside lysosomes and endosomes, another pH-sensitive dye with lower pKa value would need to be incorporated into the nanosensor.

References

[1] Bagwe, R. P.; Yang, C.; Hilliard, L. R.; Tan, W. Optimization of dye-doped silica nanoparticles prepared using a reverse microemulsion method. *Langmuir,* 2004*, 20*, 8336-8342.

[2] Schulz, A.; Woolley, R.; Tabarin, T.; McDonagh, C. Dextran-coated silica nanoparticles for calcium-sensing. *Analyst,* **2011***, 136*, 1722-1727.

[3] Bihari, P.; Vippola, M.; Schultes, S.; Praetner, M.; Khandoga, A. G.; Reichel, C. A.; Coester, C.; Tuomi, T.; Rehberg, M.; Krombach, F. Optimized dispersion of nanoparticles for biological in vitro and in vivo studies. *Particle and Fibre Toxicology,* **2008***, 5*, 14.

[4] Patra, D.; Amali, A. J.; Rana, R. K. Preparation and photophysics of HPTS-based nanoparticle-assembled microcapsules. *Journal of Materials Chemistry,* **2009***, 19*, 4017-4021.

[5] Suteewong, T.; Sai, H.; Lee, J.; Bradbury, M.; Hyeon, T.; Gruner, S. M.; Wiesner, U. Ordered mesoporous silica nanoparticles with and without embedded iron oxide nanoparticles: structure evolution during synthesis. *Journal of Materials Chemistry,* **2010***, 20*, 7807-7814.

[6] Osseo-Asare, K.; Arriagada, F. J. Preparation of SiO_2 nanoparticles in a non-ionic reverse micellar system. *Colloids and Surfaces,* **1990***, 50*, 321-339.

[7] Wencel, D. Sol-gel-derived optical oxygen, pH and dissolved carbon dioxide sensors. Ph. D. Thesis, Dublin City University, 2008.

[8] Hendrick, E.; Frey, M.; Herz, E.; Wiesner, U. Cellulose Acetate Fibers with Fluorescing Nanoparticles for Anti-counterfeiting and pH-sensing Applications. *Journal of Engineered Fibers and Fabrics,* **2010***, 5*, 21-30.

[9] Moreno, M. J.; Monson, E.; Reddy, R. G.; Rehemtulla, A.; Ross, B. D.; Philbert, M.; Schneider, R. J.; Kopelman, R. Production of singlet oxygen by $Ru(dpp(SO_3)_2)_3$ incorporated in polyacrylamide PEBBLES. *Sensors Actuators B: Chem.,* **2003***, 90*, 82-89.

Chapter 5

Intracellular sensing

5.1 Introduction

In the last decade, optical PEBBLE nanosensors have been developed in order to monitor processes occurring at the cellular level [1]. Many different factors have to be considered while designing the nanosensor for intracellular imaging and sensing, including the size and charge of the nanoparticles, the method of delivering the nanoparticles to the specific cell line as well as the influence of the nanomaterial on the cellular environment [2]. In the case of nanosensing an additional factor has be taken into consideration, which is the potential change in the nanosensor response upon its introduction to a complex cellular environment. In this chapter, the results obtained from cellular uptake and intracellular sensing experiments are described. Different methods of delivering the nanoparticles into the cells were tested on various cell lines. The intracellular sensing part is focused on the detection of oxygen. Due to time and other constraints, although pH nanosensors have been developed as reported in Chapter 4, it was not possible to progress the study of intracellular sensing with these nanoparticles. This is included under Future work in Chapter 6.

5.2 Materials and methods

5.2.1 Reagents and materials

General buffers

Phosphate buffer saline (PBS) (GIBCO): 13.7mM $NaCl_2$, 27mM KCl, 100mM Na_2HPO_4, 20mM NaH_2PO_4. pH 7.3

FACS buffer – BD Biosciences

External buffer: 145mM $NaCl_2$, 2mM KCl, 5mM $NaHCO_3$, 10mM Glucose, 10mM HEPES, 1mM $MgCl_2$, 2.5mM $CaCl_2$. pH 7.3

5.2.2 Cell culture

5.2.2.1 Cell maintenance and growth media

Macrophages J774A.1 cells were maintained in Roswell Park Memorial Institute media 1640 supplemented with 10% v/v fetal bovine serum and 2% v/v Penicillin Streptomycin, all obtained from GIBCO. Human Embryo Kidney (HEK293) cells which were stably transfected with Toll-like receptor 4 (TLR4) and Human Osteosarcoma Epithelial (U_2OS) cells were cultured in Dulbecco's Modified Eagles Medium (DMEM) (Sigma Aldrich) supplemented with 10% v/v fetal bovine serum. All cell lines were maintained between 80% and 90% confluence, at low passage number (below 40) in T-75 flasks (Nunc, Fisher Scientific) at 37^0C, 5%CO_2.

5.2.2.2 Cell passage

Cells were grown up to 90% of confluency and washed three times with 1ml of sterile PBS. Cells were then detached from the bottom of T-75 flasks by addition of 1ml of Trypsin (0.25% w/v) / EDTA (0.02% w/v) solution 1X (Sigma Aldrich) for 10 minutes at 37^0C. In the case of macrophages, adherent cells were detached from the bottom of culture flasks using a scraper. Cells were re-suspended in an appropriate media (described in section 5.2.2.1) in up to 10ml of total volume and transferred into a 15ml sterile centrifuge tube for washing. Cell pellets were collected at 148rcf for 5 minutes at room temperature. The resulting supernatants were removed and cells were re-suspended in 5ml of appropriate complete growth media. Cells were finally passaged at a ratio of 1 to 5 into new T75 flasks.

5.2.2.3 Cell counting

Prior to plating, cell numbers were determined using the trypan blue viability method. Briefly, a sample of resuspended cells was diluted 5 times in PBS containing Trypan Blue (0.4%w/v) (Sigma) and healthy cells were counted on a hemocytometer.

5.2.2.4 Preparation of microscope coverslips

All imaging and time-domain fluorescence lifetime sensing experiments were performed on coated 15mm diameter round coverslips (Deckgläser, Germany). For frequency-domain fluorescence lifetime sensing experiments, cells were grown on 25mm diameter coated round coverslips. The thickness of both types of coverslips was equal 1.5mm.

5.2.2.5 Poly-D-lysine coating

Before coating, the coverslips were washed in 5% (v/v) acetic acid ethanolic solution for 3 hours on a rotating carousel. They were washed several times with distilled water and sterilized by autoclaving. At the end of the process, clean and sterile coverslips were transferred into a 12-well plate and incubated for 3 hours at 37^0C with poly-D-lysine solution diluted in PBS to a final concentration of 30ng/ml. The coated coverslips were finally washed three times in sterile PBS after removing poly-D-lysine solution from the wells.

5.2.2.6 Nanoparticle intracellular delivery procedures

MACROPHAGE UPTAKE

The phagocytosis uptake was performed based on the following standard protocol:

1) The cells were cultured for 24 hours in 6-well plates (Nunc, Fisher Scientific) with a concentration of $5x10^5$ cells per well. Two plates were prepared: one for flow cytometry studies, another one containing coverslips (detailed in section 5.2.2.4), on which macrophages were grown for analysis under the confocal microscope.
2) Lipopolysaccharide (LPS) solution was added for 24h to the wells at a final concentration of 200ng/ml. During this time macrophages, stimulated by LPS, developed the immunological response expressed as an increase in phagocytic activity.
3) There followed the 0,2,6,12,24 hours incubation of the nanoparticles (25µg/well) with macrophages; the negative control was also prepared containing LPS with cells.
4) Cells for flow cytometry were washed 3 times in FACS buffer (PBS, 2% v/v FCS, 0.05g NaN_3 in 100ml) and scraped from a 6 well culture plate. This was followed by centrifugation for 5 min at 148rcf. The cell pellets were then re-suspended in 500µl of FACS buffer and analysed (BD FACS Aria Cell Sorter, USA).
5) For confocal microscopy, coverslips containing macrophages were transferred directly from the culture media to PBS. Coverslips were fixed in acetone for 15 minutes at -20^0C. After washing in PBS, 6µl of the fluorescence mounting media (DAKO, USA) was used to mount coverslips onto microscope slides prior to imaging. The slides were stored protected from the light, in the fridge.

PASSIVE UPTAKE

Passive uptake experiments were done for HEK293 and HEK293 stably transfected with TLR4 cells. All cells were seeded on the poly-D-lysine coated coverslips located in a 12-well plate at density $15x10^4$ cells per well. After 24 hours of incubation at 37^0C the cells were washed 3 times in PBS and fresh complete media containing nanoparticles

(50µg/well) was applied into the wells. The cells were washed three times in PBS, stained, mounted onto microscope slides and imaged using confocal microscopy. Nanoparticle incubation times of 24 hours and 48 hours of nanoparticle uptake were investigated.

CHEMICAL TRANSFECTION

The chemical transfection experiments were performed with HEK293 cells grown on sterile coverslips coated with poly-D-lysine and placed in 12-well plates. Cell concentration was 15×10^4 cells per well. SAINT-MIX reagent (Synvolux Therapeutics, Sweden), which belongs to a group of cationic lipid-based transfection systems, was used for these experiments. The amount of the transfection reagent components (SAINT MIX, HBS buffer) was optimized. In general the protocol consisted of the following steps:

1) 5/50/100µg of nanoparticles were diluted in 100ul of HBS buffer
2) SAINT MIX transfectant (5µl, 10µl, 20ul) was added to the nanoparticles/HBS solution
3) Nanoparticles/SAINT MIX mixture was incubated for 15 minutes at room temperature
4) After the incubation, nanoparticles/SAINT MIX complex was added to the wells with a fresh complete medium
5) 24 hours after nanoparticle transfection, cells were washed in PBS, stained and mounted on the microscope slides for imaging

ELECTROPORATION

The physical transfection with nanoparticles was done using an electroporator (Bio-Rad Gene Pulser, USA). HEK293 (1×10^6 cells/ml) in media containing nanoparticles were placed on ice prior to electroporation. Different parameters were optimized which are listed below:

- amount of nanoparticles: 20µg, 100µg
- voltage applied to the sample: 220V, 260V, 320V
- the capacitance: 960µF

Following electroporation cells were immersed on ice for 5 minutes and then washed in fresh media. After counting on a hemocytometer, the cells were grown on coverslips in 12-well plates at a final concentration $5x10^5$ cells/well. Imaging was carried out 24 hours post transfection.

5.2.2.7 Staining of intracellular compartments

For the intracellular localisation studies, cells were stained using CellMask^{TM} Deep Red Plasma Membrane Stain (Molecular Probes$^{®}$, USA). This dye, due to its amphipathic structure, is loaded very efficiently through its hydrophobic moiety into the cell membrane, while its other component, negatively-charged hydrophilic dye, remains anchored outside the membrane. For membrane staining, the cells grown on the coverslips were taken out from the 12-well plate and put on the paper filter. The cells were then washed three times in sterile PBS and 150µl of staining solution with a concentration of 2.5µg/ml was pipetted on the coverslips with the cells and left at room temperature for 5 minutes. Cells were then washed three times with 150µl of PBS and were mounted on microscope slides using 3µl of Fluorescence Mounting Media.

Mitochondrial staining was performed at 37^{o}C for 30 minutes with the MitoTracker® Deep Red FM (Molecular Probes$^{®}$, USA) diluted in serum-free media at a concentration of 25nM. This staining reagent contains a mildly thiol-reactive chloromethyl moiety, which, once inside the cell, can form covalent bioconjugates with different intra-mitochondrial protein sulfhydryls [3] as presented in Figure 5.1

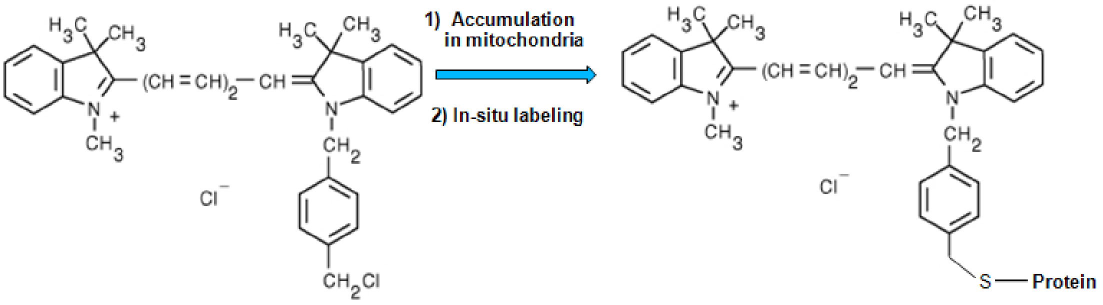

Figure 5.1: Intracellular reactions of the MitoTracker® Deep Red FM.

Before staining, the cells were washed three times in sterile PBS (150µl). Washing and mounting of the cells on the coverslips was performed in the same way as described above for the cell membrane staining protocol.

Both dyes were chosen due to their optical properties ($\lambda_{abs}/\lambda_{em}$ ~644/665 nm), which should not interfere with the broad peaks of excitation and emission of ($[Ru(dpp)_3]^{2+}$) (presented in section 3.3.3.1).

5.2.3 Instrumentation

5.2.3.1 Flow cytometry

Flow cytometry was used for the nanoparticle uptake analysis. This method employs both the laser light scattered by the molecules of interest as well as fluorescence emitted from the fluorophore incorporated in the sample to identify and quantify the cellular components. Samples were loaded into the flow cytometer FACS Aria 1 (BD Biosciences, USA). Due to the pressurized sheath fluid forcing the analysed sample into the center of the chamber and into the capillary, the cells were focused into single file inside the flow cell. While passing through the interrogation point, laser light intersected the cells and, as a consequence, side and forward scattering and fluorescence signals were collected. A 488-nm Coherent® Sapphire™ solid state laser was used as the excitation source. The fluorescence from the ruthenium complex was collected in the 600-620 nm PE-Texas Red® channel. The detection of the scattered light was divided between two pathways depending on the type of the scattering:

- forward scatter light gathered by the photodiode placed along the axis of the laser beam
- side scatter light directed through a system of mirrors and filters to the photomultiplier tube (PMT) at a 90^0 angle [4].

The photons collected by the detectors were then transduced into voltage, which is proportional to the amount of light.

5.2.3.2 Confocal microscopy

Confocal microscopy was used to investigate the intracellular localization of the nanoparticles. Confocal microscopy was performed using a Zeiss LSM 510 META.

($[Ru(dpp)_3]^{2+}$) and ($[Ru(dpp)_3]^{2+}$)/ATTO488-doped nanoparticles were excited with 488nm line of a 100 mW Argon laser beam. The fluorescence from CellMask™ Deep Red Plasma Membrane Stain and MitoTracker® Deep Red FM was stimulated using the 633nm line of Helium-Neon laser beam. The optical filter sets, together with the excitation lines, are described in Table 5.1.

Table 5.1: Optical configuration used on the confocal microscope. NS -non-stained samples, ST- stained samples, HFT (German abbreviation: Haupt-Farb-Teiler) – Primary Dichroic Beamsplitter, NFT (German abbreviation: Neben-Farb-Teiler) – Secondary Dichroic Beamsplitter, LP - long-pass, BP - band-pass. Numbers represent wavelength values in nm.

Sample	**Measurement mode**	**Excitation filter**	**Dichroics Main *secondary***	**Channel**	**Emission filter**
NS	Single channel	488	HFT 405/488, *NFT490*	Ch2	LP420
	Single channel	488	HFT 405/488, *NFT545*	Ch2	BP 505-530
				Ch3	LP615
ST	Sequential channel	488	HFT 405/488, *NFT 545*	Ch2	BP 505-530
				Ch3	LP615
		633	HFT 405/488/ /543/633, *NFT545*	Ch3	LP 650

The imaging of non-stained samples was carried out using the backscattered reflection of the laser beam on the glass coverslip (yellow – labelled optical path in Table 5.1). In the case of stained samples, fluorescence from the mitochondrial and cell membrane stains was employed to determine the correct focal plane (green-labelled optical path in Table 5.1). The emitted signals were detected using photomultiplier tubes and transformed into the images. The images were acquired with 63x magnification objective under oil immersion (Plan-Apochromat 63x/1.40 Oil DIC M27) using Zeiss LSM 510 META software and then analysed with Image J.

The other settings used for the imaging are listed below:

- pixel dwell time – 25.6 µs/pixel,
- resolution - 1024 pixels,
- image – 12 bit,

Confocality was achieved by setting pinhole equivalent to 1 airy unit for each channel (896µm and 106µm for 488nm and 633nm excitation respectively).

5.2.3.3 Confocal microscopy with the TCSPC Platform.

Time-domain sensing was accomplished with the Zeiss LSM510 confocal microscope combined with fluorescence lifetime imaging extension modules (Picoquant, Germany). The sample was excited with a 5mW, 50ps 405nm diode laser (LDH405, Picoquant). The excitation source was coupled to the Zeiss LSM microscope and emitted light collected though the same optical fibre. The emitted signal was detected using Single Photon Avalanche Diodes (MPD-SPAD, Picoquant) in the Time-Tagged Time-Resolved (TTTR) format. A TCSPC data acquisition module (PicoHard 300, Picoquant, Germany) tags photon arrival times with respect to the beginning of the experiment and with respect to the laser pulse which allows for reconstruction of 2 dimensional and 3 dimensional fluorescence lifetime modes. A schematic diagram of the time-domain FLIM instrumentation setup is presented in Figure 5.2.

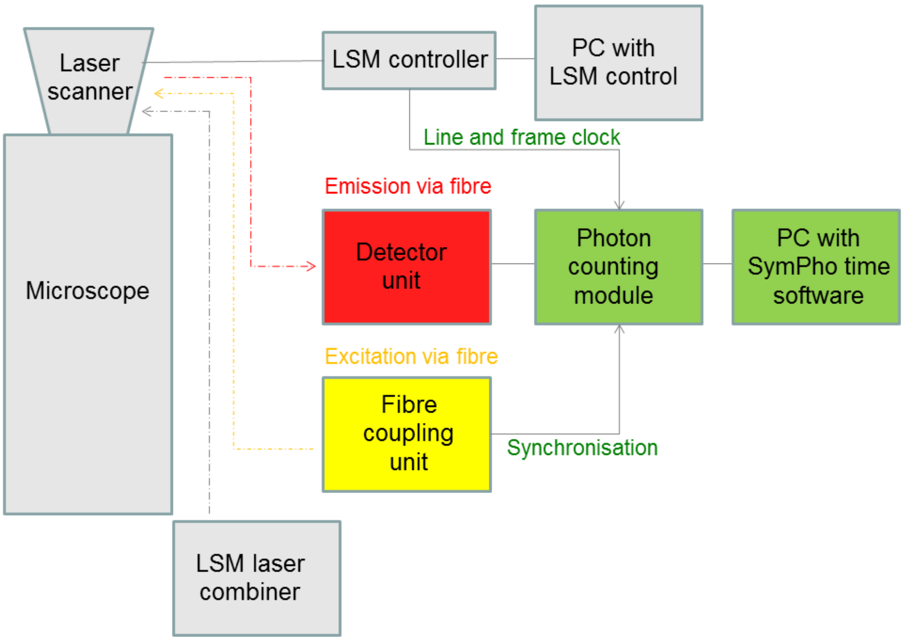

Figure 5.2: Time-domain FLIM microscopy setup.

5.2.3.4 Wide-field frequency-domain fluorescence lifetime microscopy

A Leica DMIRE2 widefield microscope was used for the frequency domain FLIM measurements. Fluorescence was stimulated using a 1W 473nm LED (PicoQuant) modulated at 100kHz and suitable filter sets (Leica I3 filter set: 450-490 band pass excitation filter, 510nm dichroic mirror, 515nm and 540nm long pass emission filters) and visualised at 63x magnification under glycerine immersion (Leica HCX PL APO 37^{0}C X63/A=1.3). To amplify the emission signal, a frequency-modulated image intensifier (Lambert Instruments II18MD) coupled to a CCD camera (Vosskuhler CCD-1300D) was used. Images were acquired and analysed using LI-FLIM 1.2.12 software. The frequency-domain instrumentation scheme is presented below in Figure 5.3.

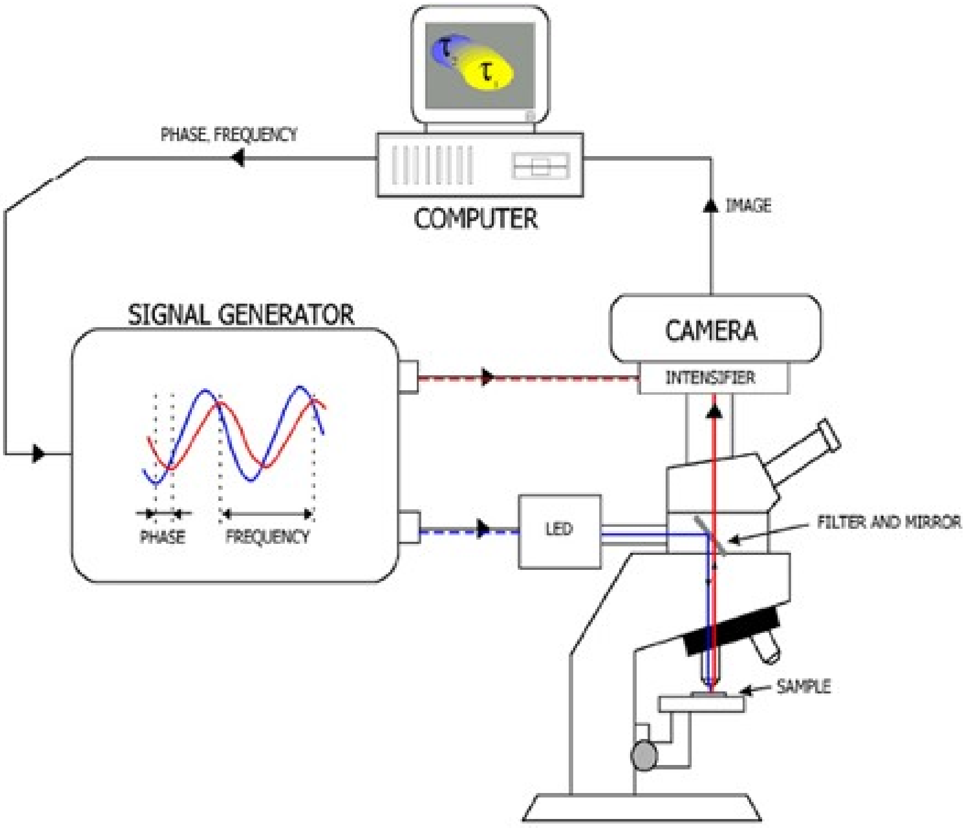

Figure 5.3: Frequency-domain FLIM instrumentation [5].

5.3 Nanoparticle intracellular delivery

Due to the fact that there was no difference in cellular uptake observed for the nanoparticles designed for the lifetime and ratiometric detection as will be shown in the experimental section, the results can be addressed to both types of nanoparticles. The macrophage uptake and electroporation experiments are described using the results obtained for the ($[Ru(dpp)_3]^{2+}$)-doped nanoparticles. For the passive uptake and chemical transfection, the data obtained from the experiments performed with the nanoparticles containing ($[Ru(dpp)_3]^{2+}$) and ATTO488 are presented.

5.3.1 Macrophage uptake

5.3.1.1 Flow cytometry analysis

The results from the phagocytosis uptake were analysed by the flow cytometry method and are presented as histograms displaying the number of events versus their intensities. This is shown in Figure 5.4.

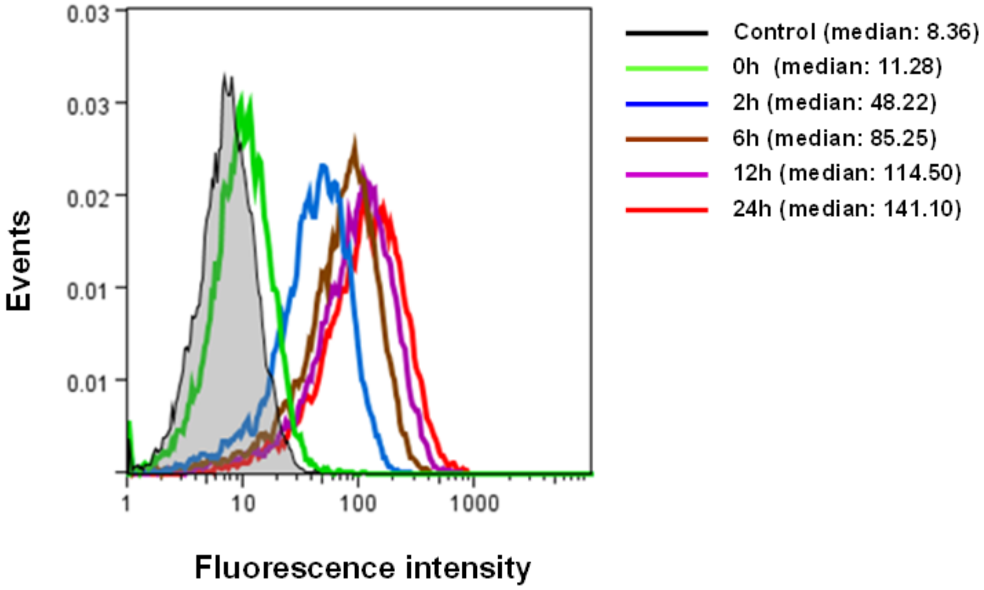

Fig 5.4: Histograms obtained by FACS represent nanoparticle phagocytosis uptake for the different incubation times (0h ,2h ,6h ,12h ,24h) with macrophages together with a negative control (untreated cells).

The negative control and 0 hours incubation samples gave, as expected, a very similar population of low intensity events. No signal from [Ru(dpp$_3$)$^{2+}$]-doped nanoparticles was detected. Increase in time of incubation resulted in the shifting of the peak toward the higher intensity region, so that the mean fluorescence intensity for the final 24h incubation sample was significantly higher in comparison to the negative control and equal to 141.10 arbitrary units. This shift in fluorescence intensity indicates the particle uptake into the cell population.

The data are also illustrated as a cytogram (dot plot), where the side scatter light intensity was plotted versus the forward scatter channel. Each dot represents one event. The set of clusters, equivalent to different populations within the sample, could be therefore distinguished on the plot. Boxes were drawn around regions of the cytogram, which allowed the calculation of the percentage of total fluorescence events within the population [4]. For the longer incubation time, an increase in the amount of events assigned to the macrophages with nanoparticles region from around 2% up to 91% was observed, which is presented in Figure 5.5.

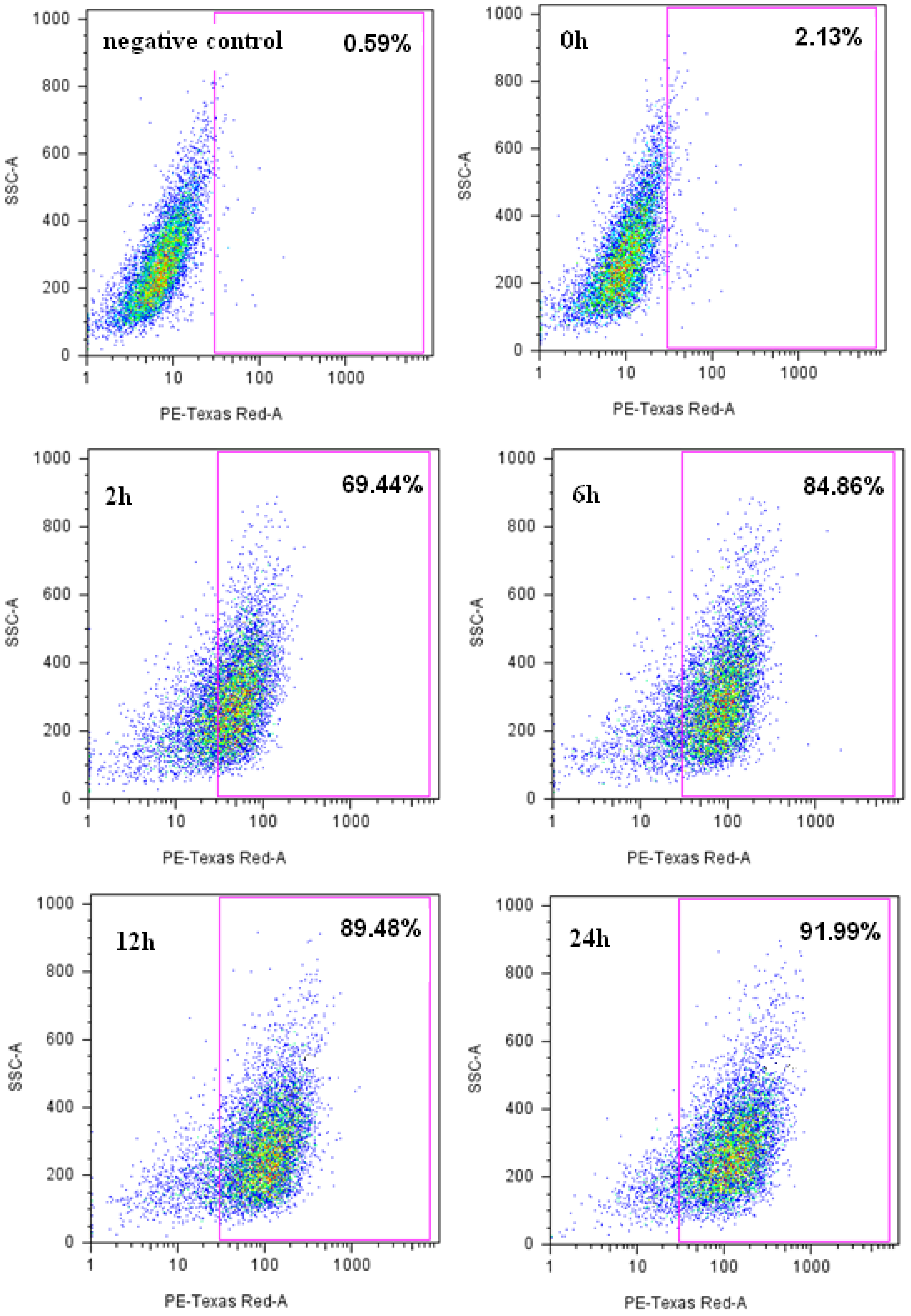

Fig 5.5: Dot plot representation of the phagocytosis assay for the different NPs incubation time with macrophages together with negative control. SSC- side-scattered light. PE-Texas Red – forward scattered light channel with 620BP emission filter.

The population of dead cells was gated out at the time of analysis.

5.3.1.2 Confocal microscopy imaging

As a complementary technique of the nanoparticle uptake analysis, confocal microscopy was employed and the data from the imaging are presented in Figure 5.6.

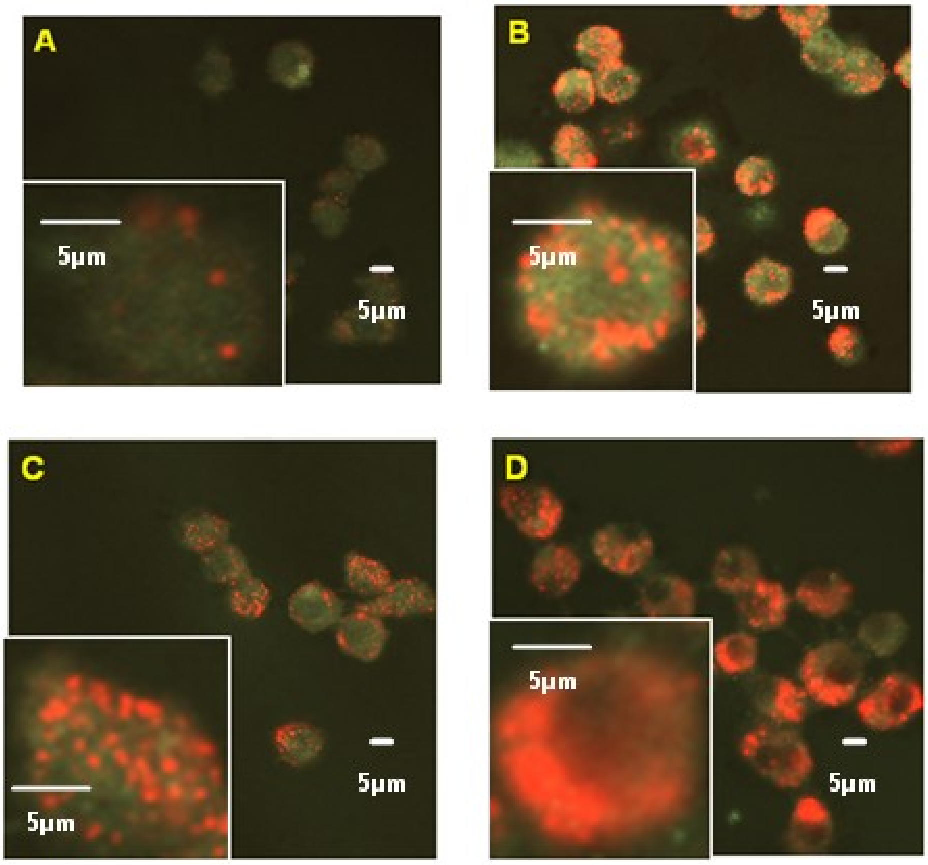

Figure 5.6: Confocal images of macrophages incubated with the ($[Ru(dpp)_3]^{2+}$)-doped nanoparticles (red) for A) 0 h, B) 2h, C) 6h, D) 12h. Non-fluorescent / scattered light was used to identify the cells (green).

For the cells with 0 hours nanoparticle incubation time (Figure 5.6A), where nanoparticles were applied to the cells for a very short time (a few seconds), no nanoparticles appeared to enter the cell. A few isolated nanoparticles occurred on the cell periphery. With this limited exposure time, no nanoparticles are expected to enter the cells through phagocytosis. Phagocytosis has been detected as early as after 10 minutes and the point when uptake saturates depends very much on the analyte of interest [6]. Therefore any nanoparticles visible in Figure 5.6a are presumably bound non-specifically to the outside of the cell. After 2 hours (Figure 5.6B), the amount of nanoparticles visualized inside the macrophages increased dramatically. This uptake is time-dependent with a greater number of nanoparticles seen inside the macrophages after 6 and 12 hours of incubation (Figure 5.6 C and D). The confocal images are in agreement with the flow cytometry results.

5.3.2 Passive uptake

In order to investigate the passive uptake of the nanoparticles, the adherent HEK 293 cell line was used for the experiment. The cells were incubated with the nanoparticles for 24 hours. The results from the passive uptake experiment are shown in Figure 5.7.

HEK 293 cells – passive uptake

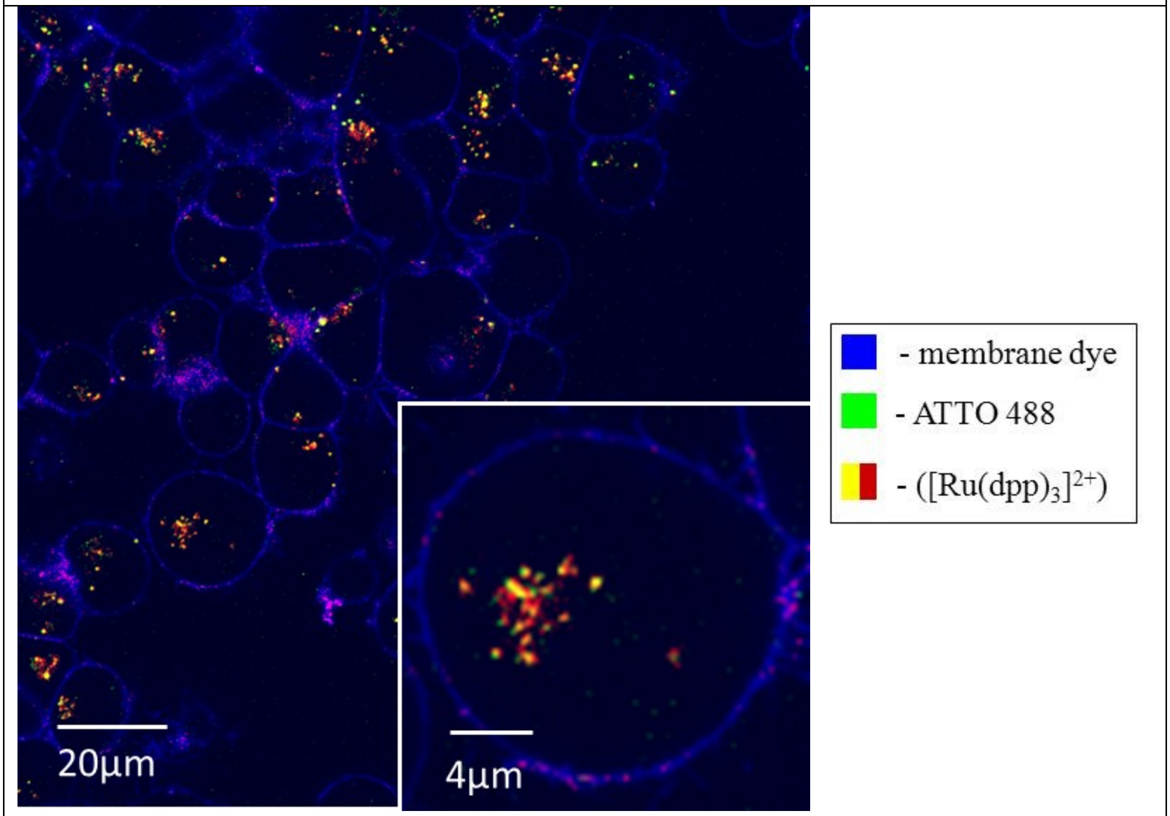

Figure 5.7: Confocal images of HEK293 incubated with the ([Ru(dpp)$_3$]$^{2+}$)/ATTO488-doped nanoparticles for 24h. The luminescence signal from the nanoparticles was collected with 488nm laser into two separate channels, green and red, corresponding to ATTO488 and ([Ru(dpp)$_3$]$^{2+}$), respectively. The cell membrane (blue) was stained with CellMask^{TM} Deep Red Plasma Membrane Stain and imaged with 635 nm laser.

It can be observed from the images that the nanoparticles are passively uptaken by HEK 293 cells up to some extent. To increase the efficiency of the uptake, HEK293 cells were starved for different period of time by the incubation with a serum-free DMEM media [7, 8]. The results from this approach are presented in Figure 5.8.

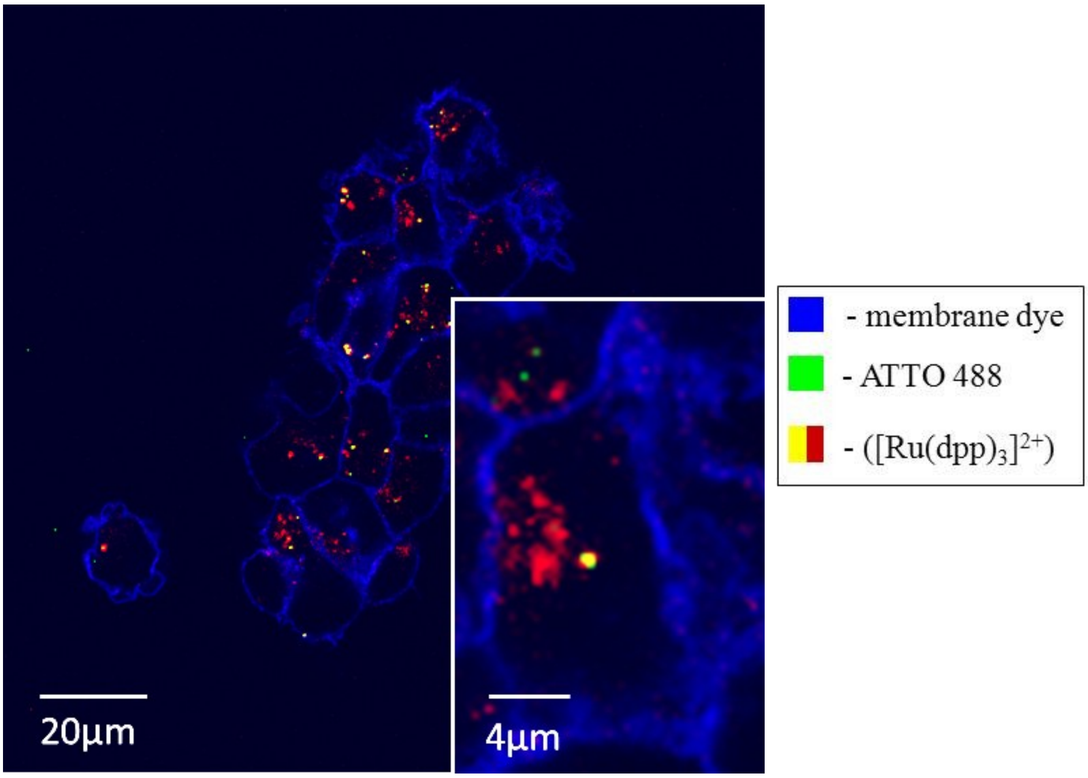

Figure 5.8: Confocal images of HEK293 starved for 5 hours in the serum-free media and then incubated with the ($[Ru(dpp)_3]^{2+}$)/ATTO488-doped nanoparticles in the complete media for 24h. The luminescence signal from the nanoparticles was collected with 488nm laser into two separate channels, green and red, corresponding to ATTO488 and ($[Ru(dpp)_3]^{2+}$), respectively. The cell membrane (blue) was stained with CellMask^{TM} Deep Red Plasma Membrane Stain and imaged with 635 nm laser.

As observed from the confocal images, positive uptake results were obtained for HEK 293 cells when exposed to starvation. However, the cell membrane integrity and overall condition of HEK293 suggests that the cell viability may be affected in the absence of FBS.

5.3.3 Chemical transfection

The chemical transfection experiments were performed according to a protocol described in section 5.2.2.6. Different amounts of SAINT-MIX transfectant were used in the experiment. The images from the confocal microscope are presented in Figure 5.9.

HEK 293 – 5 µl of SAINT-MIX (Membrane stain)

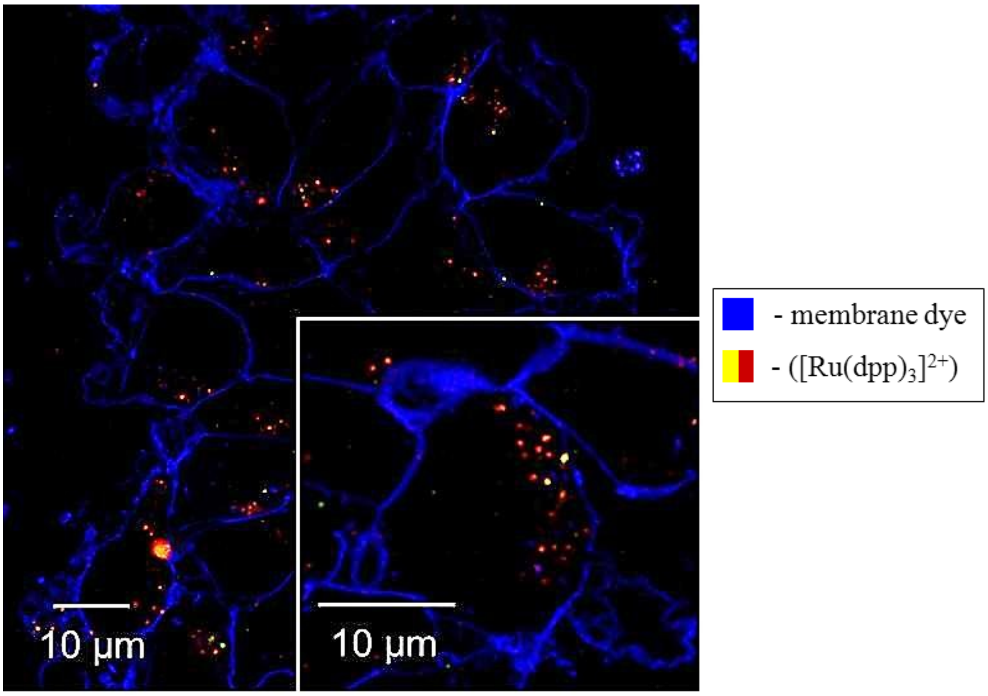

HEK 293 – 10 µl of SAINT-MIX (Membrane stain)

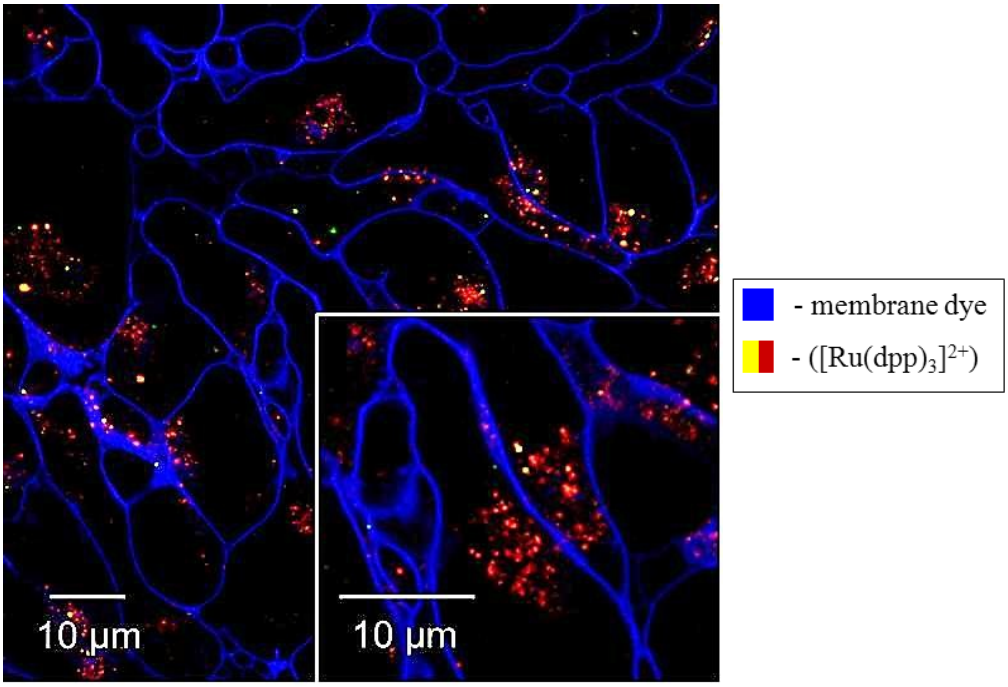

HEK 293 – 20 µl of SAINT-MIX (Membrane stain)

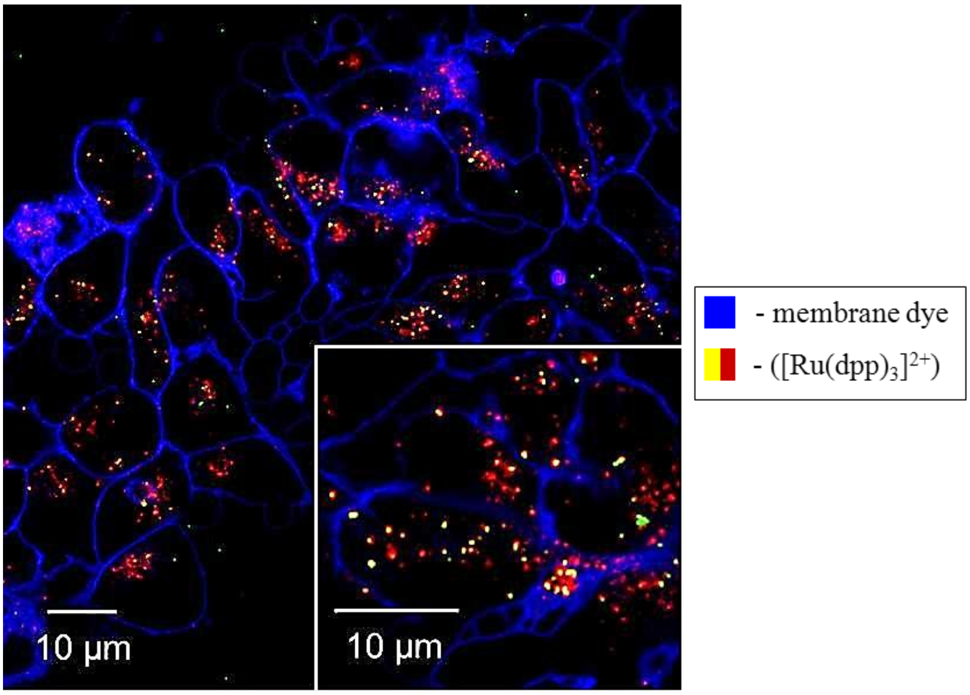

Figure 5.9: Confocal images of HEK293 cells transfected with the ([Ru(dpp)$_3$]$^{2+}$)-doped nanoparticles containing different amount of SAINT-MIX chemical transfectant.

An increase in amount of nanoparticles for the slides with the higher amount of SAINT-MIX transfectant was detected. A difference in intensity redistribution is observed especially for the nanoparticles transfected with the highest amount of transfectant reagent. This could be caused by different factors including the higher permeability of the cell membrane to oxygen. As a consequence, a higher oxygen concentration would be detected, which would result in more efficient quenching of ([Ru(dpp)$_3$]$^{2+}$) and a larger contribution of ATTO488 to the signal. A more disrupted structure for 10µl and 20 µl of SAINT-MIX is as well observed, which supports the previous hypothesis.

5.3.4 Recombinant cell line

Another strategy was to employ HEK 293 transfected with TLR4 receptor. This cell line, due the presence of TLR4, has ability to detect LPS derived from Gram-negative bacteria and, as a consequence, initiate an immunological (phagocytic) response. The phagocytic ability of this cell line was therefore employed for the ($[Ru(dpp)_3]^{2+}$) / ATTO-doped nanoparticle uptake studies. The confocal images obtained from the experiments are presented in Figure 5.10 a, b.

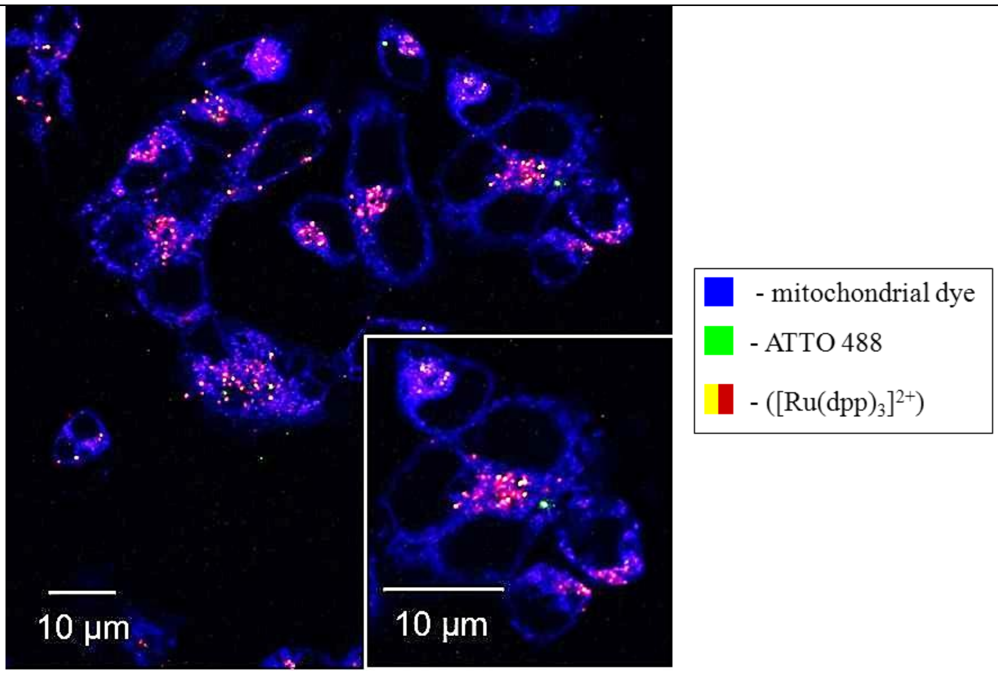

HEK 293 transfected with TLR4 (Mitochondrial stain)

Figure 5.10a : Confocal image of the ($[Ru(dpp)_3]^{2+}$)/ATTO488-doped nanoparticle uptake performed for HEK293 transfected with TLR4 stained with MitoTracker®Deep Red FM dye.

HEK 293 transfected with TLR4 (Membrane stain)

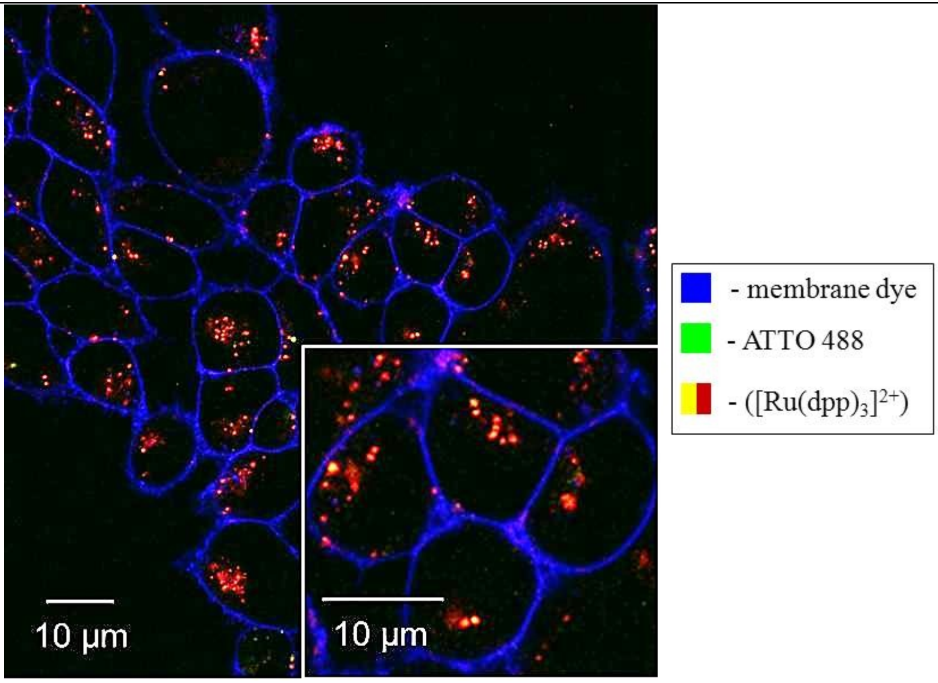

Figure 5.10b : Confocal image of the ($[Ru(dpp)_3]^{2+}$)/ATTO488-doped nanoparticle uptake performed for HEK293 transfected with TLR4 stained with CellMask^{TM} Deep Red Plasma Membrane dye.

The successful uptake is clearly visible from the confocal images (Figure 5.10 a, b). The image of the cells stained with the membrane dye (Figure 5.10b) indicates that morphologically the cells remain unchanged after the nanoparticle uptake therefore the cell integrity is well maintained. This suggests that the nanoparticles are biocompatible.

As seen in Figure 5.10a, the luminescence derived from the nanoparticles and the mitochondrial stain was collected from the same pixels, which reveals that the nanoparticles are located in the proximity or inside the mitochondria. To fully understand whether nanoparticles enter inside mitochondria, some confocal microscopy-based co-localization studies and high resolution TEM imaging of the biological specimens should be performed.

5.3.5 Electroporation

Electroporation was the last nanoparticle delivery technique investigated within these studies. This method is based on the application of an electrical impulse in order to open the pores in the cell membrane and introduce the nanomaterial inside the cell. The results from the electroporation collected for ($[Ru(dpp)_3]^{2+}$)-doped nanoparticles are presented in Figure 5.11.

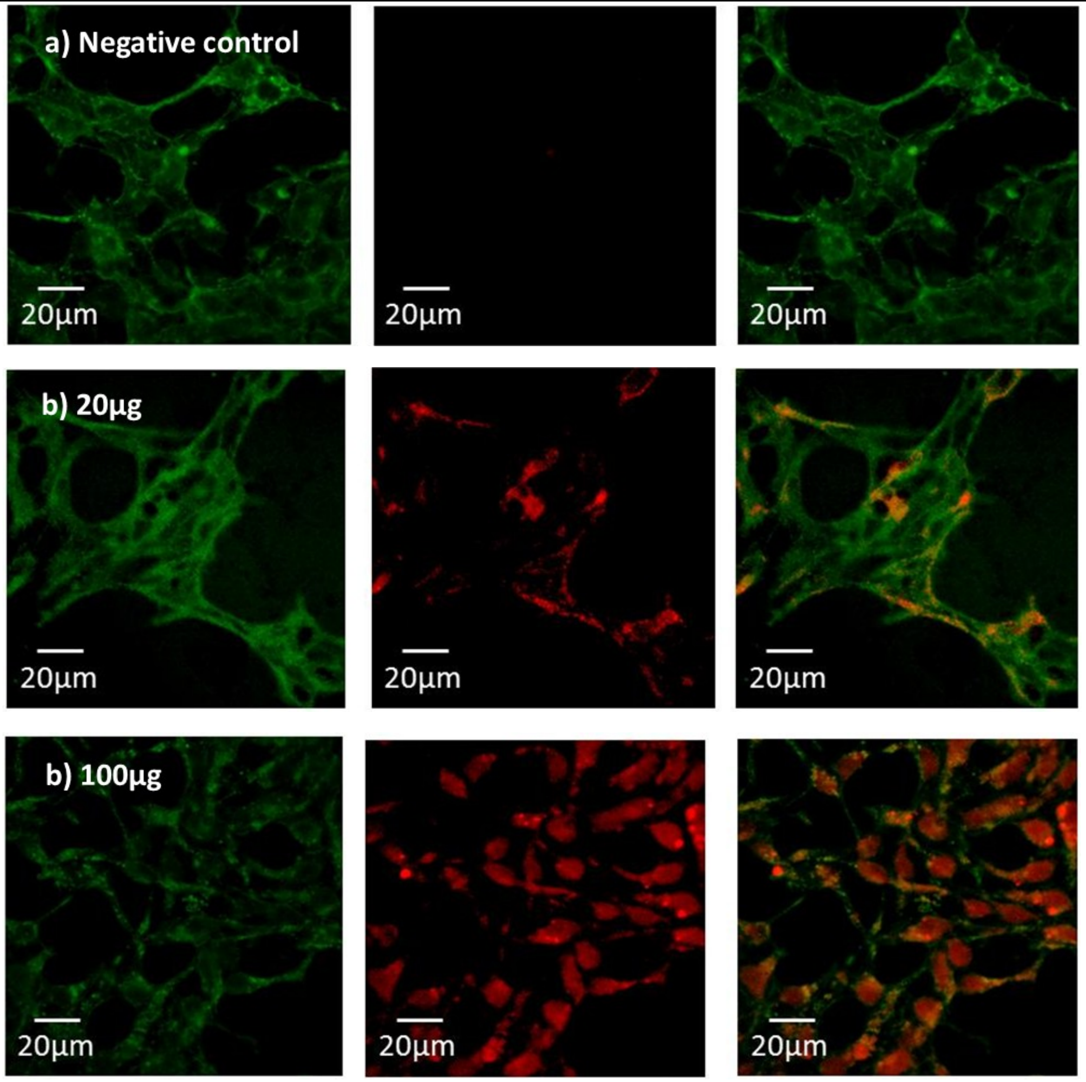

Figure 5.11: Confocal images of HEK293 electroporated with ($[Ru(dpp)_3]^{2+}$)-doped nanoparticles. Green channel (left-hand side): pseudo-coloured images of the cells, red channel (in the middle): images of ($[Ru(dpp)_3]^{2+}$)-doped nanoparticles inside the cell, the composite image reconstructed from both channels (right-hand side).

Confocal images obtained from three different samples (negative control, 20µg and

100µg of nanoparticles) are presented. As expected, HEK293 cells with the highest concentration of nanoparticles applied for the electroporation shows the highest nanoparticle delivery efficiency. The morphology of HEK293 cells after the electroporation is different in comparison to the previous results (see Figures 5.8 and Figure 5.9) obtained from the passive uptake and chemical transfection experiments. It may be caused by the invasive character of this technique. In consequence, the cells after electroporation require more time to spread on the glass coverslip and reach the desired level of co-fluency (~80%) for the confocal imaging. Due to the invasive character of this intracellular delivery method, other approaches were investigated.

5.4 Intracellular oxygen sensing

5.4.1 Time-domain measurements

Oxygen sensing experiments were performed on macrophages using the fluorescence lifetime imaging microscopy (FLIM) technique. Macrophages, due to their ease of maintenance, are a very powerful model system for quantitative biophysical studies of eukaryotes [9].

Six slides with 0h, 2h, 6h, 12h, 24h incubation times and a negative control were prepared for the oxygen sensing experiment according to the protocol described in section 5.2.2.6. The composite ($[Ru(dpp)_3]^{2+}$)-doped nanoparticles were used for this experiment. Five randomly selected areas for each slide were then imaged and analysed in accordance with the steps listed below:

- Focusing on the surface of the slide (Figure 5.12, left side)
- Moving the focus 2um over the surface
- Collecting the wide field fluorescence image (Figure 5.12, in the middle)
- Switching to the FLIM platform and collecting the lifetime map (512x512 resolution, 2.5µs acquisition window, 164µs pixel dwell time) (Figure 5.12, right side)
- Analyzing the fluorescence images with ImageJ image processing program in order to compare an average fluorescence for the slides with a different nanoparticle incubation time.

The images are presented in Figure 5.12.

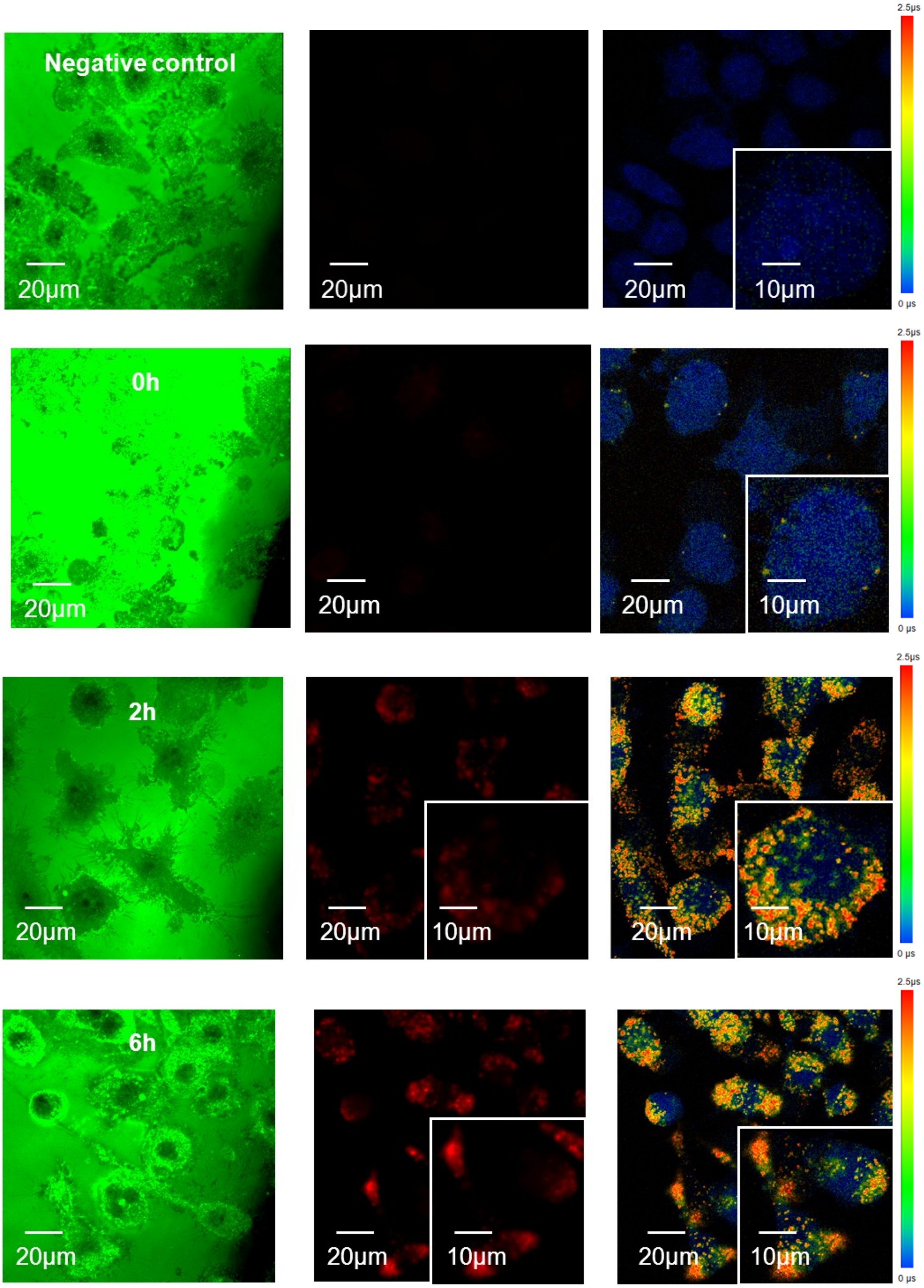

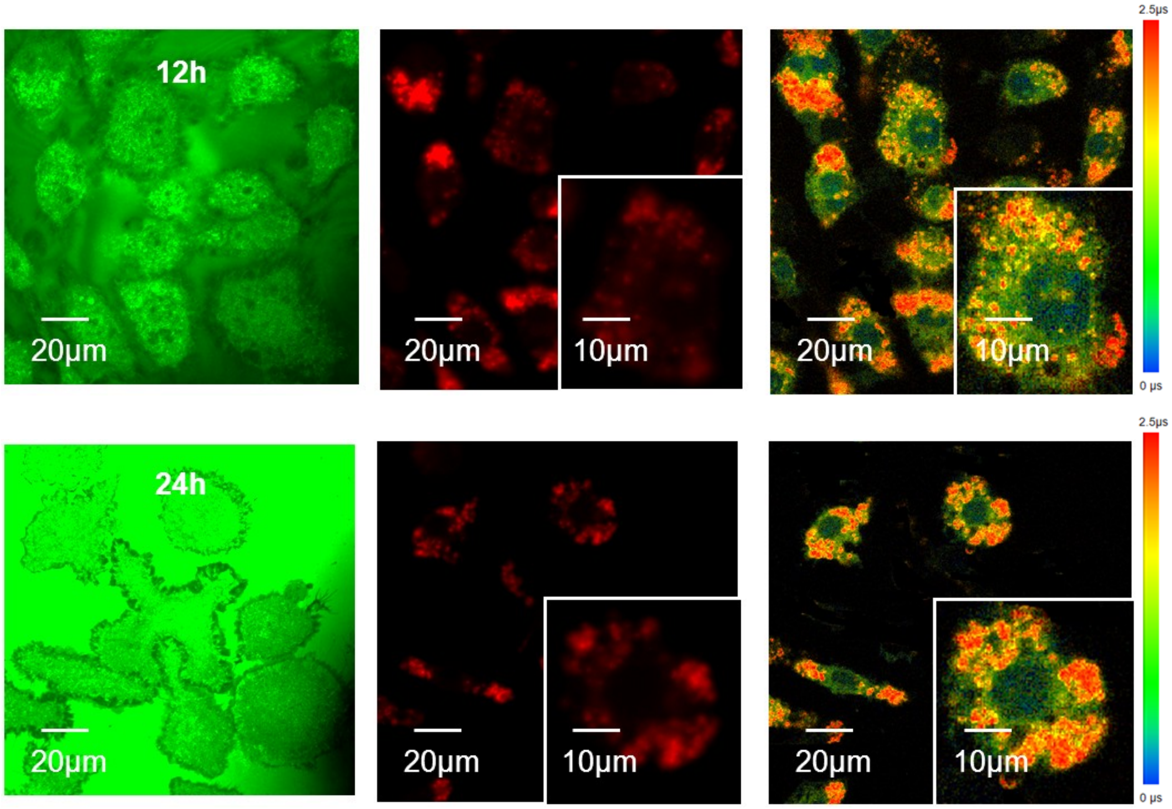

Figure 5.12: Confocal images of macrophages incubated with the ([Ru(dpp)$_3$]$^{2+}$)-doped nanoparticles for negative control, 0h, 2h, 6h, 12h, 24h (left – back scattered image, center – fluorescence image, right – FLIM image).

The fluorescence-based analysis (data not shown) confirmed the flow cytometry results for the negative control, 0h and 2h incubation slides. In the case of the 6h incubation slide, the average fluorescence was higher than for the 12h and 24h incubation slides. It was possibly caused by the difference in the sample preparation (scraping of the macrophages versus simple wash of the slides in PBS).

The FLIM images allowed for ease of distinguishing between the long lifetime nanoparticles (red spots) and the short lifetime endogenous proteins of macrophages (blue regions).

Note that, due to hardware restrictions resulting in a short acquisition window (2.5µs), the colour scale does not show the real values of the lifetime. As it was mentioned in section 2.3.2, the experiments on the macrophages presented in this work, are qualitative. The quantitative analysis is limited to the point measurements due to the µs range lifetime of the ruthenium complex, which requires a very long acquisition window and presents technical limitations regarding the equipment available.

5.4.2 Frequency-domain measurements

Frequency-domain sensing was carried out as part of a European research infrastructure Euro – Bioimaging Proof-of-concept project. The experiments were performed at the Netherlands Cancer Institute in Amsterdam. The scope of this project was to overcome the hardware limitations of the previous time-domain FLIM system and prove that the composite nanoparticles can be used in the intracellular environment to sense the level of oxygen. The experiments were performed on a widefield frequency domain FLIM setup (described in section 5.2.3.4) and the results obtained are discussed below. A new type of the adherent cells, U_2OS, was used in these frequency-domain FLIM experiments. At the beginning it was confirmed that the nanoparticles are uptaken by U_2OS cells. The results from the intracellular localisation of the nanoparticles are presented in the following Figures (Figure 5.13 and Figure 5.14)

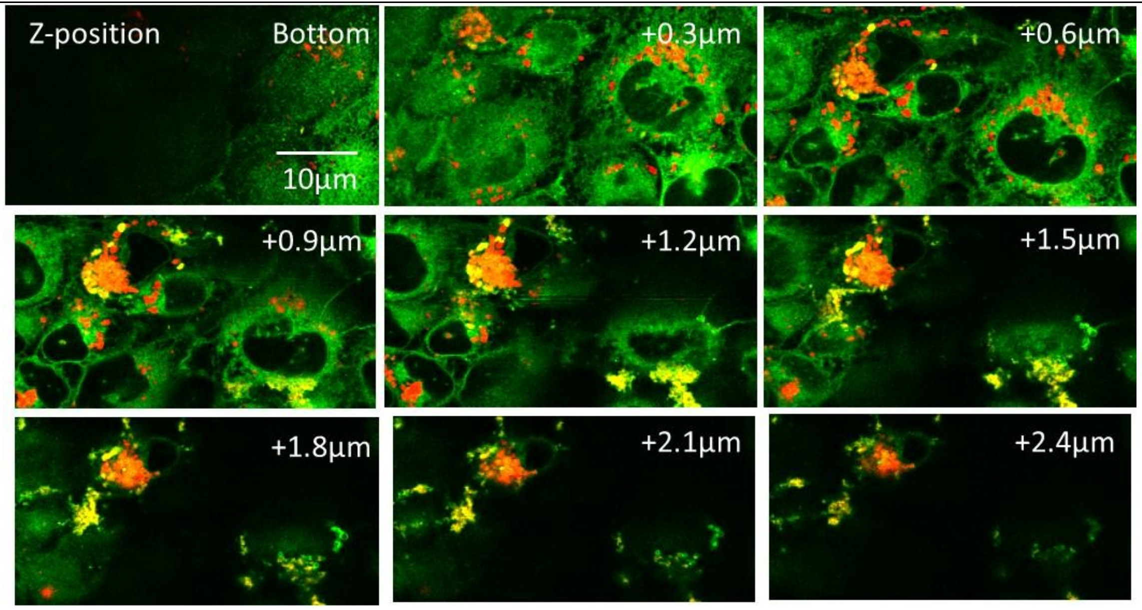

Figure 5.13: Z-stack of confocal microscope images of 24 hours incubated with ($[Ru(dpp)_3]^{2+}$)-doped nanoparticles (passive uptake) U_2OS cells. Each image is a composite of backscatter light (green) and signal from the ruthenium-doped nanoparticles (red).

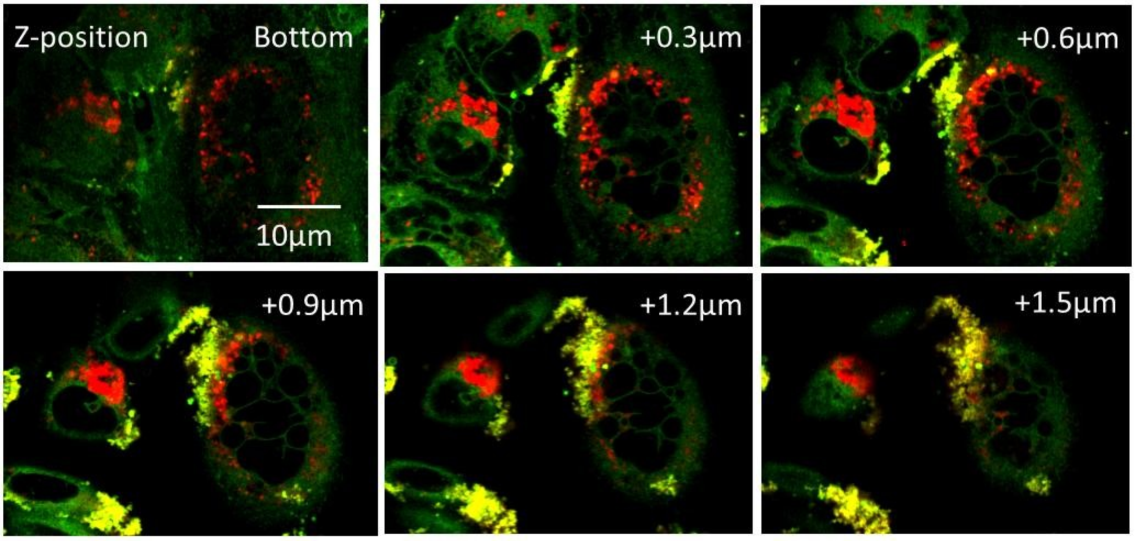

Figure 5.14: Z-stack of confocal microscope images of U_2OS cells transfected with the ($[Ru(dpp)_3]^{2+}$)-doped nanoparticles using lipofectamine. Each image is a composite of backscatter light (green) and signal from the ($[Ru(dpp)_3]^{2+}$)-doped nanoparticles (red).

From the Z-stack of confocal images above, it is clearly visible that the nanoparticles are located inside the cell after 24 hours nanoparticle uptake as well as after lipofectamine-based transfection. Prior to performing the final nanoparticle calibration experiment with the nanoparticles engulfed by U_2OS, the system (described in section 5.2.3.4) was optimized for detection of the ($[Ru(dpp)_3]^{2+}$). Based on the extensive studies performed by the group, it was established that the optimal modulation frequency for ($[Ru(dpp)_3]^{2+}$) is 20kHz. The minimum modulation frequency available on the frequency-domain FLIM instrumentation in Amsterdam was 100kHz, which has to be taken into the consideration, when evaluating the oxygen nanosensor performance. The data obtained for free ($[Ru(dpp)_3]^{2+}$) molecules dissolved in EtOH within the physiological range of dissolved oxygen concentration (see Figure 5.15) revealed the change in the lifetime of around 1.6 µs.

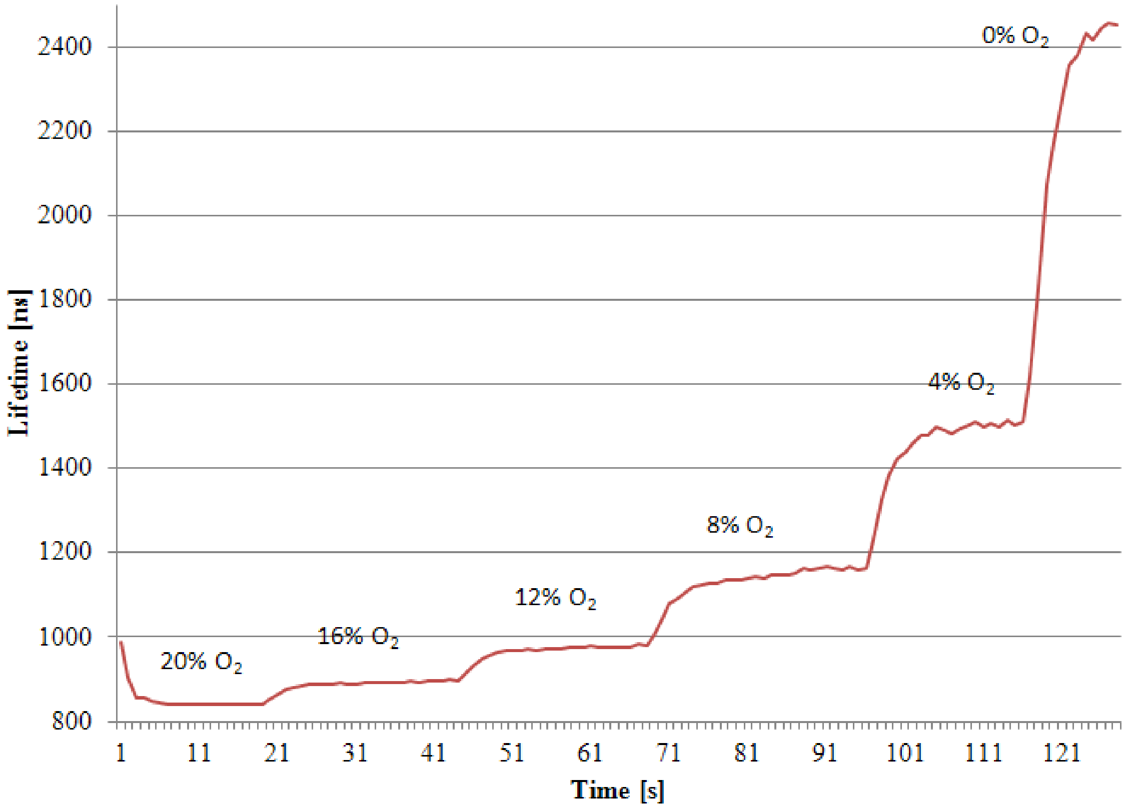

Figure 5.15: Lifetime calibration on frequency-domain FLIM for free ($[Ru(dpp)_3]^{2+}$) molecules dissolved in ethanol.

On the phase fluorometry system (described in section 2.5.3.1), in the same dissolved oxygen concentration region, the change in the lifetime for free ($[Ru(dpp)_3]^{2+}$) molecules dissolved in EtOH was around 3.5 times larger compared to the frequency-domain FLIM data. This is very likely due to the larger modulation frequency which reduces the optical signal compared to that which would be obtained at the more suitable frequency of ~ 20kHz. The calibration procedure was then repeated for the nanoparticles dispersed in water (Figure 5.16).

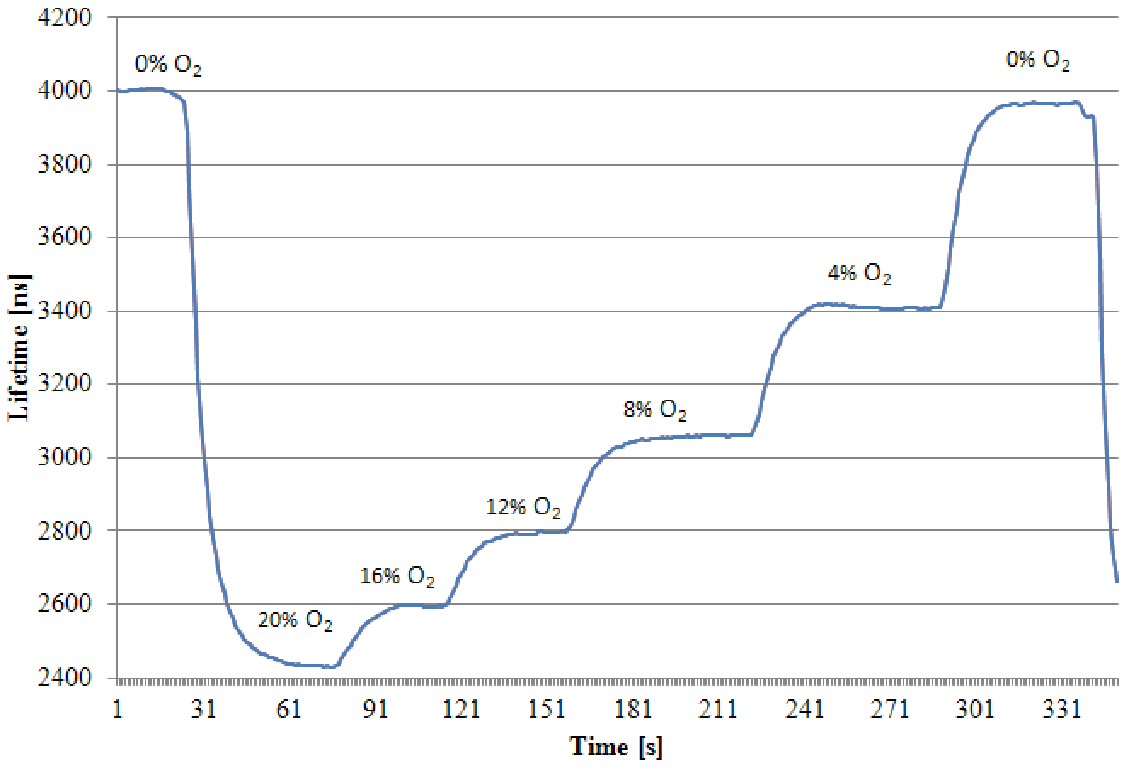

Figure 5.16: Lifetime calibration done on the frequency-domain FLIM for the nanoparticles doped with ($[Ru(dpp)_3]^{2+}$) dispersed in water.

The final experiment with the nanoparticles transfected into cells was performed and the data collected from this experiment are presented in Figures 5.17 and 5.18.

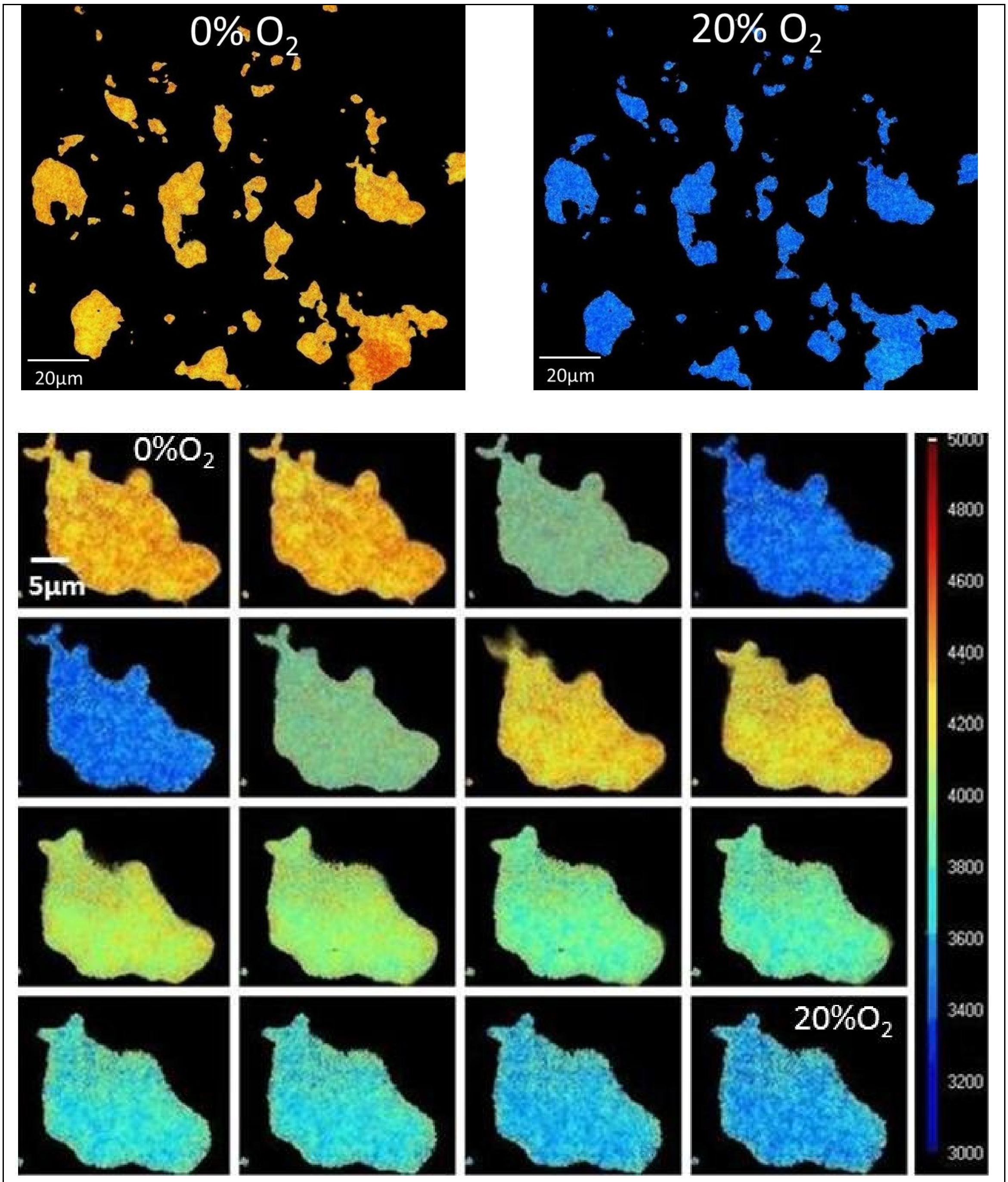

Figure 5.17: Frequency-domain FLIM images of the ($[Ru(dpp)_3]^{2+}$) – doped nanoparticles uptaken by U_2OS cells acquired under different oxygen concentration conditions (calibration gas mixtures containing from 0% up to 20% of oxygen). To visualize better the changes in the lifetime, the sequence of images containing only one cell is presented.

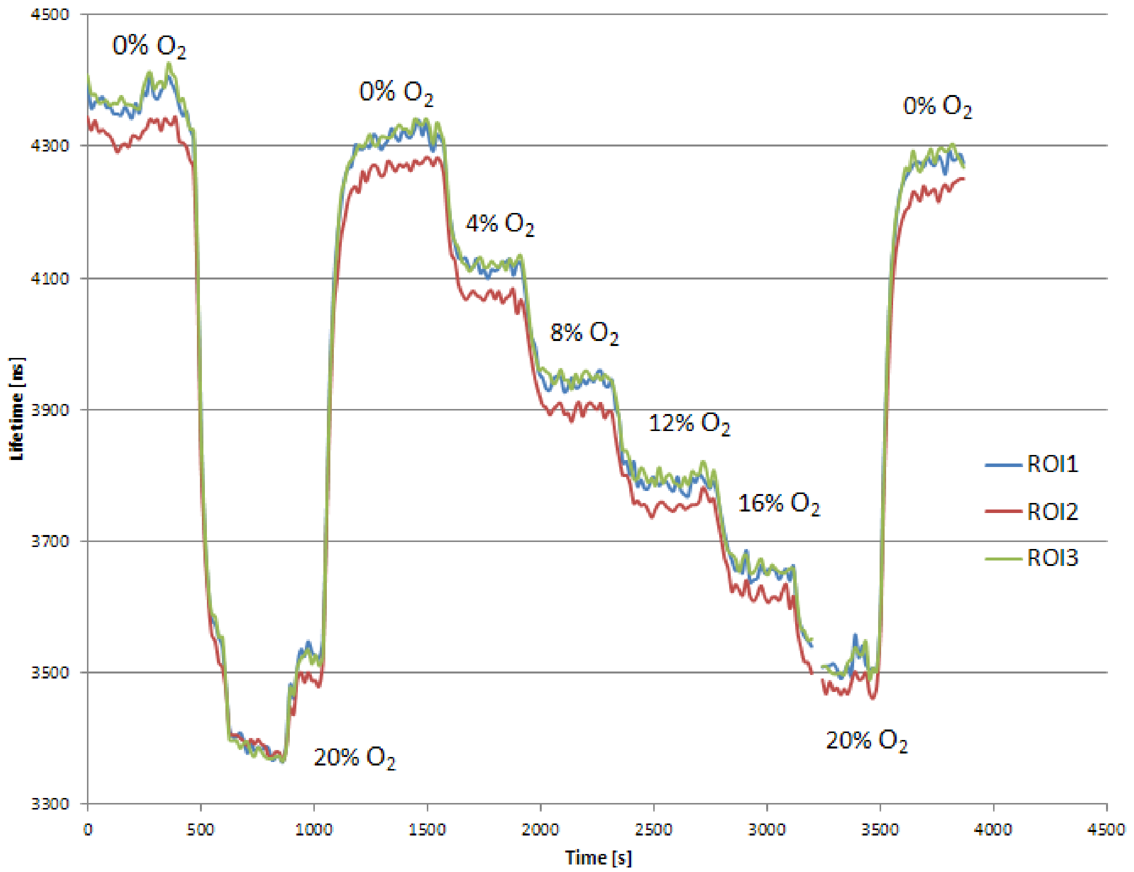

Figure 5.18: Lifetime calibration done on frequency-domain FLIM for the nanoparticles doped with ($[Ru(dpp)_3]^{2+}$) uptaken by U_2OS cells. Three different cells correspond to three different region of interest (ROI1, ROI2, ROI3).

The sensitivity of the composite nanoparticles from calibration in water was then compared to those located inside U_2OS cells (Figure 5.19).

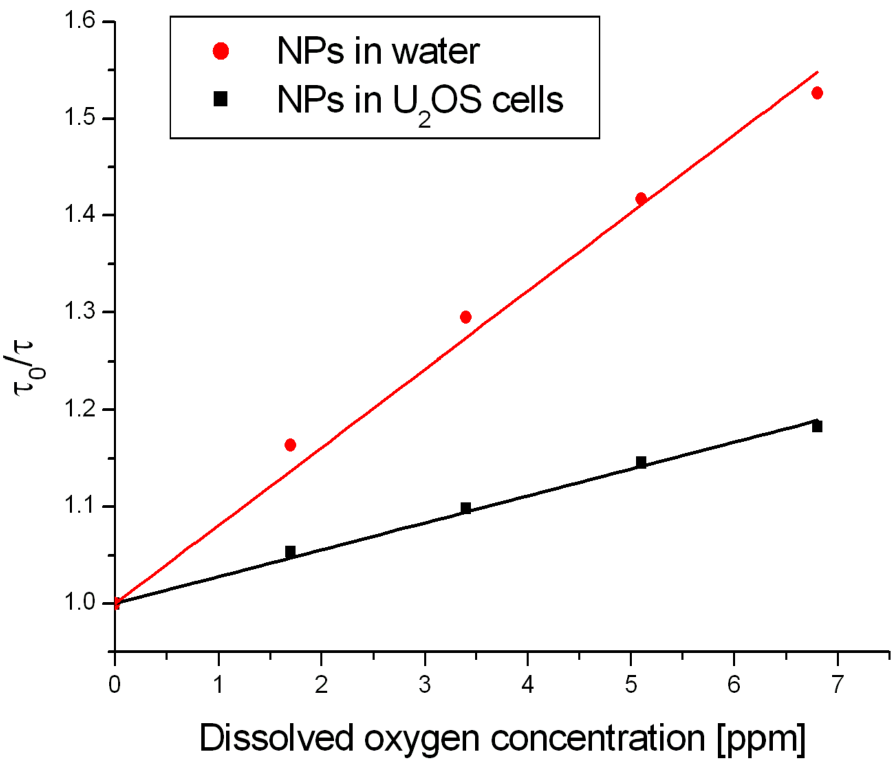

Figure 5.19: Comparison of oxygen sensitivities between the composite nanoparticles doped with ($[Ru(dpp)_3]^{2+}$) dispersed in water and uptaken by U_2OS cells.

The fitting to the linear Stern-Volmer model was performed for the data obtained from the experiments within the physiological concentration range and a good correlation to this model was observed for both data sets (see Table 5.2). The dissolved oxygen concentrations, expressed in ppm, were calculated based on the solubility constant of oxygen in water at 21°C (0.004252g of O_2 in 100g of H_2O) [10].

Table 5.2: Stern-Volmer fitting parameters obtained from frequency-domain FLIM for the composite nanoparticles dispersed in water and uptaken by U_2OS cells.

NPs in	**Stern-Volmer model - physiological concentration range**	
	$K_{SV}[O_2]^{-1}$	r^2
H_2O	0.0806 ± 0.0022	0.991
U_2OS	0.0278 ± 0.0006	0.995

As mentioned in the introduction, the complex intracellular environment can influence the nanosensor performance as observed in this case from the decrease in a value of the parameter K_{SV} for the nanoparticles located inside U_2OS cells. It has to be underlined however that due to the non-optimal modulation frequency parameters these data are only indicative of the response of the nanoparticles to intracellular oxygen concentrations and do not represent an accurate measurement. The same experiments would need to be performed on the instrument with 20 kHz modulation frequency capability to truly evaluate the performance of the nanoparticles.

5.5 Conclusions

In this chapter, nanoparticle uptake was successfully performed on four different cell lines using a range of available techniques. All approaches were successful in delivering the nanomaterial inside the cells. It was difficult to distinguish the precise intracellular localization of the nanoparticles using fluorescence confocal microscopy due to spectral cross-talk between commonly used intracellular fluorescent probes and the diffraction limited resolution of standard optical microscopy. Some other complementary techniques would need to be applied to these studies (i.e. TEM, STED) in order to gain some better insight in this matter. For the intracellular sensing experiments two different measurement techniques were employed, time and frequency-domain lifetime microscopy. Due to the long lifetime of ($[Ru(dpp)_3]^{2+}$) and limited hardware resources, the TCSPC technique could be only applied for qualitative studies. Quantitative results were obtained on the frequency-domain FLIM. A decrease in the lifetime from ~4.4μs to ~3.4μs was observed when the cells were exposed from 0% to 20% of oxygen. This change in lifetime is smaller in comparison to what was detected on the phase fluorometry setup for the nanoparticles dispersed in water. One of the factors responsible for the detected decrease in the oxygen sensitivity is the non-optimal modulation frequency. Other reasons could be related to the interaction between the nanoparticles and biological matter such as coating of the active sensing surface of the nanoparticle with proteins. Further investigation is required to fully interpret the results obtained.

References

[1] Lee, Y. K.; Kopelman, R. Optical nanoparticle sensors for quantitative intracellular imaging. *Wiley Interdisciplinary Reviews-Nanomedicine and Nanobiotechnology,* **2009**, *1*, 98-110.

[2] Fercher, A.; Borisov, S. M.; Zhdanov, A. V.; Klimant, I.; Papkovsky, D. B. Intracellular O_2-Sensing Probe Based on Cell-Penetrating Phosphorescent Nanoparticles. *Acs Nano,* **2011**, *5*, 5499-5508.

[3] Wu, S.; Song, Y.; Li, Z.; Wu, Z.; Han, J.; Han, S. Covalent labeling of mitochondria with a photostable fluorescent thiol-reactive rhodamine-based probe. *Analytical Methods,* **2012**, *4*, 1699-1703.

[4] Heller, D. A Review and Applications of Flow Cytometry. Department of Chemistry, University of Illinois at Urbana-Champaign, December 17, 2004.

[5] http://research.nki.nl/jalinklab/Homepage%20Phys&ImgGrp%200.htm "Frequency-domain FLIM".

[6] Samuelson, D. A.; Gelatt, K. N.; Gum, G. G. Kinetics of Phagocytosis in the Normal Canine Iridocorneal Angle. *Am. J. Vet. Res.,* **1984**, *45*, 2359-66.

[7] Beduneau, A.; Ma, Z.; Grotepas, C. B.; Kabanov, A.; Rabinow, B. E.; Gong, N.; Mosley, R. L.; Dou, H.; Boska, M. D.; Gendelman, H. E. Facilitated Monocyte-Macrophage Uptake and Tissue Distribution of Superparmagnetic Iron-Oxide Nanoparticles. *Plos One,* **2009**, *4*, 4343.

[8] Meng, H.; Yang, S.; Li, Z.; Xia, T.; Chen, J.; Ji, Z.; Zhang, H.; Wang, X.; Lin, S.; Huang, C.; Zhou, Z. H.; Zink, J. I.; Nel, A. E. Aspect Ratio Determines the Quantity of Mesoporous Silica Nanoparticle Uptake by a Small GTPase-Dependent Macropinocytosis Mechanism. *Acs Nano,* **2011**, *5*, 4434-47.

[9] Hunt, T. K.; Knighton, D. R.; Thackral, K. K.; Goodson, W. H.; Andrews, W. S. Studies on inflammation and wound healing: angiogenesis and collagen synthesis stimulated in vivo by resident activated wound macrophages. *Surgery*, **1983**, *96*, 48-54.

[10] Xu, H.; Aylott, J. W.; Kopelman, R.; Miller, T. J.; Philbert, M. A. A real-time ratiometric method for the determination of molecular oxygen inside living cells using sol-gel-based spherical optical nanosensors with applications to rat C6 glioma. *Anal. Chem.,* **2001***, 73*, 4124-4133.

Chapter 6

Summary and Perspectives

The main objectives of this interdisciplinary project, as stated in chapter 1 of the thesis, were the development, characterization and optimisation of novel oxygen and pH – sensitive nanoparticles for intracellular sensing applications.

The first goal – synthesis of novel nanoparticles with enhanced oxygen sensitivity, was achieved by incorporation of an organically modified silica precursor - MTEOS into the nanoparticle structure. A gradual improvement in the nanoparticle oxygen response was achieved. An increase in oxygen response of around 1.5 times within the physiological dissolved oxygen concentration range (0-10ppm) was detected for the composite nanoparticles synthesized via a newly developed modified Stöber approach compared to pure silica particles obtained from the conventional Stöber process. These optimal composite nanoparticles, with the highest oxygen-sensitivity, exhibit very good sensor performance, namely excellent batch to batch reproducibility, reversibility and temporal stability. Additionally, in the region of dissolved oxygen concentration relevant to this cellular application, an excellent (r^2=0.999) and good (r^2 = 0.994) correlation to the Demas and Stern-Volmer models is observed, respectively. This quasi-linear response of the nanosensor enables a two-point calibration strategy. Due to the cost, availability and overall complexity of the FLIM instrumentation, ratiometric intensity-based nanoparticles were developed as an alternative to the lifetime-based particles. Both types of nanoparticles were encapsulated in cells and the lifetime-based intracellular oxygen response was measured.

The second goal – synthesis of pH-sensitive nanoparticles to monitor initially pH within cytosol was successfully accomplished by incorporation of pH-sensitive FITC and pH-insensitive Texas Red to the TEOS - nanoparticle matrix. Both dyes were covalently linked to the nanoparticle structure to avoid the problem with leaching of the dye (observed for the HPTS-doped approach) from the nanoparticle matrix into the cell environment. These nanoparticles, with pKa equal to 7.17, are well suited for intracellular cytosolic investigation.

The third goal – the intracellular delivery of nanoparticles was performed using many different approaches such as passive uptake, chemical transfection, electroporation as well as using a recombinant cell line. All of these strategies resulted in efficient delivery of the nanoparticles inside various cell lines. The phagocytic uptake of the nanoparticles by the macrophages was also investigated. Confocal microscopy was used to investigate the intracellular location of the nanoparticles. Protocols for staining of the intracellular compartments were optimised and applied in these studies. The cellular membrane staining confirmed the positive uptake information. For the mitochondrial stain, the signal from both fluorophores incorporated in the nanoparticles and the mitochondria-targeting dye were collected from the same pixels, which can indicate the nanoparticle intracellular localisation in the proximity of or inside the mitochondria. However more detailed fluorescence co-localization and alternative TEM imaging should be performed to fully understand the nanoparticle localisation. Under all conditions tested, cellular uptake does not significantly alter particle photophysics and the particles retain their high molecular brightness and are easily distinguishable from endogenous fluorescent proteins both in terms of intensity and fluorescence lifetime. Additionally these particles can be tolerated within the cell for extended periods of time (24 hours) without obvious cytotoxic effects.

The fourth goal – the intracellular sensing experiments were successfully performed for oxygen only, using two different approaches, time- and frequency-domain FLIM. Due to the long lifetime of ($[Ru(dpp)_3]^{2+}$), the data obtained from the time-domain FLIM is qualitative in nature. Nevertheless, very good contrast between the long-lifetime nanoparticles doped with ($[Ru(dpp)_3]^{2+}$) and short-lifetime endogenous proteins was observed on the images acquired in this time-domain mode, which is a big advantage over conventional fluorescence imaging. The data collected on frequency-domain FLIM revealed the good potential of this technique for the intracellular sensing application.

From the preliminary results obtained from the proof-of concept study, around 1.6 μs change in the lifetime within the physiological dissolved oxygen concentration region was detected. The modulation frequency used for the measurements was not optimal for ($[Ru(dpp)_3]^{2+}$) (100 kHz used instead of 20 kHz), therefore it was not possible to obtain the absolute quantitative information about the nanosensor sensitivity. Both imaging techniques had a positive contribution to the project and might be investigated in the future for specific intracellular diagnostics applications. Using the nanoparticles as a diagnostic tool can enable the early detection of disease and can contribute to more efficient therapeutics.

Future work in the context of oxygen sensing could consist of the development of other nanoparticle formulations based on optimising the new modified Stöber synthesis for other organosilicon precursors or by changing the ($[Ru(dpp)_3]^{2+}$) to some other fluorophore with the longer lifetime; for example, porphyrin complexes. Expanding the area of the application for the pH-sensitive nanoparticles could be accomplished by the incorporation of a third fluorophore with a lower pKa into the nanoparticle structure in order to sense the pH in the intracellular compartments with lower pH such as endosomes and lysosomes. The delivery of the nanoparticles could be as well improved by labelling the nanoparticles with a specific antibody to the intracellular organelle or by using other techniques, including encapsulation of the nanoparticle into the liposomes. In the course of this work, while pH-sensitive nanoparticles were synthesised and characterised, it was not possible to proceed with cellular sensing. This work is ongoing.

FLIM is a very promising technique, which could be applied in order to monitor the analyte changes occurring inside the cell. Nevertheless, a dependence of the modulation frequency on the luminophore lifetime has to be well considered in obtaining precise measurements. Due to the short lifetimes of fluorophores used for the cellular imaging, most FLIM setups are equipped with the frequency modulation modules, which operate at high frequencies. The long lifetime oxygen-sensitive dyes require much lower (10Hz-50kHz) modulation frequencies. To obtain the precise quantitative data from these intracellular sensing measurements, frequency-domain FLIM with a shorter modulation frequency (~20kHz) should be used for the experiments.

A huge area of research is devoted to monitoring the parameters from a single cell. The combination of microfluidics with intracellular sensing could provide very interesting results, where monitoring of the parameters of the single cell could be accomplished. Collectively, these results demonstrate the successful application of ($[Ru(dpp)_3]^{2+}$)-doped nanoparticles for intracellular oxygen sensing. Overall, this thesis demonstrates the huge potential for the development of oxygen, pH and other analyte-sensitive nanoparticles, which would lead to a multifunctional platform for early diagnostics and therapeutics applications.

List of conference presentations

Oral Presentations:

"Silica nanoparticle-based intracellular diagnostics", Young Scientist Lecture Competition at 6th International Conference on Surfaces, Coatings & Nanostructured Materials (NANOSMAT), Cracow, Poland, 17-20.10.2011.

Poster Presentations:

B. Korzeniowska, A. Schulz, D. Wencel, C. McDonagh, "Luminescent nanoparticle-based intracellular sensing", IEEE conference, Limerick, 28-31.10.2011.

B. Korzeniowska, J. Decourcey, D. Wencel, C. Loscher, R. Woolley, C. McDonagh, "Sol-gel-derived luminescent nanoparticle-based oxygen and pH sensors for intracellular diagnostics", Sol-Gel Conference, Hangzhou, China, 28.08 - 02.09.2011.

B. Korzeniowska, J. Decourcey, D. Wencel, R. Woolley, C. Loscher, B. D. MacCraith, C. McDonagh, "Nanoparticle-based intracellular diagnostics", VI Meeting of the Irish Cytometry Society, Guinness Storehouse, Dublin, 17-18.11.2010.

B. Korzeniowska, A. Panzera, S. Roy, D. Wencel, A. Schulz, J. Decourcey, R. Wooley, C. Loscher, S. Ramstrom, D. Kenny, B. D. MacCraith, C. McDonagh, "Fluorescent nanoparticles (NPs) for intra- and inter-cellular diagnostics", BioPIC conference, Meath, Ireland, 18-20.10.2010.

A. Panzera, B. Korzeniowska, S. Roy, D. Wencel, A. Schulz, J. Decourcey, R. Wooley, C. Loscher, S. Ramstrom, D. Kenny, B. D. MacCraith, C. McDonagh, "Intra- and inter-cellular diagnostics using fluorescent nanoparticles", Europtrode X, Prague, 28.03-31.03.2010.

B. Korzeniowska, J. Decourcey, D. Wencel, R. Woolley, C. Loscher, B. D. MacCraith, C. McDonagh, "Nanoparticle-based intracellular diagnostics", Photonics Ireland, Kinsale, 14-16.09.2009.

Awards:

2nd prize in the poster competition at the Photonics Conference in Kinsale

1st prize in the poster competition at the Irish Cytometry Society Meeting in Dublin

3rd prize in Young Scientist Lecture Competition with the oral presentation on "Silica nanoparticle-based intracellular diagnostics".

Proof-of-concept study

"Intracellular oxygen sensing using frequency-domain FLIM", European research infrastructure Euro – Bioimaging Proof-of-concept project, Netherlands Cancer Institute in Amsterdam